

UNIVERSITY OF CALIFORNIA, SAN DIEGO

Designing and Diagnosing Novel Electrode Materials for Na-ion Batteries:  
Potential Alternatives to Current Li-ion Batteries

A dissertation submitted in partial satisfaction of the  
requirements for the degree Doctor of Philosophy

in

Materials Science and Engineering

by

Jing Xu

Committee in charge:

Professor Ying Shirley Meng, Chair  
Professor Renkun Chen  
Professor Eric E. Fullerton  
Professor Sungho Jin  
Professor Yu Qiao

2014

Copyright

Jing Xu, 2014

All rights reserved.

The Dissertation of Jing Xu is approved, and it is acceptable in quality and form for publication on microfilm and electronically:

---

---

---

---

---

Chair

University of California, San Diego

2014

## **DEDICATION**

*To Xiaosong Xu and Jingyan Zhang*

## TABLE OF CONTENTS

Signature Page.....	iii
Dedication.....	iv
Table of Contents.....	v
List of Figures.....	vii
List of Tables.....	xi
Acknowledgements.....	xii
Vita.....	xv
Abstract of the Dissertation.....	xviii
Chapter 1. Motivation and Outline.....	1
Chapter 2. Introduction of the alkali-ion batteries.....	4
2.1. The configuration of the alkali battery.....	4
2.2. Charging and discharging process in alkali-ion batteries.....	7
2.3. Practical criterions for the electrode materials designs in alkali-ion batteries.....	8
2.4. Recent progress in electrode materials for Na-ion batteries.....	9
2.4.1. <i>Layered metal oxides as cathode materials</i> .....	9
2.4.2. <i>Polyanion compounds as cathode materials</i> .....	12
2.4.3. <i>Anode materials</i> .....	15
Chapter 3. Advanced characterization tools.....	22
3.1. Synchrotron X-ray scattering techniques.....	22
3.1.1 <i>Synchrotron radiation</i> .....	22
3.1.2 <i>In situ synchrotron X-ray diffraction (SXRD)</i> .....	23
3.1.3 X-ray absorption spectroscopy (XAS).....	24
3.2. First principles calculation.....	26
3.2.1 <i>Density functional theory</i> .....	26
3.2.2 <i>Application in battery study</i> .....	28
Chapter 4. Advanced cathode for Na-ion batteries with high rate and excellent structural stability.....	34
4.1. Introduction.....	34
4.2. Experimental.....	37
4.3. Results and discussion.....	39

4.3.1. <i>Electrochemical properties of P2 – Na<sub>2/3</sub>[Ni<sub>1/3</sub>Mn<sub>2/3</sub>]O<sub>2</sub></i> .....	39
4.3.2. <i>Structural properties of P2 – Na<sub>2/3</sub>[Ni<sub>1/3</sub>Mn<sub>2/3</sub>]O<sub>2</sub> upon the charge and discharge</i> .....	40
4.3.3. <i>Na-ion ordering effects</i> .....	43
4.3.4. <i>Diffusion properties of Na-ion in P2 – Na<sub>2/3</sub>[Ni<sub>1/3</sub>Mn<sub>2/3</sub>]O<sub>2</sub></i> .....	44
4.3.5. <i>Electronic structural properties</i> .....	45
4.3.6. <i>Improved electrochemical properties of P2 – Na<sub>2/3</sub>[Ni<sub>1/3</sub>Mn<sub>2/3</sub>]O<sub>2</sub></i> .....	47
4.4. Discussion.....	48
Chapter 5. Identifying the Critical Role of Li Substitution in P2 – Na <sub>x</sub> [Li <sub>y</sub> Ni <sub>z</sub> Mn <sub>1-y-z</sub> ]O <sub>2</sub> (0 < x, y, z < 1) Intercalation Cathode Materials for High Energy Na-ion Batteries.....	
5.1. Introduction .....	59
5.2. Experimental.....	61
5.3. Results and discussion.....	64
5.3.1. <i>Electrochemical performances of Na<sub>0.8</sub>[Li<sub>0.12</sub>Ni<sub>0.22</sub>Mn<sub>0.66</sub>]O<sub>2</sub></i> .....	64
5.3.2. <i>Structural characterization by neutron diffraction and NMR</i> .....	65
5.3.3. <i>Structural evolutions during the charge by in situ synchrotron XRD</i> ...	69
5.3.4. <i>Li site change studied by ex-situ NMR</i> .....	71
5.3.5. <i>Electronic and local structural changes by XAS</i> .....	72
5.3.6. <i>The role of Li substitution in Na<sub>0.8</sub>[Li<sub>0.12</sub>Ni<sub>0.22</sub>Mn<sub>0.66</sub>]O<sub>2</sub></i> .....	74
5.3.7. <i>Materials design principles and Na<sub>0.83</sub>[Li<sub>0.07</sub>Ni<sub>0.31</sub>Mn<sub>0.62</sub>]O<sub>2</sub></i> .....	76
5.4. Conclusion.....	77
Chapter 6. Breaking through the limitation of energy / power density for Na-ion battery cathodes .....	
6.1. Introduction .....	93
6.2. Experimental.....	95
6.3. Results and discussion.....	97
6.4. Conclusion.....	102
Chapter 7. Understanding Na <sub>2</sub> Ti <sub>3</sub> O <sub>7</sub> as an ultra-low voltage anode material for Na-ion batteries.....	
7.1. Introduction .....	111
7.2. Experimental.....	113
7.3. Results and discussion.....	115
7.4. Conclusion.....	120
Chapter 8. Summary and future work.....	
References.....	136

## LIST OF FIGURES

Figure 2.1	Schematic of a rechargeable alkali-ion battery. $A^+$ is the alkali ion....17
Figure 2.2	Cycling voltammograms of (a) Al and (b) Cu in LIB respectively .....18
Figure 2.3	Schematics of crystal structures of (a) O3, (b) P2, (c) NASICON, (d) $Na_{1.5}VOPO_4F_{0.5}$ , (e) $Na_2FePO_4F$ and (f) $Na_2FeP_2O_7$ .....19
Figure 2.4	Summary of specific capacity, operating voltage range and energy density of the intercalation cathode materials for Na-ion batteries.....20
Figure 3.1	X-ray absorption spectroscopy spectra including XANES and EXAFS regions. Inset schemes illustrate the origins of the oscillation in the spectra.....32
Figure 3.2	Schematic of the application of the DFT calculations in battery research.....33
Figure 4.1	(a) Electrochemical profiles for $Na/Na_{2/3}[Ni_{1/3}Mn_{2/3}]O_2$ cells between 2.3 to 4.5 V at C/100 current rate including the calculated voltage profiles, (b) Calculated formation energies at different Na concentration including the convex hull and (c) Structural schematics of P2 and O2 .....50
Figure 4.2	(a) Synchrotron X-ray diffraction patterns of $Na_x[Ni_{1/3}Mn_{2/3}]O_2$ at different x concentration during the 1st cycle, (b) Changes in a and c lattice parameters, and (c) Changes in $Na_f$ and $Na_e$ site occupancies upon the 1st cycle .....51
Figure 4.3	In-plane Na-ions orderings of $Na_x[Ni_{1/3}Mn_{2/3}]O_2$ in the triangular lattice (a) $x = 2/3$ , (b) $x = 1/2$ , and (c) $x = 1/3$ (Blue balls: Na-ions on $Na_e$ sites, pink balls: Na-ions on $Na_f$ sites).....52
Figure 4.4	(a) The diffusion paths of P2 (left) and O2 (right), (b) Calculated activation energy using NEB method, and (c) Chemical diffusion coefficient of Na-ions ( $D_{Na}$ ) in $Na_x[Ni_{1/3}Mn_{2/3}]O_2$ calculated from GITT as a function of the Na concentration.....53
Figure 4.5	The electronic structures of Ni 3d and Mn 3d orbitals in $Na_x[Ni_{1/3}Mn_{2/3}]O_2$ at (a) $x = 2/3$ , (b) $x = 1/3$ , and (c) $x = 0$ .....54
Figure 4.6	(a) Schematic illustration of the oxygen layer, (b) Calculated spin density cutting from oxygen layer at $x = 2/3$ , and (c) $x = 0$ .....54
Figure 4.7	The electrochemical properties of $Na/Na_{2/3}[Ni_{1/3}Mn_{2/3}]O_2$ cells, (a) Cycling performances at different voltage ranges (2.3 ~ 4.1 V and 2.3 ~

	4.5 V) and different C-rate (C/100, C/20 and C/5), and (b) Rate capability at C/20, C/10, C/2, 1C and 2C between 2.3 ~ 4.1 V.....55
Figure 5.1	(a) The electrochemical profiles for $\text{Na}_{0.80}[\text{Li}_{0.12}\text{Ni}_{0.22}\text{Mn}_{0.66}]\text{O}_2$ at the 1 <sup>st</sup> , 2 <sup>nd</sup> , 3 <sup>rd</sup> , 30 <sup>th</sup> and 50 <sup>th</sup> cycle, and (b) the rate capability at different current densities from C/10 to 5C .....80
Figure 5.2	The (a) XRD and (b) SEM image of as-synthesized P2 – $\text{Na}_{0.80}[\text{Li}_{0.12}\text{Ni}_{0.22}\text{Mn}_{0.66}]\text{O}_2$ powder. ....81
Figure 5.3	(a) Neutron diffraction patterns including extended view of superlattice region (inset), and (b) NMR spectra of as-synthesized P2- $\text{Na}_{0.8}[\text{Li}_{0.12}\text{Ni}_{0.22}\text{Mn}_{0.66}]\text{O}_2$ .....82
Figure 5.4	(a) <i>In situ</i> SXRD for $\text{Na}_{0.80}[\text{Li}_{0.12}\text{Ni}_{0.22}\text{Mn}_{0.66}]\text{O}_2$ during the 1 <sup>st</sup> charge, (b) changes in the <i>a</i> and <i>c</i> lattice parameters upon the 1 <sup>st</sup> charge by the refinement., and (c) simulated XRD patterns with different percentage of stacking faults by CrystalDiffact software .....83
Figure 5.5	(a) Ex situ SXRD patterns of pristine and fully cycled $\text{Na}_{0.80}[\text{Li}_{0.12}\text{Ni}_{0.22}\text{Mn}_{0.66}]\text{O}_2$ . (b) Comparison of ex situ SXRD pattern of $\text{Na}_{0.80}[\text{Li}_{0.12}\text{Ni}_{0.22}\text{Mn}_{0.66}]\text{O}_2$ electrode after one full charge under CCCV to XRD pattern of the O2 phase (including a hydrated phase) .....84
Figure 5.6	Isotropic slices of <sup>7</sup> Li pj-MATPASS NMR spectra acquired at 200 MHz on as-synthesized P2- $\text{Na}_{0.8}[\text{Li}_{0.12}\text{Ni}_{0.22}\text{Mn}_{0.66}]\text{O}_2$ and at three different stages along the first electrochemical cycle. pj-MATPASS experiments were performed using a train of five non-selective $\pi/2$ pulses.....85
Figure 5.7	1D <sup>7</sup> Li Hahn echo spectra recorded of as-synthesized $\text{Na}_{0.80}[\text{Li}_{0.12}\text{Ni}_{0.22}\text{Mn}_{0.66}]\text{O}_2$ and $\text{Na}_{0.80}[\text{Li}_{0.12}\text{Ni}_{0.22}\text{Mn}_{0.66}]\text{O}_2$ charged to 4.1 V, 4.4 V, discharged to 2.0 V, and after 5 electrochemical cycles.....86
Figure 5.8	XAS analysis of $\text{Na}_{0.8}[\text{Li}_{0.12}\text{Ni}_{0.22}\text{Mn}_{0.66}]\text{O}_2$ charged to 4.1 V, 4.4 V and discharged to 2.0 V at Ni K-edge (a) XANES region including NiO standard and (b) EXAFS spectra .....87
Figure 5.9	XAS analysis of $\text{Na}_{0.8}[\text{Li}_{0.12}\text{Ni}_{0.22}\text{Mn}_{0.66}]\text{O}_2$ charged to 4.4 V and discharged to 2.0 V at Mn K-edge (a) XANES region including NiO standard and (b) EXAFS spectra .....88
Figure 5.10	The electrochemical profiles for $\text{Na}_{0.83}[\text{Li}_{0.07}\text{Ni}_{0.31}\text{Mn}_{0.62}]\text{O}_2$ in the voltage range of 2.0 ~ 4.4 V at the 1 <sup>st</sup> , 3 <sup>rd</sup> , and 5 <sup>th</sup> cycle .....89
Figure 6.1	Electrochemical profile for $\text{Li}_{1.133}\text{Ni}_{0.3}\text{Mn}_{0.567}\text{O}_2$ during initial delithiation and initial sodiation.....104

Figure 6.2	(a) Electrochemical profiles of initial delithiation and initial sodiation. (b) Electrochemical profile of $\text{Na}_{0.719}\text{Li}_{0.073}\text{Ni}_{0.3}\text{Mn}_{0.567}\text{O}_2$ during the 1 <sup>st</sup> , 2 <sup>nd</sup> , 10 <sup>th</sup> , 20 <sup>th</sup> , 30 <sup>th</sup> cycles in Na-ion batteries. (c) Comparison of reversible capacities for the intercalation-based Na cathodes.....	105
Figure 6.3	SEM images for as-synthesized $\text{Na}_{0.78}\text{Li}_{0.18}\text{Ni}_{0.25}\text{Mn}_{0.583}\text{O}_2$ .....	106
Figure 6.4	Rate performance of $\text{Na}_{0.78}\text{Li}_{0.18}\text{Ni}_{0.25}\text{Mn}_{0.583}\text{O}_2$ .....	106
Figure 6.5	(a) Ex situ XRD for $\text{Li}_{1.167}\text{Ni}_{0.25}\text{Mn}_{0.583}\text{O}_2$ and $\text{Na}_{0.78}\text{Li}_{0.18}\text{Ni}_{0.25}\text{Mn}_{0.583}\text{O}_2$ at different states. (b) Schematic of O3 structure. (c) Schematic of the proposed mechanism.....	107
Figure 6.6	XAS analysis for $\text{Li}_{1.167}\text{Ni}_{0.25}\text{Mn}_{0.583}\text{O}_2$ and $\text{Na}_{0.78}\text{Li}_{0.18}\text{Ni}_{0.25}\text{Mn}_{0.583}\text{O}_2$ at different states. XANES spectra for (a) Ni and (b) Mn K-edge respectively. EXAFS spectra for (a) Ni and (b) Mn K-edge respectively.....	108
Figure 6.7	Schematic of Na full. (b) The electrochemical profile at 1 <sup>st</sup> cycle and (c) cycling performance for Na full cell.....	109
Figure 6.8	The electrochemical profile for $\text{Li}_{1.167}\text{Ni}_{0.166}\text{Mn}_{0.5}\text{Co}_{0.166}\text{O}_2$ during initial delithiation and initial sodiation. (b) XRD for as-synthesized $\text{NaLi}_{0.067}\text{Co}_{0.267}\text{Ni}_{0.267}\text{Mn}_{0.4}\text{O}_2$ .....	110
Figure 7.1	The (a) XRD and (b) (c) SEM images of as-synthesized $\text{Na}_2\text{Ti}_3\text{O}_7$ powder.....	121
Figure 7.2	(a) Voltage profiles of carbon-coated $\text{Na}_2\text{Ti}_3\text{O}_7$ in the 2 <sup>nd</sup> , 10 <sup>th</sup> , 25 <sup>th</sup> , 50 <sup>th</sup> , 75 <sup>th</sup> and 100 <sup>th</sup> cycles at C/10 rate. (b) Cycling performance for carbon-coated and bare $\text{Na}_2\text{Ti}_3\text{O}_7$ . (c) Voltage profiles and (d) Cycling performance for the Na full cell.....	122
Figure 7.3	Rate performance of carbon-coated $\text{Na}_2\text{Ti}_3\text{O}_7$ electrode.....	123
Figure 7.4	TEM images for (a) bare and (b) carbon-coated $\text{Na}_2\text{Ti}_3\text{O}_7$ at pristine state. TEM images for (c) bare and (d) carbon-coated $\text{Na}_2\text{Ti}_3\text{O}_7$ after 1 <sup>st</sup> discharge.....	124
Figure 7.5	Electrochemical profiles at of (a) carbon-coated and (b) bare $\text{Na}_2\text{Ti}_3\text{O}_7$ at C/25 .....	125
Figure 7.6	(a) The phase transformation (b) related structural change upon Na intercalation. (c) The calculated voltage and electrostatic energy at x=2 and x=4 for $\text{Li}_x\text{Ti}_3\text{O}_7$ and $\text{Na}_x\text{Ti}_3\text{O}_7$ respectively. The narrow bar is for $\text{Li}_x\text{Ti}_3\text{O}_7$ and wide one for $\text{Na}_x\text{Ti}_3\text{O}_7$ .....	126

Figure 7.7	(a) Change in the XRD patterns with time for fully discharged electrodes. (b) Normalized Ti K-edge XANES for $\text{Na}_2\text{Ti}_3\text{O}_7$ at pristine state (red), after discharged to 0.10 V (blue), and after discharged to 0.01 V (green) .....127
Figure 7.8	Voltage profiles for electrodes under cycling (a) with and (b) without interval rest (5 hour between charge and discharge). (c) Cycling performance for cell with (blue) and without (green) interval rest...128
Figure 7.9	5 <sup>th</sup> and 10 <sup>th</sup> Voltage profiles for electrodes with interval rest (5 hour between charge and discharge).....128
Figure 7.10	Thermogravimetric analysis for bare (black) and carbon coated (red) $\text{Na}_2\text{Ti}_3\text{O}_7$ powder.....129

## LIST OF TABLES

Table 2.1	Summary of three typical positive electrode materials for LIBs.....	21
Table 4.1	Rietveld refinement results (lattice parameters, Na sites, and R-factors).....	56
Table 5.1	Parameters and reliability factors obtained by the Rietveld refinement of neutron diffraction for as-synthesized P2-Na <sub>0.8</sub> [Li <sub>0.12</sub> Ni <sub>0.22</sub> Mn <sub>0.66</sub> ]O <sub>2</sub> ...	90
Table 5.2	Parameters and reliability factors obtained by the Rietveld refinement of X-ray diffraction for as-synthesized P2-Na <sub>0.8</sub> [Li <sub>0.12</sub> Ni <sub>0.22</sub> Mn <sub>0.66</sub> ]O <sub>2</sub> ...	91
Table 5.3	Distribution of Li-ions between TMO <sub>2</sub> and Na layer sites.....	92
Table 6.1	Refined lattice parameters for Li <sub>1.167</sub> Ni <sub>0.25</sub> Mn <sub>0.583</sub> O <sub>2</sub> and Na <sub>0.78</sub> Li <sub>0.18</sub> Ni <sub>0.25</sub> Mn <sub>0.583</sub> O <sub>w</sub> at different states.....	110

## ACKNOWLEDGEMENTS

First of all, I would foremost like to thank my advisor, Dr. Ying Shirley Meng, for her generous financial supports and great inspiration and motivation. I was sincerely honored to meet and work with her. I shall never forget her endless advice and help. I would like to express the deepest gratitude to my other committee members: Dr. Renkun Chen, Dr. Eric E. Fullerton, Dr. Sungho Jin, and Dr. Yu Qiao for their time and guidance.

Secondly, I would like to acknowledge my collaborators and co-authors in UCSD, Dr. Dae Hoe Lee, Chuze Ma and Haodong Liu, with whom I had many useful and stimulating discussions. I'm also grateful to all my group mates in Laboratory for Energy Storage and Conversion (LESC) who have helped and inspired me in many ways.

Finally, I would like to express my special thanks to my collaborators and co-authors, Dr. Clare P. Grey and Raphael J. Clement at University of Cambridge, Dr. Xiao-Qing Yang and Dr. Xiqian Yu at Brookhaven national laboratory, Dr. Shigeto Okada and Jie Zhao at Kyushu University, and Dr. Mahalingam Balasubramanian at Argonne national laboratory for their invaluable help throughout the projects.

Chapter 2, in part, is a reprint of the material "Recent advances in sodium intercalation positive electrode materials for sodium ion batteries" as it appears in the Functional materials letters, Jing Xu, Dae Hoe Lee, Ying S. Meng, 2013, 6, 1330001. The dissertation author was the co-primary investigator and author of this paper. The author wrote the polyanion cathodes for the Na-ion battery part.

Chapter 4, in full, is a reprint of the material "Advanced cathode for Na-ion batteries with high rate and excellent structural stability" as it appears in the Physical Chemistry Chemical Physics, Dae Hoe Lee, Jing Xu, Ying S. Meng, 2013, 15, 3304. The

dissertation author was the co-primary investigator and author of this paper. All the computational parts were performed by the author.

Chapter 5, in full, is a reprint of the material “Identifying the critical role of Li substitution in  $P2\text{-Na}_x[\text{Li}_y\text{Ni}_z\text{Mn}_{1-y-z}]\text{O}_2$  ( $0 < x, y, z < 1$ ) intercalation cathode materials for high energy Na-ion batteries” as it appears in Chemistry of Materials, Jing Xu, Dae Hoe Lee, Raphael J. Clement, Xiqian Yu, Michal Leskes, Andrew J. Pell, Guido Pintacuda, Xiao-qing Yang, Clare P. Grey, Ying Shirley Meng, 2014, 26, 1260-1269.”. The dissertation author was the co-primary investigator and author of this paper. The author conducted materials design, synthesis, electrochemical characterization, SXRDR refinement and corresponding writing.

Chapter 6, in full, is currently being prepared for submission for publication of the material “Breaking through the limitation of energy / power density for Na-ion battery cathodes”. The dissertation author was the co-primary investigator and author of this paper. The author collected and analyzed in-situ synchrotron X-ray diffraction (SXRDR) and X-ray absorption spectroscopy (XAS), and wrote the whole paper.

Chapter 7, in full, is currently being submitted for publication of the material “Understanding  $\text{Na}_2\text{Ti}_3\text{O}_7$  as an ultra-low voltage anode material for Na-ion battery”. The dissertation author was the co-primary investigator and author of this paper. The author conducted XAS experiment, first principles calculation and corresponding writing.

I would like to acknowledge the financial support from the National Science Foundation under Award Number 1057170 and from the Northeastern Center for Chemical Energy Storage, an Energy Frontier Research Center funded by the U.S. Department of Energy, Office of Basic Energy Sciences, with Award Number DE-SC 0001294.

For the last but not least, my deepest gratitude goes to my parents Xiaosong Xu and Jingyan Zhang for their love, patience and never-ending support. I specially thank to my fiance, He Liu, for his endless support and encouragement during my Ph.D.

## VITA

- 2009 Bachelor of Science, University of Science and Technology of China
- 2011 Master of Science, University of Southern California
- 2014 Doctor of Philosophy, University of California, San Diego

## PUBLICATIONS

1. Ding, N.; Feng, X. Y.; Liu, S. H.; **Xu, J.**; Fang, X.; Lieberwirth, I.; Chen, C. H., High capacity and excellent cyclability of vanadium (IV) oxide in lithium battery applications. *Electrochemistry Communications* **2009**, 11, 538-541.
2. Ding, N.; Fang, X.; **Xu, J.**; Yao, Y. X.; Zhu, J.; Chen, C. H., Performance of lithium-ion cells with a gamma-ray radiated electrolyte. *Journal of Applied Electrochemistry* **2009**, 39, 995-1001.
3. Ding, N.; **Xu, J.**; Yao, Y. X.; Wegner, G.; Fang, X.; Chen, C. H.; Lieberwirth, I., Determination of the diffusion coefficient of lithium ions in nano-Si. *Solid State Ionics* **2009**, 180, 222-225.
4. Ding, N.; **Xu, J.**; Yao, Y. X.; Wegner, G.; Lieberwirth, I.; Chen, C. H., Improvement of cyclability of Si as anode for Li-ion batteries. *Journal of Power Sources* **2009**, 192, 644-651.
5. Chen, P. C.; **Xu, J.**; Chen, H. T.; Zhou, C. W., Hybrid silicon-carbon nanostructured composites as superior anodes for lithium ion batteries. *Nano Research* **2011**, 4, 290-296. **(Equally contributed first authors)**
6. Chen, H. T.; **Xu, J.**; Chen, P. C.; Fang, X.; Qiu, J.; Fu, Y.; Zhou, C. W., Bulk synthesis of crystalline and crystalline core/amorphous shell silicon nanowires and their application for energy storage. *ACS Nano* **2011**, 5, 8383-8390. **(Equally contributed first authors)**
7. Lee, D. H.; **Xu, J.**; Meng, Y. S., An advanced cathode for Na-ion batteries with high rate and excellent structural stability. *Physical Chemistry Chemical Physics* **2013**, 15, 9, 3304-3312. **(Equally contributed first authors)**
8. Rong, J. P.; Fang, X.; Ge, M. Y.; Chen, H. T.; **Xu, J.**; Zhou, C. W., Coaxial Si / anodic titanium oxide / Si nanotubes arrays for lithium-ion battery anodes. *Nano Research* **2013**, 6, 182-190.

9. **Xu, J.**; Lee, D. H.; Meng, Y. S., Recent advances in sodium intercalation positive electrode materials for sodium ion batteries, *Functional Materials Letters* **2013**, 6, 1.
10. **Xu, J.**; Lee, D. H.; Clement, R. J.; Yu, X.; Leskes, M.; Pell, A. J.; Pintacuda, G.; Yang, X.-Q.; Grey, C. P.; Meng, Y. S., Identifying the critical role of Li substitution in P2-Na<sub>x</sub>[Li<sub>y</sub>Ni<sub>z</sub>Mn<sub>1-y-z</sub>]O<sub>2</sub> (0 < x, y, z < 1) intercalation cathode materials for high energy Na-ion batteries. *Chemistry of Materials* **2014**, 26, 1260-1269.
11. Qu, B.; Ma, C.; Ji, G.; Xu, C.; **Xu, J.**; Meng, Y. S.; Wang, T.; Lee, J. Y., Layered SnS<sub>2</sub>-Reduced Graphene Oxide Composite – A High-Capacity, High-Rate, and Long-Cycle Life Sodium-Ion Battery Anode Material. *Advanced Materials*, **2014**. DOI: 10.1002/adma.201306314.
12. Zhao, J.; **Xu, J.**; Lee, D. H.; Dimov, N.; Meng, Y. S.; Okada, S.; Electrochemical and thermal properties of P2-type Na<sub>2/3</sub>Fe<sub>1/3</sub>Mn<sub>2/3</sub>O<sub>2</sub> for Na-ion batteries. *Journal of Power Sources* **2014**, 264, 235-239.
13. **Xu, J.**; Ma, C. Z.; Balasubramanian, M.; Meng, Y. S., Understanding Na<sub>2</sub>Ti<sub>3</sub>O<sub>7</sub> as an ultra-low voltage anode material for Na-ion battery. *Chemical Communications* **2014** (accepted).
14. Liu H. D.; **Xu, J.**; Meng, Y. S., Breaking through the limitation of energy / power density for Na-ion battery cathodes. **2014** (in preparation)
15. **Xu, J.**; Liu, H. D.; Meng, Y. S., High-power cathode material with O3 structure for Na-ion batteries. **2014** (in preparation)

## **ABSTRACT OF THE DISSERTATION**

Designing and Diagnosing Novel Electrode Materials for Na-ion Batteries:  
Potential Alternatives to Current Li-ion Batteries

by

Jing Xu

Doctor of Philosophy in Materials Science and Engineering

University of California, San Diego, 2014

Professor Ying Shirley Meng, Chair

Owing to outstanding energy density, Li-ion batteries have dominated the portable electronic industry for the past 20 years and they are now moving forward powering electric vehicles. In light of concerns over limited lithium reserve and rising lithium costs in the future, Na-ion batteries have re-emerged as potential alternatives for large scale energy storage. On the other hand, though both sodium and lithium are alkali metals sharing many chemical similarities, research on Na-ion batteries is still facing many challenges due to the larger size and unique bonding characteristics of Na ions.

In this thesis, a series of sodium transition metal oxides are investigated as cathode materials for Na-ion batteries. P2 -  $\text{Na}_{2/3}[\text{Ni}_{1/3}\text{Mn}_{2/3}]\text{O}_2$  is firstly studied with a combination of first principles calculation and experiment, and battery performance is improved by excluding the phase transformation region. Li substituted compound, P2- $\text{Na}_{0.8}[\text{Li}_{0.12}\text{Ni}_{0.22}\text{Mn}_{0.66}]\text{O}_2$ , is then explored. Its crystal / electronic structure evolution upon cycling is tracked by combining *in situ* synchrotron X-ray diffraction, *ex situ* X-ray absorption spectroscopy and solid state NMR. It is revealed that the presence of Li-ions in the transition metal layer allows increased amount of Na-ions to maintain the P2 structure during cycling. The design principles for the P2 type Na cathodes are devised based on this in-depth understanding and an optimized composition is proposed. The idea of Li substitution is then transferred to O3 type cathode. The new material, O3 -  $\text{Na}_{0.78}\text{Li}_{0.18}\text{Ni}_{0.25}\text{Mn}_{0.583}\text{O}_2$ , shows discharge capacity of 240 mAh/g, which is the highest capacity and highest energy density so far among cathode materials in Na-ion batteries.

With significant progress on cathode materials, a comprehensive understanding of  $\text{Na}_2\text{Ti}_3\text{O}_7$  as anode for Na-ion batteries is discussed. The electrochemical performance is enhanced, due to increased electronic conductivity and reduced SEI formation with carbon coating. Na full cell with high operating voltage is demonstrated by taking advantage of the ultra-low voltage of  $\text{Na}_2\text{Ti}_3\text{O}_7$  anode. The self-relaxation for fully intercalated phase,  $\text{Na}_4\text{Ti}_3\text{O}_7$ , is shown for the first time, which results from structural instability as suggested by first principles calculation.  $\text{Ti}^{4+} / \text{Ti}^{3+}$  is the active redox couple upon cycling based on XANES characterization. These findings unravel the underlying relation between unique properties and battery performance of  $\text{Na}_2\text{Ti}_3\text{O}_7$  anode, which should ultimately shed light on possible strategies for future improvement.

## Chapter 1. Motivation and Outline

Energy storage has become a growing global concern over the past decade as a result of skyrocketing energy demand, combined with drastic jump in the price of fossil fuels and the environmental consequences of their use. This leads to a strong call for environmentally responsible alternative sources, such as wind and solar. However, the increasing use of renewable energy sources are facing several crucial challenges, including modulating variable renewable resources from time to time, integrating them into the grid smoothly and safely, and balancing electricity generation / demand between peak and off-peak periods.<sup>1</sup> Therefore, the extension of battery technology to large-scale storage is of significant importance to the society.

Li-ion batteries (LIBs), the most common type of rechargeable batteries found in almost all portable electronic devices, are one of the possible solutions to these global concerns.<sup>2</sup> Lithium-based electrochemistry possesses several appealing attributes: Lithium is the lightest metallic element and has a very low redox potential ( $E_{\text{Li}^+/\text{Li}}^0 = -3.04$  V versus standard hydrogen electrode), which enables cells with high voltage and high energy density. Furthermore, Li ion has a small ionic radius, which is beneficial for diffusion in solids. Coupled with its long cycle life and rate capability, these properties have enabled Li-ion technology to capture the portable electronics market.<sup>3</sup>

In addition to the rapidly rising demand for LIBs as a major power source in portable electronic devices, LIB has become the prime candidate to power the next generation of electric vehicles and plug-in electric vehicles. Nevertheless, with the likelihood of enormous consumption of limited lithium resources, concerns over

lithium supply – but mostly its cost – have arisen. Many global lithium reserves are located in remote or in politically sensitive areas.<sup>4,5</sup> Even if extensive battery recycling programs were established, it is possible that recycling could not prevent this resource depletion in time.<sup>3</sup> Moreover, increasing lithium utilization in medium-scale automotive batteries will ultimately push up the price of lithium compounds, thereby making large-scale storage prohibitively expensive.

The use of sodium instead of lithium in batteries could mitigate the feasible shortage of lithium in an economic way, owing to the high abundance and broad distribution of sodium sources. Furthermore, with very suitable redox potential ( $E_{\text{Na}^+/\text{Na}}^0 = -2.71$  V versus standard hydrogen electrode; only 0.3 V above that of lithium), rechargeable Na-ion batteries (NIBs) also hold much promise for energy storage applications. Since sodium is located just below lithium in the s block, similar chemical approaches including synthetic strategies, intercalation / alloying / conversion chemistries, and characterization methods utilized in electrode materials for LIBs could be applied to develop electrode materials for NIBs more efficiently.<sup>6</sup> On the other hand, the larger size and different bonding characteristics of Na ions influence the thermodynamic / kinetic properties of NIBs, which leads to unexpected behaviors in electrochemical performance and reaction mechanism, compared to LIBs. Therefore, my Ph. D research mainly focused on revealing the underlying electrochemical mechanisms of the electrode materials for NIBs and making critical breakthroughs in energy / power densities for both cathode and anode materials.

The objective of the first part of my thesis is to investigate the effects of transition metals and alkali ions on the phase stability and ionic diffusivity in the layered

intercalation compounds upon cycling. The objective of the second part is to improve the capacity retention and rate capability sodium titanates and unravel the fundamental reasons for their ultra low voltage and intrinsic problems. **Chapter 2** gives a general introduction of alkali-ion batteries. **Chapter 3** briefly introduces advanced characterization tools I use in my research including synchrotron X-ray scattering and first principles calculations. **Chapter 4** investigates P2 –  $\text{Na}_x[\text{Ni}_{1/3}\text{Mn}_{2/3}]\text{O}_2$  ( $0 < x < 2/3$ ) as cathode for NIBs and report the phase transformation, Na-ion orderings and diffusion for this family of materials. **Chapter 5** discusses the critical role of Li substitution in P2- $\text{Na}_x[\text{Li}_y\text{Ni}_z\text{Mn}_{1-y-z}]\text{O}_2$  ( $0 < x, y, z < 1$ ) in the structural stability for P2 layered compounds, and proposes design principles for high-energy electrode materials. In **chapter 6**, the idea of Li substitution is transferred from P2 to O3 type compounds and it is demonstrated that the phase changes triggered by layer shifting could be prohibited through materials optimization. **Chapter 7** explains the in-depth understanding on  $\text{Na}_2\text{Ti}_3\text{O}_7$  as an ultra-low voltage anode material for NIBs. The performance as well as the intrinsic problems for this anode candidate is illustrated. Na full cell are fabricated with the cathode and anode in my research. **Chapter 8** summarizes the overall work and plan for the future research.

## Chapter 2. Introduction of the alkali-ion batteries

### 2.1. The configuration of the alkali-ion battery

Batteries convert chemical energy into electrical energy. In practice, it usually consists of several electrochemical cells that are connected in parallel and / or in series to meet the voltage / current requirements. As shown in Figure 2.1, each electrochemical cell is basically composed of a positive electrode, a negative electrode, and a membrane separator between the two electrodes. Both electrodes and the separator are immersed in the electrolyte. Each of the two electrodes has active materials on the current collectors. In the alkali-ion batteries, the active materials allow alkali ions to be inserted or extracted. The electrolyte and separator are conductive to ions but resistant to electrons, allowing alkali ions but not electrons to pass between the two electrodes through the electrolyte.

The positive electrode, which is also called as “cathode”, is a thin film consisting of an active material, a conductive agent, and a binder. As stated above, the active materials could allow alkali ions to be inserted or extracted through intercalation or conversion reactions. For Li-ion batteries (LIBs), layered  $\text{LiTMO}_2$ , spinel  $\text{LiTM}_2\text{O}_4$  and olivine  $\text{LiTMPO}_4$  (TM = transition metal), are the most extensively investigated. Table 2.1 summarizes three typical cathode materials for LIBs. For Na-ion batteries (NIBs), a lot of attentions have been paid on layered  $\text{NaTMO}_2$  and NASICONs as active materials. As most electrode materials are semiconductors or insulators, conductive additives such as carbon black or acetylene black are essential to enhance the electronic conductivity. Polymer binders such as polytetrafluoroethylene (PTFE) or poly-vinylidene fluoride (PVDF) are utilized to adhere the active materials and conductive additives together with

necessary mechanical strength. Upon cycling, the volume change of the active materials could be considerable, giving rise to the damage in the electrode intactness. As a result, the electric contact and the active materials will get lost. Therefore, a proper binder is of great importance in maintaining the electrode intactness during the cycling and improving the cycling accordingly.

The most widely used materials for the negative electrode, which is also called as “anode”, are carbon-based materials such as graphite or Mesocarbon Microbead (MCMB). Graphite’s layered structure allows Li ions to intercalate into interlayers. The specific capacity of graphite is 372 mAh/g and the average voltage about 0.1 – 0.2 V vs. Li / Li<sup>+</sup>. Graphite as an anode shows very good cycling with electrolytes containing ethylene carbonate because these electrolyte solvents decompose on the carbon-based anode, forming a protective film called the solid electrolyte interphase (SEI).<sup>7, 8</sup> For Na-ion batteries, Na ion can be barely intercalated into interlayers in graphite mostly due to its large ionic size. Hard or nanoporous carbons, however, contain pores between randomly stacked layers, where both Na and Li ions can be inserted. Silicon, Tin, and Antimony are three of the promising candidates for anode materials in LIBs / NIBs. However, these materials are based on alloy reactions, so after fully insertion, the active materials will undergo a dramatic volume change.<sup>9, 10</sup> During cycling, the large volume change will lead to the loss of mechanical integrity through the electrode. A better choice of binder, such as Carboxyl methyl cellulose (CMC), can improve the mechanical integrity over cycling and give better performance retention than PVDF.<sup>11, 12</sup>

The separator is a polymer membrane separating the two electrodes, which allows ionic flow but prevents electric contact of the electrodes. The separator should be

chemically inert to both electrodes and the electrolyte. Commonly used separators include porous films of Polyethylene (PE), Polypropylene (PP), and glass fibers (GFs). Trilayer separators (PP/PE/PP) offer advantages by combining the lower melting temperature of PE with the high-temperature strength of PP.<sup>13</sup>

The electrolyte is a solution of alkali salts and solvent. For LIBs and NIBs, the active nature of the strongly oxidizing cathode and the strongly reducing anode rules out the use of any aqueous electrolyte. This is because the reduction of protons and the oxidation of anions such as  $\text{OH}^-$  generally occur within 2.0 – 4.0 V vs. alkali metal,<sup>14</sup> while the charged potentials of the anode and cathode are around 0.0-0.2 V and 3.0-4.5 V respectively. On the other hand, non-aqueous solvents need polar groups such as carbonyl (C=O) or ether-linkage (-O-) to dissolve the salt sufficiently.<sup>7</sup> So carbonates such as ethylene carbonate (EC), propylene carbonate (PC), dimethyl carbonate (DMC) and diethyl carbonate (DEC) are most commonly used. As for the salts, the choices are relatively limited because the solubility requirement in low dielectric nonaqueous solvent, together with the anodic stability. Among most of salts which have been intensively studied including  $\text{LiClO}_4$ ,  $\text{LiAsF}_6$ , and  $\text{LiBF}_4$ ,  $\text{LiPF}_6$  stands out owing to its well-balanced properties.<sup>15-17</sup>

The current collectors serve as the substrates for the electrode, providing support and conductivity.<sup>18</sup> In LIBs, aluminum is the choice for the cathode, due to its low cost, good electric conductivity, and anodic stability up to 5 V vs.  $\text{Li/Li}^+$ . Figure 2.2 (a) shows the profile and cyclic voltammograms of Al metal in 1 M  $\text{LiPF}_6$  in EC:DMC = 1:1 as an electrolyte. It is seen that the anodic current maintains a very low level from 1.0 V up to 5.0 V vs.  $\text{Li/Li}^+$ , indicating a good anodic stability within the potential window of the

positive electrode. Between 0 V to 1.0 V vs. Li/Li<sup>+</sup>, however, there is a strong redox reaction corresponding to the Li-Al alloying and de-alloying. This hinders the use of an Al foil as a current collector for the anode. Copper, however, shows significantly high anodic and cathodic current between 1.5 V to 5.0 V vs. Li/Li<sup>+</sup> but very low current between 0 V to 1.0 V (Figure 2.2(b) from ref. 9).<sup>19</sup> The excellent cathodic stability makes Cu a good choice for the current collector of the anode in LIBs. There are no systematic investigations on the current collectors for Na ion batteries at this point.

## 2.2. Charging and discharging processes in alkali-ion batteries

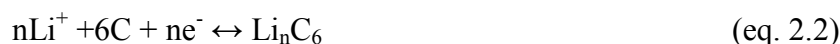
The open circuit voltage across an alkali-ion battery is decided by the difference in the chemical potentials of alkali ions on the two electrodes. Therefore, the selection of the two electrodes materials determines the open circuit voltage of the battery. The cathode has a lower chemical potential of alkali ions and thus a higher electric potential. Accordingly, the anode has a higher chemical potential and a lower electric potential.

Charging and discharging process occurs through the intercalation / deintercalation at the electrode, which is driven by the increase / reduction of the electrochemical potential of the alkali ion. As LIB and NIB are similar, here we just use a typical LIB as an example. During the charging process, the Li ions are deintercalated from the cathode, which is a layered LiTMO<sub>2</sub> compound:



The Li ions are driven by the electric force from the cathode to the anode through the electrolyte, and the electrons move through the external circuit performing work. At

the anode, the Li ions intercalate into the active material, which is usually Graphite in LIBs:



The above reactions at both electrodes are reversible. Upon the discharging process, the reactions at both electrodes occur in the reverse direction. Li ions are de-intercalated from the anode and intercalated into the cathode. Figure 2.1 shows the ionic and electronic flow at the charging and discharging process.

### 2.3. Practical criteria for the electrode material designs in alkali-ion batteries

The electrode materials have crucial effect on the performance of an alkali-ion battery, since the electrochemical reaction in a battery is intimately tied to the electrode materials. The key parameters for electrode materials include voltage, gravimetric and volumetric energy density, power density, cycle life and cost, etc.

High voltage and capacity are desired to improve the energy density. The capacity is based on how much the alkali ion could be hosted in the electrode material. The voltage is not only decided by the selection of electrode materials but also limited by the stability of the electrolyte. The current electrolyte in LIBs today requires the voltage to be kept below 4.5 V to avoid substantial reactions between the electrolyte and the electrode.<sup>2</sup>

The gravimetric energy density, defined as the energy per unit weight (Wh/kg), is the product of the voltage and the specific capacity. If one mole of electrode material can supply  $x$  mole of electrons, then the specific capacity is  $(x \cdot F / M) \times 1000 / 3600$  mAh/g.  $F$  is the Faraday's constant, and  $M$  is the molar weight of the electrode material. Besides the specific energy density, volumetric energy density is the energy per unit volume

(Wh/L). As today's electronic devices require more energy within a limited size, volumetric energy density becomes more and more significant. Higher volumetric energy density can also cut down costs by reducing the use of separators, electrolytes and current collectors.

The power density of a battery is calculated as the power per unit weight (W/kg). If the internal resistance is  $r$  and the load on the cell is  $R$ , the current is  $I = V_{oc} / (R + r)$  and the output power can be determined by the following equation:

$$P = V_{oc} \cdot I - I^2 \cdot r = V_{oc}^2 \cdot R / (R+r)^2 \quad (\text{eq. 2.3})$$

where  $V_{oc}$  is the open circuit voltage. With higher current, more power will be distributed to the internal resistance and generates heat inside the cell, which may cause safety issues. When the battery is discharging at high rate with low external load  $R$ , the output power is mainly restricted by  $r$ .

The cycle life is defined as the number of charging /discharging cycles the battery can perform before the specific capacity falls below a certain percentage (such as 80%) of the initial capacity.<sup>20</sup> The cycle life relies on various factors including the structural stability of the electrode materials, the formation of the SEI layer and its stability, the chemical stability of the electrolyte, and the mechanical integrity.

## **2.4. Recent progress in electrode materials for Na-ion batteries**

### **2.4.1. Layered metal oxides as cathode materials**

It is no wonder that sodium layered oxide compounds ( $\text{Na}_x\text{MO}_2$ ) have drawn significant attention as cathode materials in Na-ion batteries considering that their Li analogues have been comprehensively understood for last two decades. The layered

$\text{Na}_x\text{MO}_2$  materials can be categorized into two major groups which are P2 and O3 type. The first letter “P” or “O” refers to the nature of the site occupied by alkali ion (prismatic or octahedral), and “2” or “3” refers to the number of transition metal layers in the repeat unit perpendicular to the layering.<sup>21</sup> The structural properties of  $\text{Na}_x\text{MO}_2$  have been studied in 70’s by Delmas *et al.*,<sup>22, 23</sup> and  $\text{Na}_x\text{CoO}_2$  has been revealed to show reversible phase transformations by electrochemical charge and discharge demonstrating the feasibility of  $\text{Na}_x\text{MO}_2$  as a cathode material.<sup>24</sup> However, limited efforts have been spent on Na-ion batteries during the past two decades due to the tremendous success of Li-ion batteries. Several studies on P2 or O3 type  $\text{Na}_x\text{CrO}_2$ ,<sup>25</sup>  $\text{Na}_x\text{MnO}_2$ ,<sup>26</sup> and  $\text{Na}_x\text{FeO}_2$ <sup>27</sup> have been conducted in early 80’s to 90’s, but the researches were limited to the structural studies up to 3.5 V versus sodium upon the 1st cycle mostly due to the instability of the electrolyte.

Recent studies on O3- $\text{Na}_x\text{MO}_2$  compounds started to reveal the fact that they can be utilized as a cathode electrode with excellent electrochemical properties in Na-ion cells.  $\text{NaCrO}_2$  was investigated by Komaba *et al.*, and showed 120 mAh  $\text{g}^{-1}$  of specific capacity near 2.9 V.<sup>28, 29</sup> Interestingly,  $\text{NaCrO}_2$  exhibited better electrochemical performances over that of  $\text{LiCrO}_2$  due to larger  $\text{CrO}_2$  inter-slab distance in Na compound. The O3- $\text{NaNi}_{0.5}\text{Mn}_{0.5}\text{O}_2$  electrodes delivered 105 mAh  $\text{g}^{-1}$  at 1C (240 mA  $\text{g}^{-1}$ ) and 125 mAh  $\text{g}^{-1}$  at C/30 (8 mA  $\text{g}^{-1}$ ) in the voltage range of 2.2 - 3.8 V and displayed 75% of the capacity after 50 cycles.<sup>29, 30</sup> The Fe-substituted O3- $\text{Na}[\text{Ni}_{1/3}\text{Fe}_{1/3}\text{Mn}_{1/3}]\text{O}_2$  exhibited the specific capacity of 100 mAh  $\text{g}^{-1}$  (avg. V: 2.75 V) with smooth voltage profiles.<sup>31</sup> The phase transformation was observed in the fully charged (~ 4.0 V) electrode but original R-3m phase was completely restored at the following discharge. The isostructural

compound,  $\text{Na}[\text{Ni}_{1/3}\text{Mn}_{1/3}\text{Co}_{1/3}]\text{O}_2$ , showed reversible intercalation of 0.5 Na-ions leading to the specific capacity of  $120 \text{ mAh g}^{-1}$  in the voltage range of 2.0 - 3.75 V.<sup>32</sup> In-situ XRD revealed the sequential phase evolutions (O3, O1, P3 and P1) composed of biphasic and monophasic domains upon the Na-ions extraction associated with stair-like voltage profiles.

In addition to the O3 phase, P2 structured materials have been extensively studied since larger Na-ion is stable in more spacious prismatic site. Recently, P2- $\text{Na}_x\text{CoO}_2$  has been reinvestigated by Berthelot *et al.* and reported to reversibly operate between  $0.45 \leq x \leq 0.90$ .<sup>33</sup> The in-situ XRD indicated that nine single-phase domains with narrow sodium composition ranges were observed due to distinctive  $\text{Na}^+$ /vacancy orderings. P2- $\text{Na}_x\text{VO}_2$  was also revisited and precise phase diagram determined from electrochemical Na-ions intercalation and extraction was reported.<sup>34</sup> Four different monophasic domains due to different  $\text{Na}^+$ /vacancy ordering between  $\text{VO}_2$  slabs were evidenced within the x range of 0.5 ~ 0.8 leading to the superstructures. The Mn substituted P2- $\text{Na}_{2/3}[\text{Co}_{2/3}\text{Mn}_{1/3}]\text{O}_2$ , where  $\text{Co}^{3+}$  and  $\text{Mn}^{4+}$  coexist, was investigated by the same group.<sup>35</sup> Unlike its analogue, P2- $\text{Na}_{2/3}\text{CoO}_2$ , P2- $\text{Na}_{2/3}[\text{Co}_{2/3}\text{Mn}_{1/3}]\text{O}_2$  displayed only one voltage step at  $\text{Na}_{1/2}[\text{Co}_{2/3}\text{Mn}_{1/3}]\text{O}_2$  composition. A study by Lu *et al.* demonstrated that the P2- $\text{Na}_{2/3}[\text{Ni}_{1/3}\text{Mn}_{2/3}]\text{O}_2$  can reversibly exchange 2/3 of Na-ions in Na cells leading to the capacity of  $160 \text{ mAh g}^{-1}$  between 2.0 ~ 4.5 V.<sup>36, 37</sup> The phase transformation of P2 to O2 at the high voltage region was evidenced by in-situ XRD and it caused the significant capacity fading and poor rate capability. However, when this material was recently revisited by Lee *et al.*, the electrodes delivered  $89 \text{ mAh g}^{-1}$  at C/20 and 85% of capacity at 1C was obtained with excellent cycling performances by excluding the phase

transformation region.<sup>38</sup> It was revealed that the diffusivity of Na-ions in P2 structure is higher than that in the corresponding O3 structured Li compounds. Li substituted  $\text{Na}_{1.0}\text{Li}_{0.2}\text{Ni}_{0.25}\text{Mn}_{0.75}\text{O}_2$  was studied by Kim *et al.* and displayed 95 – 100 mAh g<sup>-1</sup> of specific capacity in the voltage range of 2.0 ~ 4.2 V, excellent cycling and rate capabilities<sup>39</sup>. Recently, Yabuuchi *et al.* reported that  $\text{Na}_{2/3}[\text{Fe}_{1/2}\text{Mn}_{1/2}]\text{O}_2$  delivers the capacity of 190 mAh g<sup>-1</sup> between 1.5 to 4.2 V.<sup>40</sup> The energy density is estimated to be 520 mWh g<sup>-1</sup>, which is comparable to that of  $\text{LiFePO}_4$  (530 mWh g<sup>-1</sup>). They evidenced that highly reversible phase transformation of P2 to OP4 occurring above 3.8 V and  $\text{Fe}^{3+}/\text{Fe}^{4+}$  redox couple is electrochemically active in Na-ion cells.

#### 2.4.2. Polyanion compounds as cathode materials

Recently, polyanion compounds have attracted considerable attention for Na-ion batteries. Various crystal structures are demonstrated to be able to accommodate Na-ions due to their open channels. In polyanion compounds, tetrahedral polyanion structure units  $(\text{XO}_4)^{n-}$  (X = P or S) are combined with  $\text{MO}_6$  (M = transition metal) polyhedra. Due to the strong covalent bonding in  $(\text{XO}_4)^{n-}$ , polyanion cathode materials usually possess high thermal stability, which make them more suitable for large-scale energy applications. Moreover, since the operation voltage is influenced by local environment of polyanions, the voltage of a specific redox couple can be tuned for this type of materials.

Compounds based on the 3D structure of NASICON are extensively studied for their structural stability and fast ion conduction, initially as solid electrolytes<sup>41-43</sup> and more recently as insertion materials.<sup>44-51</sup> The general formula is  $\text{A}_x\text{MM}'(\text{XO}_4)_3$ , in which corner-shared  $\text{MO}_6$  (or  $\text{M}'\text{O}_6$ ) and  $\text{XO}_4$  polyhedra form a framework with large Na

diffusion channels.<sup>52</sup> In 1987 and 1988, Delmas *et al.* demonstrated that NASICON-type compounds,  $\text{NaTi}_2(\text{PO}_4)_3$ , can be electrochemically active with Na in a reversible manner<sup>44, 45</sup>. Later  $\text{NaNbFe}(\text{PO}_4)_3$ ,  $\text{Na}_2\text{TiFe}(\text{PO}_4)_3$  and  $\text{Na}_2\text{TiCr}(\text{PO}_4)_3$  were explored.<sup>47, 49</sup> Since then, most studies of this family of compounds were focused on Li-ion batteries, because the cell performance was generally poor in Na-ion batteries. Sodium intercalation in  $\text{Na}_3\text{V}_2(\text{PO}_4)_3$  was first synthesized in 2002 by Yamaki *et al.*<sup>53</sup>. The existence of two voltage plateau at 1.6 and 3.4 V vs.  $\text{Na}/\text{Na}^+$  allowed using this phase not only as cathode but also anode in a symmetric cell. However, the cycling stability of this symmetric cell was relatively poor.<sup>50</sup> Recently, several methods have been utilized to coat carbon on  $\text{Na}_3\text{V}_2(\text{PO}_4)_3$  to improve the battery performance.<sup>51, 54</sup> Among all, Balaya *et al.* reported the excellent cycling stability and superior rate capability<sup>55</sup>, which was attributed to facile sodium ion diffusion in the nano-sized particles embedded in a conductive matrix.

Unlike the olivine  $\text{LiFePO}_4$ <sup>56, 57</sup>, the sodium analogue,  $\text{NaFePO}_4$ , was not extensively investigated. The olivine  $\text{NaFePO}_4$  can be obtained by extracting Li-ions out of  $\text{LiFePO}_4$  and subsequently inserting Na-ions into  $\text{FePO}_4$ <sup>58</sup>. Upon Na-ion extraction, two different plateaus were clearly observed in the voltage-composition curve, resulted from two successive first-order transitions concomitant with the formation of an intermediate  $\text{Na}_{0.7}\text{FePO}_4$ <sup>59, 60</sup>. On the other hand, only one plateau is observed upon discharge, indicating that the charge and discharge process might go through different reaction paths. Recently, Cabanas *et al.* demonstrated that the Na insertion into  $\text{FePO}_4$  occurred via an intermediate phase which buffers the internal stresses.<sup>61</sup> Besides the pure iron olivine, the  $\text{NaFe}_{0.5}\text{Mn}_{0.5}\text{PO}_4$  was synthesized by a molten salt reaction.<sup>62</sup> Compared

with NaFePO<sub>4</sub>, a sloping profile over the entire voltage range was displayed in Na-ion batteries. The origin of this solid solution behavior was not clarified.

In the quest for new cathode materials, various structures with different polyanion groups are demonstrated to be promising candidates. The family of sodium vanadium fluorophosphates, NaVPO<sub>4</sub>F<sup>63</sup>, Na<sub>3</sub>V<sub>2</sub>(PO<sub>4</sub>)<sub>2</sub>F<sub>3</sub><sup>64-66</sup> and Na<sub>1.5</sub>VOPO<sub>4</sub>F<sub>0.5</sub><sup>67</sup> have attracted interests due to high potential of the V<sup>3+</sup>/V<sup>4+</sup> redox reaction. Though the electrochemical activities of NaVPO<sub>4</sub>F have been demonstrated in Na-ion batteries<sup>63</sup>, no long-term electrochemical tests have been reported so far. Na<sub>3</sub>V<sub>2</sub>(PO<sub>4</sub>)<sub>2</sub>F<sub>3</sub> was first reported by Meins *et al.*<sup>64</sup> and its good cyclability was achieved recently.<sup>66</sup> Concerning Na<sub>1.5</sub>VOPO<sub>4</sub>F<sub>0.5</sub>, Sauvage *et al.* claimed that a reversible capacity of 87 mAh g<sup>-1</sup> was shown by galvanostatic cycling of the material at C/2.<sup>67</sup> The compound was comprised of layers of alternating [VO<sub>5</sub>F] octahedral and [PO<sub>4</sub>] tetrahedral sharing O vertices. Moreover, Na<sub>2</sub>FePO<sub>4</sub>F was first studied by Nazar *et al.*, in which two-dimensional iron phosphate sheets host two Na-ions.<sup>68</sup> Later, the isothermal synthesis was applied to prepare this compound, so that the morphology could be controlled.<sup>69</sup> A reversible two-plateau behavior was displayed in the electrochemical profiles versus Na metal, and the discharge capacity was over 100 mAh g<sup>-1</sup> during 10 cycles. With regard to pyrophosphate, a variety of Na-based pyrophosphates are investigated.<sup>70-72</sup> While these pyrophosphate materials adopt different crystal structures depending on transition metals, most of them contain open frameworks that could facilitate efficient diffusion of Na-ions. Recently, a new version of Fe-based pyrophosphate, Na<sub>2</sub>FeP<sub>2</sub>O<sub>7</sub>, was firstly reported as the cathode materials.<sup>72</sup> This material delivered 90 mAh g<sup>-1</sup> of reversible capacity with two distinct plateaus at 2.5 V and 3.1 V respectively. Excellent thermal stability was also observed up

to 500 °C, indicating that the  $\text{Na}_2\text{FeP}_2\text{O}_7$  could be a promising candidate for positive electrode material in Na-ion batteries. In addition to phosphate-based compounds, sodium transition metal fluorosulphates,  $\text{NaMSO}_4\text{F}$ , exhibit high Na-ion ionic conductivity and have been tested for the electrochemical activities in Na-ion battery. In  $\text{NaFeSO}_4\text{F}$ , Na-ions reside in the spacious tunnels constructed by corner-shared  $\text{FeSO}_4\text{F}$  frameworks.<sup>73</sup>  
<sup>74</sup> These materials were demonstrated to work reversibly in hybrid Li-ion batteries; however no decent reversibility has obtained in Na-ion batteries.<sup>75, 76</sup>

### 2.4.3. Anode materials

Compared with tremendous progress in cathode direction, the development of suitable anode materials for Na-ion batteries remains a considerable challenge.<sup>52, 77</sup> Graphite cannot be used as anode, since it is unable to intercalate Na ion reversibly.<sup>78, 79</sup> Metallic Na is also ruled out, because it forms dendrites easily and has an even lower melting point than Li. Hard carbons is shown to insert and de-insert Na ions, delivering capacities about 200–300  $\text{mAh g}^{-1}$ .<sup>79-81</sup> However, the reversibility for carbonaceous materials still requires further improvement.<sup>82, 83</sup> Na-alloys are proposed as possible alternatives, as they can potentially provide higher specific capacities.<sup>84-88</sup> These alloys, however, suffer from large volume changes upon uptake / removal of Na, in analogy to Li-alloys.<sup>89</sup> Another emerging class of materials is transition metal oxides. For example,  $\text{NaVO}_2$  is shown to yield a reversible capacity (e.g.  $<130 \text{ mAh g}^{-1}$ ) at C/100 current rate, but its operating voltage is at 1.5 V vs.  $\text{Na}^+/\text{Na}$ , leading to a low energy density.<sup>90</sup> Ti-based oxides are suggested to be an attractive alternative, considering that  $\text{Li}_4\text{Ti}_5\text{O}_{12}$  is

one of the few commercialized anode materials in Li-ion battery.<sup>91, 92</sup> Several different sodium titanates have been explored as anodes for Na-ion battery.<sup>93-97</sup>

Chapter 2, in part, is a reprint of the material “Recent advances in sodium intercalation positive electrode materials for sodium ion batteries” as it appears in the Functional materials letters, Jing Xu, Dae Hoe Lee, Ying S. Meng, 2013, 6, 1330001. The dissertation author was the co-primary investigator and author of this paper. The author wrote the polyanion cathode for the Na-ion battery part.

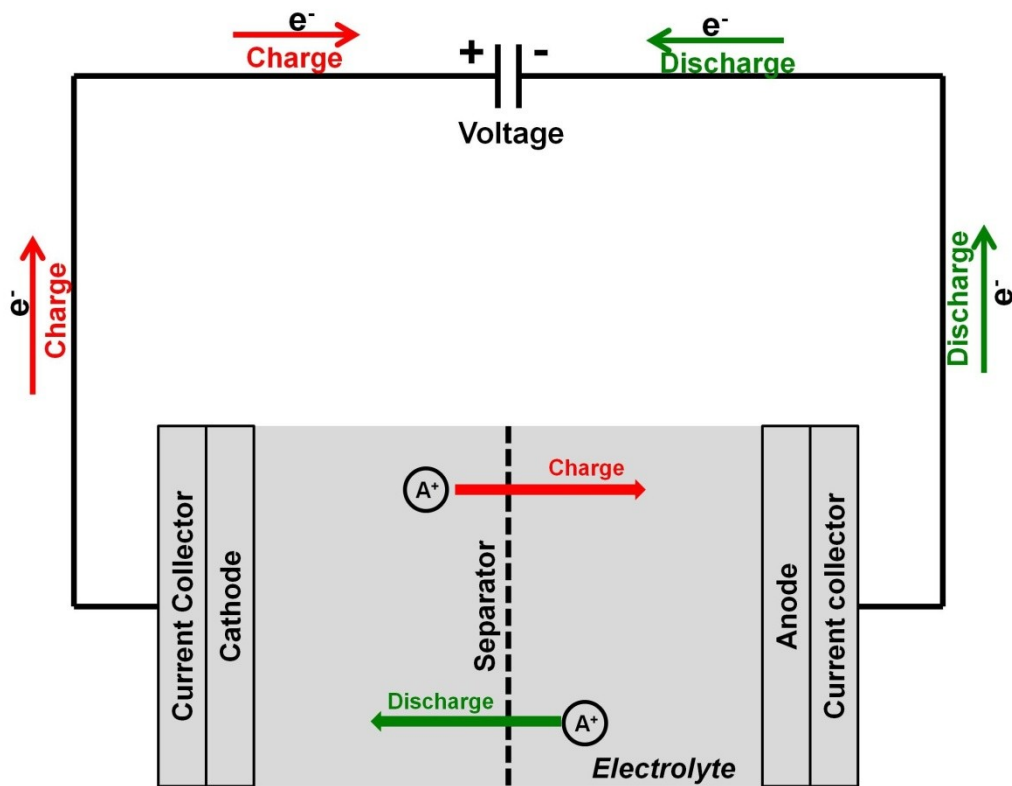
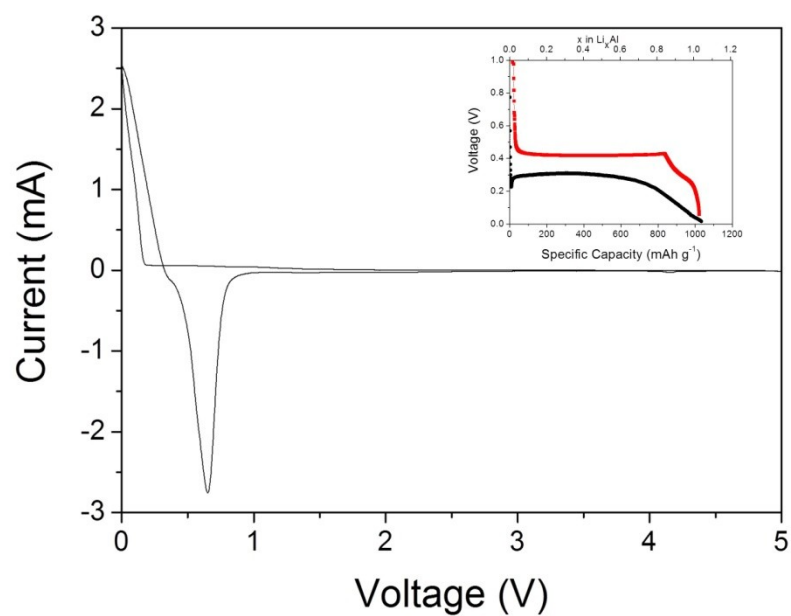


Figure 2.1 Schematic of a rechargeable alkali-ion battery.  $A^+$  is the alkali ion.

(a)



(b)

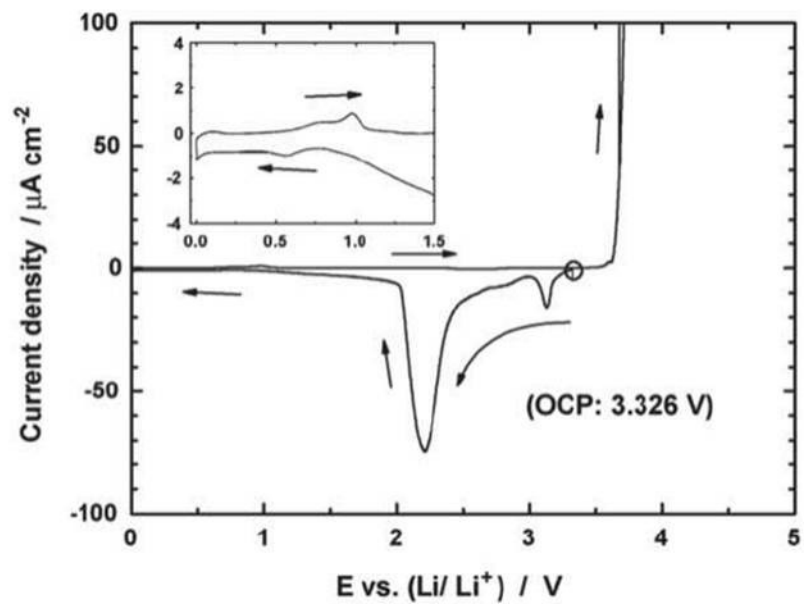


Figure 2.2 Cycling voltammograms of (a) Al and (b) Cu<sup>19</sup> in LIBs respectively.

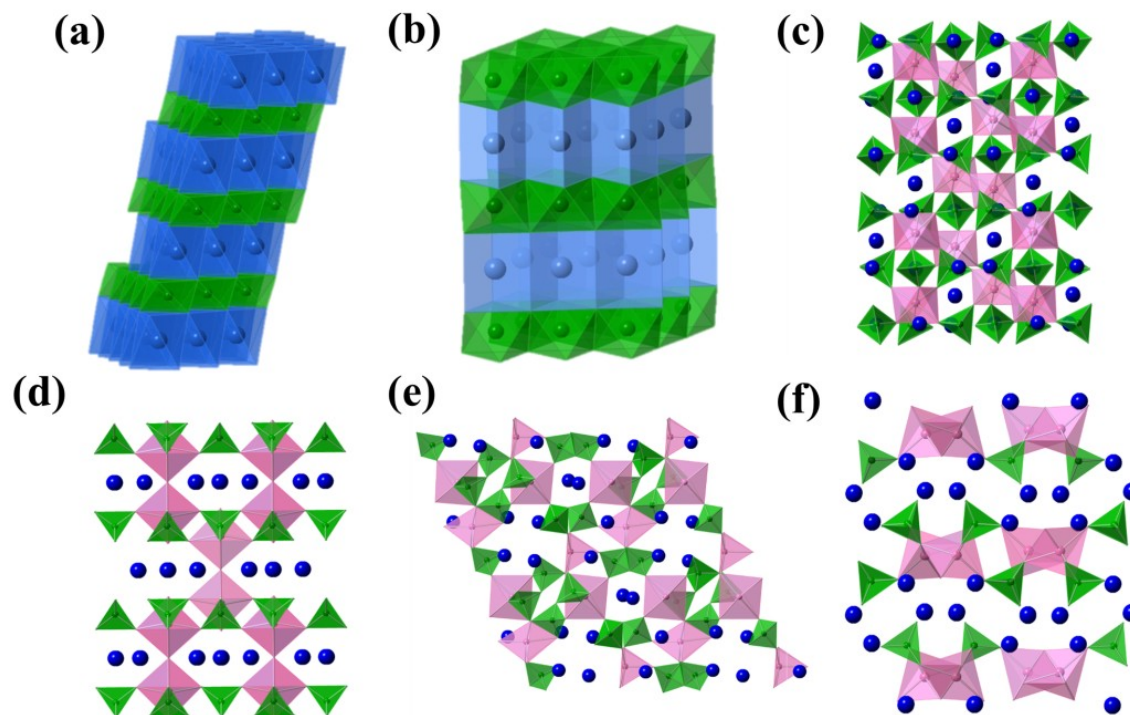


Figure 2.3 Schematics of crystal structures of (a) O3, (b) P2, (c) NASICON, (d)  $\text{Na}_{1.5}\text{VOPO}_4\text{F}_{0.5}$ , (e)  $\text{Na}_2\text{FePO}_4\text{F}$  and (f)  $\text{Na}_2\text{FeP}_2\text{O}_7$ <sup>98</sup>

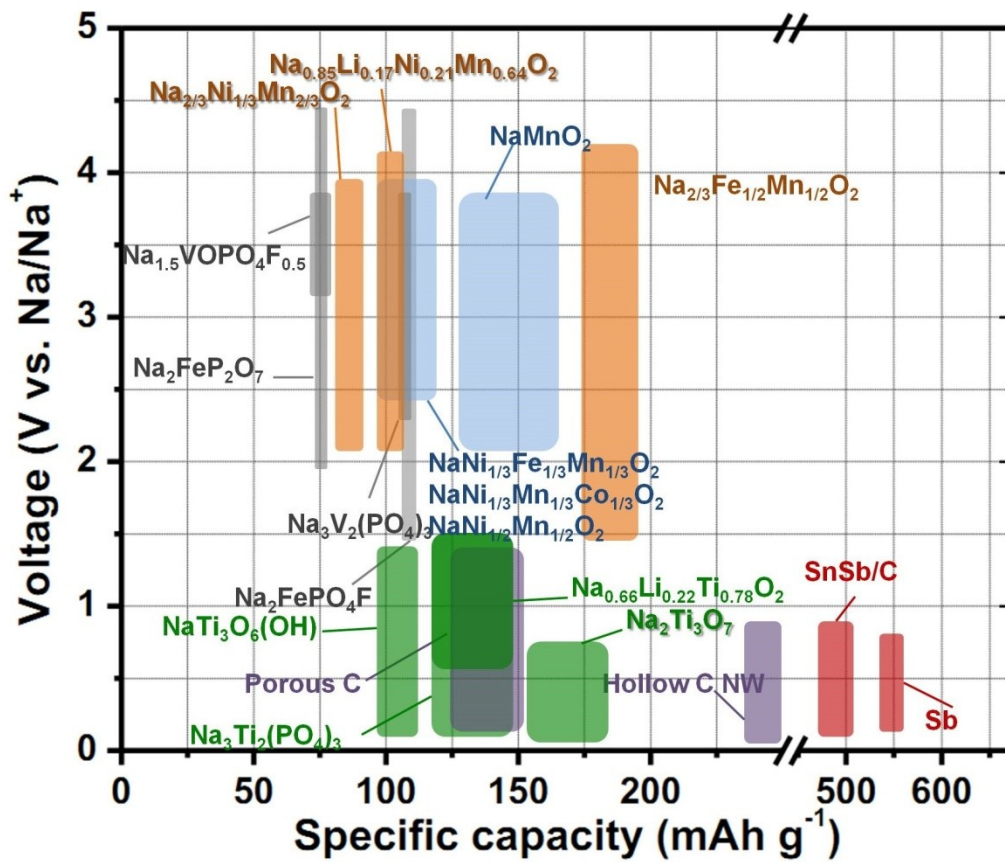


Figure 2.4 Summary of specific capacity, operating voltage range and energy density of the intercalation cathode materials for Na-ion batteries.

Table 2.1 Summary of three typical positive electrode materials for LIBs

	Space group	Structure	Ionic diffusion dimension	Ave. voltage (Volt)	Practical capacity (mAh/g)	Gravimetric energy density (Wh/kg)	Volumetric energy density (Wh/L)
$\text{LiCoO}_2$	R-3m	Layered	2D	4.0	155	620	3100
$\text{LiMn}_2\text{O}_4$	Fd3m	Spinel	3D	4.1	120	492	2066
$\text{LiFePO}_4$	Pnma	Olivine	1D	3.4	160	544	1959

## **Chapter 3. Advanced characterization tools**

### **3.1. Synchrotron X-ray scattering techniques**

#### **3.1.1. Synchrotron radiation**

In the past ten years, the skyrocketing development in LIB has significantly benefited from increasingly sophisticated characterization techniques, which enable a detailed control and comprehensive understanding at the atomic level of battery materials. Among recent advanced characterization tools, a leading role has been certainly played by those exploiting synchrotron radiation sources (SRSs).<sup>99</sup> The key features of SRS in relation to materials studies are the wavelength tunability, which allow distinguishing different elements and oxidation states, and the high brightness and excellent vertical collimation of the source, which make possible the construction of diffractometers with unparalleled angular and spatial resolution.

In SRSs, electrons moving close to the speed of light within an evacuated pipe are guided around a closed path of 100 – 1000 meter circumference by vertical magnetic fields. Wherever the trajectory bends, the electrons accelerate (change velocity vector). Accelerating charged particles emit electromagnetic radiation, and the fact that the electrons are moving at nearly the speed of light implies that relativistic effects are important. In this case, they profoundly affect the properties of the emitted radiation: the average energy of the X-rays and the total radiated power are more intense, and the radiation pattern becomes more directional, making it much easier to employ X-ray optics such as monochromators. In the new-generation of SRSs, “insertion devices” such

as “wigglers” and “undulators” also are used to further enhance the characteristics of the emitted radiation.

### 3.1.2 In situ synchrotron X-ray diffraction (SXRD)

XRD is a technique based on scattering of X-rays by electrons of the constituent atoms of a crystal. When an X-ray beam impinges on a crystalline material at an incident angle  $\theta$ , a fraction of the X-ray beam is scattered by the atoms on the surface, and the fraction not scattered reaches deeper atoms in the crystal structure where then further interaction is happened. The constructive interference of the scattered X-rays represents the diffracted beam, which behaves as a specular reflection from a regular plane of atoms in the crystal.<sup>100</sup> Therefore, the diffracted beam is generated only if certain geometrical conditions are satisfied, according to the Bragg equation:

$$N\lambda = 2d\sin\theta \quad (\text{eq. 3.1})$$

where  $\lambda$  is the wavelength of the X-ray beam,  $d$  the crystal interplanar spacing,  $n$  an integer that represents the orders of reflection, and  $\theta$  the angle of incidence or reflection of the X-ray beam. The ideal crystal size for Bragg reflection usually lies in the range  $10^{-5}$  to  $10^{-7}$  m, and if the crystal size is smaller than about  $10^{-8}$  m, the crystallites are too small for diffraction at Bragg angles, so that their only constructive interferences are limited to small angles.<sup>101</sup>

As phase transformations are frequently encountered in electrode materials upon cycling, the use of in situ XRD has provided valuable information on reaction paths and rates, nature of crystalline and amorphous intermediate product phases, lattice evolution, stacking faults formation and growth. Although a conventional laboratory diffractometer

with Cu  $K\alpha_1$  X-ray tube can be used to conduct in situ measurements, the quality of the measured signal may be adversely affected as a consequence of the attenuation of the incident X-ray beam within the batteries. On the other hand, the principal features that distinguish synchrotron X-rays from conventional X-rays, are the high intensity, the excellent vertical collimation, and the white (continuous) spectral distribution. Therefore, the use of synchrotron radiation permits XRD measurements to be performed with high, spatial and time resolution through the use of focused and intense high energy X-rays that are capable of penetrating a wide range of in situ sample environments.<sup>102</sup> The high intensity of synchrotron X-ray beams greatly improves the signal-to-noise ratio, allowing the detailed analysis of trace amounts of material and the sufficient data quality for Rietveld refinements. The tunability of the wavelength makes it possible to avoid absorption edges or use hard X-ray radiation in order to penetrate reaction vessels, such as LIB and NIB.<sup>103</sup>

### **3.1.3 X-ray absorption spectroscopy (XAS)**

The element-specific nature and high sensitivity to the local chemical environment of XAS technique make it an ideal tool to detect the electronic structural properties and inter-atomic details. Once the X-rays hit a sample, the oscillating electric field of the electromagnetic radiation interacts with the electrons bound in an atom. Either the radiation will be scattered by these electrons or absorbed and excite the electrons.<sup>104</sup> A narrow parallel monochromatic X-ray beam of intensity  $I_0$  passing through a sample of thickness  $x$  will get a reduced intensity  $I$  according to the equation 3.2:

$$\ln\left(\frac{I_0}{I}\right) = \mu x \quad (\text{eq. 3.2})$$

In this equation,  $\mu$  is the linear absorption coefficient, which depends on the types of elements and the density of the material. At certain energies where the absorption increases drastically and gives rise to an absorption edge. Each edge occurs when the energy of the incident photons is just sufficient to cause excitation of a core electron of the absorbing atom to a continuum state. Thus, the energies of the absorbed radiation at these edges correspond to the binding energies of electrons in the K, L, M, etc, shells of the absorbing elements. The absorption edges are labeled in the order of increasing energy, K, L<sub>I</sub>, L<sub>II</sub>, L<sub>III</sub>, M<sub>I</sub>, corresponding to the excitation of an electron from the 1s (2S<sub>1/2</sub>), 2s (2S<sub>1/2</sub>), 2p (2P<sub>1/2</sub>), 2p (2P<sub>3/2</sub>), 3s (2S<sub>1/2</sub>) orbitals (states), respectively. When the photoelectron leaves the absorbing atom, its wave is backscattered by the neighboring atoms. Figure 3.1 shows the sudden increase in the X-ray absorption with increasing photon energy. The maxima and minima after the edge correspond to the constructive and destructive interference between the outgoing photoelectron wave and backscattered wave. An X-ray absorption spectrum is generally divided into 4 sections: 1) pre-edge ( $E < E_0$ ); 2) X-ray absorption near edge structure (XANES), where the energy of the incident X-ray beam is  $E = E_0 \pm 10$  eV; 3) near edge X-ray absorption fine structure (NEXAFS), in the region between 10 eV up to 50 eV above the edge; and 4) extended X-ray absorption fine structure (EXAFS), which starts approximately from 50 eV and continues up to 1000 eV above the edge.

The minor features in the pre-edge region are usually due to the electron transitions from the core level to the higher unfilled or half-filled orbitals (e.g.,  $s \rightarrow p$ , or  $p \rightarrow d$ ). In the XANES region, transitions of core electrons to non-bound levels with

close energy occur. Because of the high probability of such transition, a sudden raise of absorption is observed. In NEXAFS, the ejected photoelectrons have low kinetic energy ( $E - E_0$  is small) and experience strong multiple scattering by the first and even higher coordinating shells. In the EXAFS region, the photoelectrons have high kinetic energy ( $E - E_0$  is large), and single scattering by the nearest neighboring atoms normally dominates.

## 3.2. First principles calculation

### 3.2.1 Density functional theory

All first principles quantum mechanical calculations require a solution to the many-particle Schrodinger equation. The exact solution of the full many-bodied Schrodinger equation describing a material is still not completely solvable today, but by using a series of approximations, the electronic structure and the total energy of most materials can be calculated quite accurately. The total energy of a compound is defined as “the energy required to bring all constituent electrons and nuclei together from infinite distance” where they do not interact to form an aggregate.<sup>105</sup>

Density Functional Theory (DFT) is an approach to the quantum mechanical many-body problem, which associates all the interactions to a uniform variable, the electronic charge density.<sup>106-108</sup> Hohenberg and Kohn<sup>106</sup> showed that the ground-state energy of an M-electron system is a function only of the electron density  $\rho(\vec{r})$ . In DFT the electrons are represented by one-body wavefunctions, which satisfy Schrodinger-like equations:

$$\left\{ -\nabla^2 + V_N(\vec{r}) + V_e[\rho(\vec{r})] + V_{xc}[\rho(\vec{r})] \right\} \psi_i(\vec{r}) = \epsilon_i \psi_i(\vec{r}) \quad (\text{eq. 3.3})$$

In this equation,  $i$  is the integer number. The first term represents the kinetic energy of a system of non-interacting electrons; the second is the potential due to all nuclei; the third is the classical Coulomb energy, often referred as the Hartree term; and the fourth, the so-called exchange and correlation potential accounts for the Pauli Exclusion Principle and spin effects.  $V_{xc}$  includes the difference between the kinetic energy of a system of independent electrons and the kinetic energy of the actual interacting system with the same density.<sup>105</sup> The solution of the energy equation is obtained in a self-consistent way to ensure the accuracy.

To get the exchange-correlation potential, there are two major approximations to solve this problem, local-density approximation (LDA) and generalized gradient approximation (GGA). In LDA approximation,<sup>109</sup> it is assumed that the exchange-correlation energy per electron equal to the one in a homogeneous electron gas. While in GGA approximation, the detailed deviation of the exchange-correlation potential curve is taken into consideration and used as the criterion to determine the exchange-correlation energy.<sup>110</sup> However, in transition metal ions, the highly localized d electrons could cause the main error of calculation accuracy because of the lack of cancellation of electron self-interaction. A DFT + U method therefore is developed to circumvent this problem and is proved to be successful in intercalation materials.<sup>111, 112</sup>

Besides the electron-electron interaction, the electron-ion interactions are also difficult to deal with because of the huge number of core-electrons of each ion. Since the core-electrons are tightly bonding with the nuclei, a large number of wave functions are needed for the fourier transformation, which will highly raise the cost of computation. It is necessary to do the full electron calculation if dealing with the fine electronic structure

of the materials. However, most of the time, the major physical properties of the materials are determined by the valence electrons.<sup>113</sup> Thus, the pseudopotential approximation is developed so that all the core-electrons are simplified as a core and the ion is divided into two parts - the “core” and the valence electrons. A local pseudopotential is set up that it will be exactly the same with the core electron potential beyond a critical distance,  $r_c$ , from the nuclei. On one hand, the consistence between pseudopotential and full-electron potential beyond  $r_c$  ensures the correction of the properties that determined only by the valence electrons. On the other hand, the complicated core-electrons are substituted by only one potential function therefore the computation cost is significantly reduced. Again, since the pseudopotential of each element is only determined by the atomic number of the element, it could also be determined in a self-consistent way.

### 3.2.2 Applications in battery study

The equilibrium intercalation voltage is determined by the chemical potential difference of alkali ions in the anode and cathode. The open circuit voltage of a cathode with the alkali ion composition of  $x$ , is obtained by

$$V = -\frac{\mu_A^{cathode} - \mu_A^{anode}}{ze} \quad (\text{eq. 3.4})$$

where A is the alkali ion,  $z$  is the charge of alkali ion, and  $e$  is the electron charge. When the anode is pure metallic Li or Na, its chemical potential is constant and the voltage is only dependent on the change in the chemical potential on the cathode. In most cases, the average voltage is of main interest, though it is possible to obtain the voltage as a

function of alkali ion composition with a higher computation cost.<sup>114, 115</sup> The average voltage can be easily obtained by the equation below:

$$V = \frac{-\Delta G}{(x_2 - x_1)ze} \quad (\text{eq. 3.5})$$

where  $\Delta G$  the Gibbs free energy for the reaction between the alkali ion composition of  $x_1$  and  $x_2$  in the cathode. The reaction free energy can be considered in three parts by the equation  $\Delta G \equiv \Delta E + P\Delta V - T\Delta S$ . The internal energy change,  $\Delta E$ , can be obtained from first principles calculations. The  $P\Delta V$  term can be neglected in a solid-state reaction where the volume changes are usually small. In fact,  $P\Delta V$  is in the order of  $10^{-5}$  eV, whereas  $\Delta E$  is in the order of 3 to 4 eV per formula unit.  $T\Delta S$  can also be neglected as it is only the order of thermal energy, which is about 0.025 eV. Therefore,  $\Delta G$  can be approximated by  $\Delta E$  with very small error, enabling the fairly correct voltage prediction from first principles calculation.<sup>114, 115</sup>

During the charging / discharging reaction, some electrode materials experience phase transformations. Irreversible phase transformations cause capacity loss if the transformed structure is not electrochemically active in the desired voltage or rate range. Also, some reversible phase transformations can affect the integrity of structures especially when the volume change involved is substantial. First principles calculations can predict the phase transformation during the alkali ion insertion and extraction, since the energetically favorable phase can be easily determined by total energy calculations.<sup>116</sup> However, predicting phase transformations is often not a simple task if competitive structures are not known at all. All possible candidates for a stable structure at each alkali ion composition should be considered and the total energy of all the structures should be

calculated for comparison. In practice, it is nearly impossible to find all possible structures, and the computational cost of total energy calculations of these structures is often extremely high. Nevertheless, some experimental information available about the structure at certain alkali ion composition can be of great help to reduce the efforts and make phase identification much more efficient. Besides, some techniques which deal with partial disorder efficiently such as the cluster expansion can be useful.<sup>117-119</sup> It has been shown that the cluster expansion technique is particularly helpful in handling candidate structures with partial Li occupancies in Li sites that arise from Li de/intercalation reaction. The dependence of the energy on the site disorder can be parameterized with a cluster expansion if there is no major structural modification. Only the total energy of a manageable number of configurations is required to parameterize the cluster expansion correctly. Once the function between energy and Li composition for candidates structures is constructed, the stable phase(s) at the composition of interest are determined, therefore, the phase transformation can be predicted.<sup>120</sup>

Li diffusivity in electrode materials can be estimated from first principles calculations. Diffusion is a non-equilibrium phenomenon that refers to the transport of atoms over a chemical potential gradient. However, when kinetic phenomena proceed not too far from equilibrium but rather evolve between states that are in local equilibrium.<sup>121-123</sup> the kinetic parameters such as the diffusivity can be determined by considering the decay of fluctuations at equilibrium.<sup>124-133</sup> Li ions spend most of their time at crystallographically well defined equilibrium sites and only a very small fraction of time is spent occupying paths connecting adjacent sites. Therefore, Li motion can be viewed as a succession of discrete hops and be modeled statistically. A good approximation for

the frequency with which Li ions hop between adjacent sites is transition state theory.<sup>120</sup> The transition theory converts the complexity of the many dynamic trajectories a typical atom follows before it actually hops, into a probabilistic frequency that, on average, gives the rate with which an atom performs a hop. In transition state theory, the hop frequency is written by:

$$\Gamma = \nu^* \exp\left(\frac{-\Delta E_b}{k_B T}\right) \quad (\text{eq. 3.6})$$

where  $\nu^*$  is a vibrational prefactor and  $\Delta E_b$  is an energy difference between the initial state and the activated state, that is, an activation barrier. The elastic band method enables the determination of the minimum energy path between two energetically stable endpoints.<sup>134</sup> In the calculation, the initial and final states for a diffusion hop are calculated first. Then a few intermediate states are created by interpolating between initial and final states. As these intermediate states are meta-stable, they are bound to one another with so called “elastic band” so that they do not entirely relax back to their stable initial or final state. The relaxed intermediate states along the energy landscape (first principles energies) follow the minimum energy path and give the activation barrier. All the possible diffusion paths should be calculated and compared, yielding activation barriers for each path. Considering all the paths tested, numerical simulations such as kinetic Monte Carlo enable an explicit simulation of the migration of Li ions using the jump frequency obtained by equation (3.6) with the aid of cluster expansions to parameterize the first principles activation barrier if it depends on the environment.

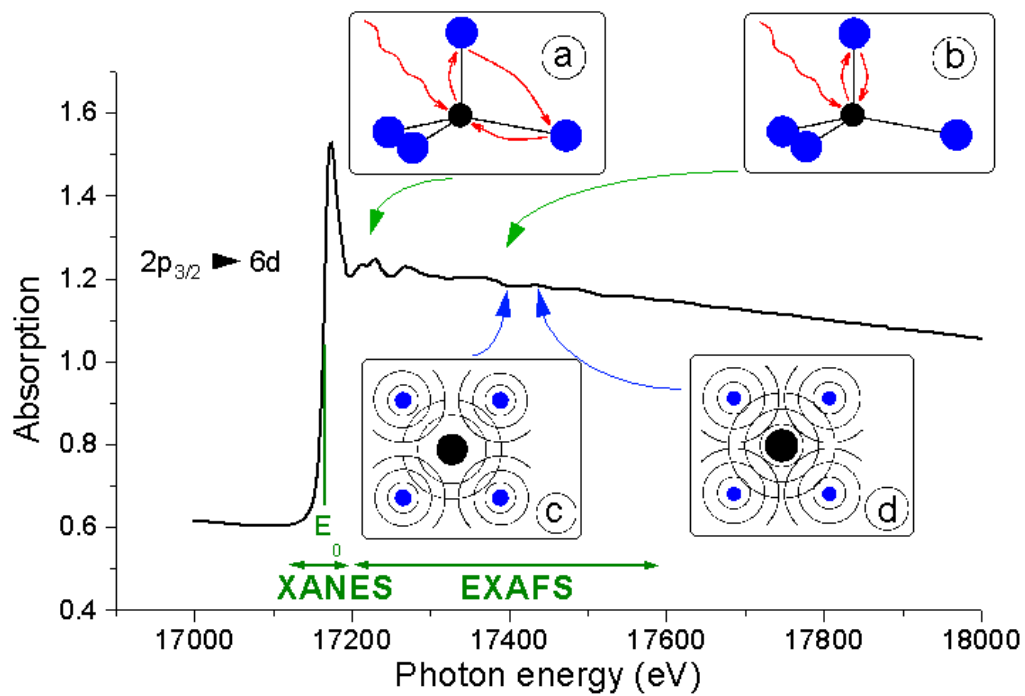


Figure 3.1 X-ray absorption spectroscopy spectra including XANES and EXAFS regions. Inset schemes illustrate the origins of the oscillation in the spectra.

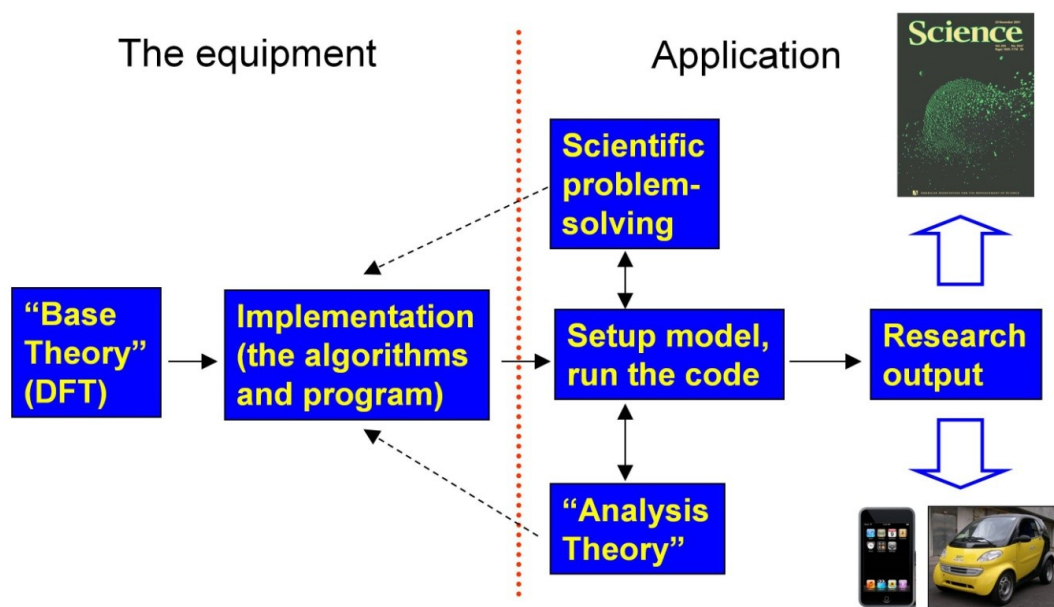


Figure 3.2 Schematic of the application of the DFT calculations in battery research

## **Chapter 4. Advanced cathode for Na-ion batteries with high rate and excellent structural stability**

Li-ion batteries offer the highest energy density among all secondary battery technologies, have dominated the portable electronics market and have been chosen to power the next generation of electric vehicles and plug-in electric vehicles. Nevertheless, the concerns regarding the size of the lithium reserves and the cost associated with Li-ion technology have driven the researchers to search more sustainable alternative energy storage solutions. In this light, sodium-based intercalation compounds have made a major comeback because of the natural abundance of sodium. In this chapter, P2 type cathode,  $\text{Na}_{2/3}[\text{Ni}_{1/3}\text{Mn}_{2/3}]\text{O}_2$ , is intensively investigated to reveal the structural stability and Na-ion mobility using synchrotron X-ray diffraction, electrochemical characterization and computational techniques. The diffusivity of Na-ions in the P2 structure is faster than that of Li-ions in O3 phase. P2 to O2 phase transformation is observed in the high voltage region, however excellent battery properties are obtained by excluding the phase transformation.

### **4.1. Introduction**

The worldwide demand to develop the electrical energy storage is growing as renewable energy technologies such as wind and solar energy conversion become increasingly prevalent. Going forward with large-scale stationary electrical storage, new battery systems which are more reliable and lower in cost will be required<sup>135</sup>. Li-ion batteries have been considered one of the most suitable candidates; however there are

concerns about the cost and the geopolitical limit of lithium sources. In order to develop the alternative energy storage devices, usage of abundant and environmental-friendly elements is needed. Ambient temperature sodium-based batteries have the potential for meeting those requirements due to the wide availability and low cost. In addition, they provide an alternative to Li-ion batteries, since the gravimetric energy density is comparable to Li-ion batteries.

Studies on electrochemical insertion and extraction of Na-ions began in the late 1970s and early 1980s<sup>136-140</sup>. Due to the tremendous success of Li-ion batteries, limited efforts have been spent on Na-ion batteries during the past two decades. More intensive researches on various cathode materials have been conducted since 2000s with the concern regarding the long term viability of Li chemistry. A series of studies on layered cathode materials for Na-ion batteries have been conducted. Sodium-based layered cathode materials are categorized into two major groups which are P2 and O3 type. The first letter “P” or “O” refers to the nature of the site occupied by alkali ion (prismatic or octahedral), and “2” or “3” refers to the number of alkali layers in the repeat unit perpendicular to the layering<sup>21</sup>. The P2 -  $\text{Na}_x\text{CoO}_2$  material has been investigated by Delmas’s group to reveal the phase transformations and electrochemical behaviors<sup>141-144</sup>. Layered O3 type  $\text{Na}_x\text{VO}_2$ <sup>90</sup>,  $\text{Na}_x\text{CrO}_2$ <sup>25</sup>,  $\text{Na}_x\text{MnO}_2$ <sup>26</sup>, and  $\text{Na}_x\text{FeO}_2$ <sup>27</sup> have also been reported to be able to host Na-ions upon charge and discharge, however the capacity fading was significant. A study by Lu et. al demonstrated that the P2 - layered oxide,  $\text{Na}_{2/3}[\text{Ni}_{1/3}\text{Mn}_{2/3}]\text{O}_2$  can reversibly exchange Na-ions in sodium cells<sup>36,37</sup>. In addition to the layered materials, some phosphates based on either the olivine<sup>59, 62, 75, 76</sup> or NASICON<sup>44-46</sup> structures appeared to hold particular promise. Their strong inductive

effect of the  $\text{PO}_4^{3-}$  polyanion that moderates the energetic of the transition metal (TM) redox couple generates relatively high operating potentials in Na-ion batteries. More recently, advanced Na compounds with novel structures have been prepared and characterized. Li substituted  $\text{Na}_{1.0}\text{Li}_{0.2}\text{Ni}_{0.25}\text{Mn}_{0.75}\text{O}_2$  was studied by Kim et. al and displayed 95 mAh/g of specific capacity, excellent cycling and rate capabilities. It is hypothesized that Li in the transition metal layer improves the structural stability during the cycling<sup>39</sup>. The research on single crystal  $\text{Na}_4\text{Mn}_9\text{O}_{18}$  nanowires was conducted by Cao et. al, and they demonstrated that their Na-ion battery exhibited 110mAh/g and good cycling properties until 100 cycles<sup>145</sup>. This compound has drawn significant attention due to the large tunnels in the structure, which are suitable for incorporation of Na-ions<sup>146, 147</sup>. However, they still require the substitution of inactive species or nano-scale fabrication which might diminish the advantage of using low cost sodium. As we mentioned earlier, the reversibility of P2 -  $\text{Na}_{2/3}[\text{Ni}_{1/3}\text{Mn}_{2/3}]\text{O}_2$  has been demonstrated experimentally. However no subsequent studies have been conducted for nearly a decade presumably due to the poor electrochemical performances, though the material is lower in cost and easy to synthesize. Since Na-ion is 70% larger in volume than Li-ion, unique and robust structures are required for long term stability and new intermediate phases due to Na-ion vacancy ordering may be expected during the cycling. Such unique crystal structural phenomena and related electronic properties can be efficiently investigated using first principles computational techniques because of their atomistic level precision<sup>148</sup>. Despite the many advantages, only a few computational studies on the physical or chemical properties of Na-ion batteries have been performed<sup>149, 150</sup>.

In this work, we combine both experimental and computational methods to

investigate the structural, electronic, and electrochemical properties of  $P2 - Na_{2/3}[Ni_{1/3}Mn_{2/3}]O_2$ . The phase transformations upon the charge and discharge were precisely characterized by synchrotron XRD and confirmed by first principles calculations. New intriguing patterns of Na-ions vacancy orderings were identified, which correspond to the intermediate phases during electrochemical cycling. The diffusion barriers calculated by the nudged elastic band (NEB) method and experimentally measured by galvanostatic intermittent titration technique (GITT) demonstrate that the mobility of Na-ions is indeed faster than that of Li-ions in a typical O3 structure. High rate capability and excellent cycling properties can be obtained by limiting the P2-O2 phase transformation.

## 4.2. Experimental

A co-precipitation technique was utilized for the synthesis of the stoichiometric NaOH (Sigma-Aldrich) solution at 10 ml/h rate. The co-precipitated  $M(OH)_2$  were then filtered using a centrifuge and washed three times with deionized water. The dried transition metal precursors were ground with a stoichiometric amount of  $Na_2CO_3$  (anhydrous, 99.5%, Strem chemicals). The calcinations were performed at 500 °C for 5 h and at 900 °C for 14 h in air.

Cathode electrodes were prepared by mixing  $Na_{2/3}[Ni_{1/3}Mn_{2/3}]O_2$  with 10 wt% acetylene black (Strem chemicals) and 5 wt% polytetrafluoroethylene (PTFE). Na metal (Sigma-Aldrich) was used as the counter electrode. 1M  $NaPF_6$  (99%, Strem chemicals) in the battery grade 67 vol.% diethylene carbonate (DEC) and 33 vol.% ethylene carbonate (EC) (Novolyte) were used as the electrolyte and the glass fiber GF/D (Whatman) was

used as the separator. The swagelok type cells were assembled in an argon filled glove box ( $\text{H}_2\text{O} < 0.1$  ppm) and tested on an Arbin battery cycler in the galvanostatic mode. To measure the chemical diffusion coefficient, the galvanostatic intermittent titration technique (GITT) was employed at a pulse of  $17 \mu\text{A}$  ( $C/100$ ) for 1 h and with 2 h relaxation time between each pulse.

The samples for XRD were obtained by disassembling cycled batteries in an argon-filled glovebox. The cathode was washed by battery grade dimethyl carbonate (DMC) 3 times and dried in the vacuum oven at  $100^\circ\text{C}$  for 24 h. The cathode film was sliced into thin pieces and mounted in the hermitically sealed capillary tubes for ex-situ XRD. Powder diffractions of all samples were taken using synchrotron XRD at the Advanced Photon Source (APS) at Argonne National Laboratory (ANL) on beamline 11-BM ( $\lambda = 0.413384 \text{ \AA}$ ). The beamline uses a sagittal focused X-ray beam with a high precision diffractometer circle and perfect Si(111) crystal analyzer detection for high sensitivity and resolution. XRD patterns were analyzed by Rietveld refinement method using FullProf software<sup>151</sup>.

The first principles calculations were performed in the spin-polarized GGA + U approximations to the Density Functional Theory (DFT). Core electron states were represented by the projector augmented-wave method<sup>152</sup> as implemented in the Vienna ab initio simulation package (VASP)<sup>153-155</sup>. The Perdew-Burke-Ernzerhof exchange correlation<sup>156</sup> and a plane wave representation for the wave function with a cutoff energy of 450 eV were used. The Brillouin zone was sampled with a dense k-points mesh by Gamma packing. The supercell is composed of twenty-four formula units of  $\text{Na}_{2/3}[\text{Ni}_{1/3}\text{Mn}_{2/3}]\text{O}_2$ . In the supercell, there are two layers of TM, and two layers of Na-

ions. The in-plane dimension is  $2\sqrt{3}a_{hex} \times 2\sqrt{3}a_{hex}$ . The lattice shows a P 63/m m c layered structure. The atomic positions and cell parameters are fully relaxed to obtain total energy and optimized cell structure. To obtain the accurate electronic structures, a static self-consistent calculation is run, followed by a non-self-consistent calculation using the calculated charge densities from the first step. The cell volume is fixed with internal relaxation of the ions in the second step calculation. The Hubbard U correction was introduced to describe the effect of localized d electrons of transition metal ions. Each transition metal ion has a unique effective U value applied in the rotationally invariant GGA + U approach. The applied effective U value given to Mn ions is 4 eV and to Ni ions is 6.1 eV, consistent with early work<sup>109, 112, 157</sup>. The migration barriers of Na-ion and vacancy in the material are calculated using the NEB method as implemented in VASP.

### 4.3. Results and discussion

#### 4.3.1. Electrochemical properties of P2 – $\text{Na}_{2/3}[\text{Ni}_{1/3}\text{Mn}_{2/3}]\text{O}_2$

Figure 4.1(a) shows the experimental voltage profiles as a function of the specific capacity in the voltage range from 2.3 ~ 4.5 V at a low rate that represents near-equilibrium (C/100). The as-calculated voltage profiles (dotted line) match qualitatively well with the experimental voltage pattern. The theoretical capacity of P2 –  $\text{Na}_{2/3}[\text{Ni}_{1/3}\text{Mn}_{2/3}]\text{O}_2$  is 173 mAh g<sup>-1</sup> considering Ni<sup>2+</sup> - Ni<sup>4+</sup> redox reaction which is associated with 2/3 of Na-ions. However the material exhibits 190 mAh g<sup>-1</sup> of specific capacity at the 1<sup>st</sup> charge which is 17 mAh g<sup>-1</sup> higher than the theoretical value presumably due to possible electrolyte decomposition above 4.4 V. Reversibly, 140 mAh

$\text{g}^{-1}$  of specific capacity was obtained at the following discharge, indicating that the reversibility is around 74%. It was observed that there are two major intermediate phases at 3.5 and 4.0 V upon the charge, which correspond to the Na content of  $1/2$  and  $1/3$ , respectively. A long plateau was observed at 4.22 V indicating that a two phase reaction is occurring. According to the energy calculation shown in Figure 4.1(b), P2 has the lowest energy in the region  $1/3 < x < 2/3$ , thus is the most stable phase. After removing all Na-ions ( $x = 0$ ), O2 is more stable phase whose energy is  $25 \text{ meV f.u.}^{-1}$  (1 f.u. contains one  $[\text{Ni}_{1/3}\text{Mn}_{2/3}]$  unit) lower than P2 phase. This energy difference is significant as the DFT accuracy is about  $3 \text{ meV f.u.}^{-1}$ . The schematics of P2 and O2 structures are shown in Figure. 4.1(c), where Na-ions are coordinated by prismatic site and octahedral site. Therefore the oxygen stacking sequences of P2 and O2 are “AABB” and “ABCB” respectively. It is easy to visualize that O2 structure can be formed by simply gliding of two oxygen layers without breaking the bonds between oxygen and TMs. The coexistence of these two phases leads to the long plateau at 4.22 V in the region  $0 < x < 1/3$ . Using P2 at  $x = 2/3$  and O2 at  $x = 0$  as the reference states, the convex hull connecting all the lowest formation energy (dotted line in Figure 4.1(b)) is constructed, which has been extensively used as a direct measure of phase stability<sup>116, 158</sup>. The two points (dotted circle in Figure 4.1(b)) at  $x = 1/2$  and  $1/3$  shown on the convex hull correspond to two new stable intermediate phases. In order to identify the intermediate phases, synchrotron XRD and advanced calculation are applied.

### **4.3.2. Structural properties of P2 – $\text{Na}_{2/3}[\text{Ni}_{1/3}\text{Mn}_{2/3}]\text{O}_2$ upon the charge and discharge**

As shown in Figure 4.2(a), ex-situ synchrotron XRD was taken at the different Na contents to investigate the new phases and precise sodium intercalation and de-intercalation mechanisms. All the reflections can be indexed in the hexagonal system using the P63/m m c space group except for the fully charged phase. The peaks at  $3.4^\circ$  and  $6.7^\circ$  are associated with the hydrated P2 phase<sup>159</sup>. As reported in earlier work, it was observed that the phase transformation from P2 to O2 occurs above 4.2 V upon the charge, and the P2 phase is reversibly regenerated at the following discharge to 3.75 V. Although the voltage rises were clearly observed at 3.5 V and 4.0 V, no obvious changes are detected in the XRD peak positions and intensities, which are consistent with the earlier report. On the pristine and fully discharged XRD patterns, the small peaks were detected at  $7.23^\circ$ ,  $7.54^\circ$  and  $7.8^\circ$  possibly due to the existence of Na-ion vacancy superstructure ordering (Figure 4.2(a) right), which will be discussed later. In order to obtain precise information regarding the structural changes, Rietveld refinement was carried out to identify the site occupancies and lattice parameters. Detailed Rietveld refinement fitting results of  $\text{Na}_x[\text{Ni}_{1/3}\text{Mn}_{2/3}]\text{O}_2$  are shown in Table 4.1. Changes in lattice parameters are shown in Figure 4.2(b). During Na-ion extraction, the  $a$  lattice parameter, which are dominated by the M–M distance, decreases slightly as expected from the oxidation of Ni ions. The  $a$  lattice parameter is maintained after 1/3 Na-ions are extracted from the structure possibly due to the P2 to O2 phase transformation. However, the  $c$  lattice parameter slowly increases until  $x$  approaches 1/3 and then decreases drastically at the P2 to O2 transformation region; where  $x$  is lower than 1/3. Once the 1/3 of Na-ions are extracted, successive O layers directly face to each other without any screening effect by Na-ions. Therefore, the increased electrostatic repulsion between these oxygen layers

expands the  $c$  lattice parameter along the  $z$ -axis. After  $1/3$  Na-ions are removed from the structure, oxygen layers prefer to shift resulting in O2 stacking. Though the changes in  $c$  lattice is relatively large, P2-O2 transformation requires no bond breaking between oxygen and TM indicating that the required energy is low and the possibility of structural collapse is small. The changes in the lattice parameters appear to be reversible at the following discharge. The changes in the site occupancies of Na-ions during the 1<sup>st</sup> charge and discharge are shown in Figure 4.2(b). There are two different Na sites in the P2 structure, which are face sharing with  $\text{MO}_6$  ( $\text{Na}_f$ ) and edge sharing ( $\text{Na}_e$ ).<sup>35</sup> The total refined Na amount in the as-prepared sample is 0.68, where 0.25 of Na are sitting on  $\text{Na}_f$  site and 0.43 of Na are located in  $\text{Na}_e$  site. In general, the simultaneous occupancy of both sites allows the in-plane  $\text{Na}^+ - \text{Na}^+$  electrostatic repulsion to be minimized leading to globally stable configurations. However, the  $\text{Na}_e$  site is energetically more favorable in comparison with the  $\text{Na}_f$  site due to lower electrostatic repulsion between  $\text{Na}^+$  and  $\text{TM}^+$ . Upon the charge, the Na-ions in  $\text{Na}_e$  site appears to extract slightly faster than Na-ions in the  $\text{Na}_f$  site until  $x$  approaches to  $1/3$ , possibly due to the higher in-plane  $\text{Na}^+ - \text{Na}^+$  electrostatic repulsion in  $\text{Na}_e$  site. However, the occupancies in both sites are uniformly extracted after that concentration. Upon the discharge, Na-ions in both sites are uniformly filled until  $x$  approaches to  $1/3$ , where  $\text{Na}_f = \text{Na}_e = 0.17$ . Although the simultaneous occupancies of both sites are essential to minimize the in-plane electrostatic repulsion, it appears that this repulsion is saturated once around 0.17 Na-ions are filled in each site. After this saturation, the electrostatic repulsion between  $\text{Na}^+$  and  $\text{TM}^+$  energetically governs the occupancies leading to majority Na-ions in  $\text{Na}_e$  site.

### 4.3.3. Na-ion ordering effects

As discussed above, the overall occupancy ratio is decided by the competition between sites energy and electrostatic repulsion. This competition also has effects on the in-plane arrangement of Na-ions. Our calculation reveals that the other two short voltage steps at 3.5 V and 4.0 V mainly result from the in-plane ordering effect. In Figure 4.3(a), the stable ordering patterns in pristine materials consist of  $\text{Na}_f$  connecting in a very intriguing pattern. The distance between such  $\text{Na}_f$  ions is  $2a_{\text{hex}}$ , which has been named “large zigzag” (LZZ) by Meng et. al.<sup>160, 161</sup>. The other simpler ordered states where all Na atoms form “honeycomb”, “diamond” or “row”<sup>119, 162, 163</sup> with no  $\text{Na}_f$  sites occupied, have at least 20 meV f.u.<sup>-1</sup> higher energy compared to that of LZZ. Therefore the ground state ordering has part of Na-ions in high energy sites ( $\text{Na}_f$ ) in order to achieve the stability by minimizing the electrostatic repulsion among Na-ions. In fact, LZZ pattern has also been detected by our synchrotron XRD. As illustrated in Figure 4.3(a) right, three superstructure peaks in pristine electrode are observed, which correspond to the d-spacing of around 3.2 Å. This value is consistent with the average distance between nearest neighbored Na-ions in the proposed LZZ pattern. Superstructure peaks disappear as Na-ions are extracted and the concentration deviates from 2/3, however they are recovered in the fully discharged electrode, suggesting that such Na-ions vacancy ordering is preferred at  $x = 2/3$  concentration. Though there is a possibility that the TM charge ordering could exist, but XRD cannot probe the charge ordering as the TM-ions have similar scattering intensities. Therefore, the superstructure observed is surely from Na-ions vacancy ordering. At  $x = 1/2$  (Figure 4.3(b)), the ordering is changed from LZZ to rows, where one row of  $\text{Na}_f$  and two rows of  $\text{Na}_e$  arrange in the plane alternatively.

When the concentration is reduced to 1/3, Na orders in rows on either  $\text{Na}_e$  or  $\text{Na}_f$  sites in a single layer. However, the stacking faults along the  $c$ -axis caused by P2 to O2 oxygen framework shift prevent us from finding peaks related to superstructures by the power diffraction.<sup>164</sup> A more detailed study to shed light on the evolution of these superstructures upon cycling is currently underway. This is the first time that Na-ion ordering effects are reported and discussed in  $\text{Na}_x[\text{Ni}_{1/2}\text{Mn}_{2/3}]\text{O}_2$ , though a lot of work has been done on  $\text{Na}_x\text{CoO}_2$ , a thermoelectric oxide material<sup>160, 161</sup>. Based on our calculation, this ordering preference is essential during the electrochemical cycling and common for all Na compounds.

#### 4.3.4. Diffusion properties of Na-ion in P2 – $\text{Na}_{2/3}[\text{Ni}_{1/3}\text{Mn}_{2/3}]\text{O}_2$

Noticing that Na-ions prefer different in-plane ordering at different Na concentration, it is hypothesized that such a fast self-arrangement must require high Na-ions mobility in the material. A NEB calculation is applied to further study the activation barrier in the  $\text{Na}_x[\text{Ni}_{1/2}\text{Mn}_{2/3}]\text{O}_2$ . The Na-ions diffusion paths of P2 (left) and O2 (right) are shown in Figure 4.4(a). The path with the minimum energy in P2 structure is passing through a shared face between two neighbored Na prismatic sites. For O2 structure, the Na-ions have to cross the tetrahedron between two octahedral sites by means of a divacancy mechanism<sup>165</sup>. According to Figure 4.4(b), Na-ions need only around 170 meV to be activated in the diffusion process, when the concentration range is  $1/3 < x < 2/3$ ; this activation barrier is lower than half of its corresponding O3 – Li compounds<sup>166</sup>. In the P2-O2 phase transformation region, the required energy increases to over 290 meV, indicating a low hopping rate and slow Na-ion mobility. This big energy difference

results from the distinct diffusion paths. It is evident that in P2 structure, the diffusion path of Na-ions is more spacious than that in O2 structure leading to much lower activation barrier. Once most of Na-ions are removed, the energy barrier decreases back to 250 meV due to the relatively small repulsion from neighboring ions in the dilute concentration. In addition to the NEB calculation, GITT was performed to measure the Na-ions mobility as a function of Na concentration in  $\text{Na}_x[\text{Ni}_{1/3}\text{Mn}_{2/3}]\text{O}_2$ , since it is known to be more reliable to calculate the chemical diffusion coefficient, especially when intrinsic kinetics of phase transformations are involved.<sup>167</sup> Figure 4.4(c) shows the variation of chemical diffusion coefficient of Na-ions ( $D_{\text{Na}}$ ) in  $\text{Na}_x[\text{Ni}_{1/3}\text{Mn}_{2/3}]\text{O}_2$  determined from the GITT profiles. The minimum value of  $D_{\text{Na}}$  is observed in  $0 < x < 1/3$ , where P2 to O2 phase transformation occurs. However, the  $D_{\text{Na}}$  in the solid solution region ( $1/3 < x < 2/3$ ) exhibits  $7 \times 10^{-9} \sim 1 \times 10^{-10} \text{ cm}^2 \text{ sec}^{-1}$ , which is around 1 order of magnitude higher than corresponding Li diffusivity in O3 compounds, where  $D_{\text{Li}}$  is  $3 \times 10^{-9} \sim 2 \times 10^{-11} \text{ cm}^2 \text{ sec}^{-1}$ <sup>168</sup>. Both NEB calculation and GITT demonstrated that Na-ions diffusion in P2 -  $\text{Na}_{2/3}[\text{Ni}_{1/3}\text{Mn}_{2/3}]\text{O}_2$  is fast.

#### 4.3.5. Electronic structural properties

To obtain the information on the oxidation states of TM, the density of states (DOS) of Ni and Mn  $3d$  orbitals in  $\text{Na}_x[\text{Ni}_{1/2}\text{Mn}_{2/3}]\text{O}_2$  ( $x = 2/3, 1/3, 0$ ) are calculated and presented in Figure 4.5. Since the Ni and Mn ions sit in the octahedral site surrounded by 6 oxygen ions,  $3d$  bands of TM ions split into  $t_{2g}$  and  $e_g$  bands. In the Ni DOS for pristine materials ( $x = 2/3$ , black curve in Figure 4.5 (a)), the energy levels of both spin-up and spin-down states in the  $t_{2g}$  orbitals are lower than the Fermi energy, indicating that the  $t_{2g}$

orbitals are fully occupied. Similarly, the spin-down states of the  $e_g$  orbitals are also full of electrons, since their energy levels are below the Fermi level. However, the energy levels of spin-up states in the  $e_g$  orbitals are above the Fermi level, indicating no orbitals are occupied. This electron configuration,  $t_{2g}^6 e_g^2$ , by Ni DOS demonstrates the presence of  $Ni^{2+}$  in the pristine material. In the half de-intercalated state ( $x = 1/3$ , red curve in Figure 4.5 (b)), the Ni DOS suggests that the  $t_{2g}$  orbitals are still completely occupied. However the spin-down states of  $e_g$  orbitals are separated into two peaks, where one peak has lower energy than the Fermi level. This indicates that one of the spin-down  $e_g$  orbitals is occupied leading to the  $t_{2g}^6 e_g^1$  electron configuration, so the existence of  $Ni^{3+}$  is confirmed at  $x = 1/3$ . After removing all Na-ions ( $x = 0$ , blue curve in Figure 4.5 (c)), most of the electrons in the  $e_g$  orbitals are removed as the energy levels of  $e_g$  orbitals are higher than the Fermi level. However, the DOS suggested that certain amount of the electron density is still found in  $e_g$  orbitals. Based on our calculation, Ni-ions are oxidized to +3.5 at the end of the charge. On the other hand, Mn-ions remain predominately at tetravalent with fully occupied  $t_{2g}$  orbitals and completely empty  $e_g$  orbitals, independent of the changes in Na concentrations (green curve in Figure 4.5 (a), (b), and (c)). In summary, our calculation illustrates the evolution of electronic structures in TM; when Na-ions are gradually extracted, Ni-ions undergo the transition of  $Ni^{2+} - Ni^{3+} - Ni^{3.5+}$ , while Mn-ions stay at +4 valence state upon the whole cycling maintaining the structural stability in the absence of Jahn-Teller active  $Mn^{3+}$ .

In addition to the changes in transition metal states, our calculation also suggests that O-ions are involved in the redox reaction providing additional electrons at the end of charging process to keep the charge balance in the compound (Figure 4.6). The valence

of O-ions is investigated qualitatively from the changes of spin distribution on O layer. In Fig. 5.6 (a), part of the O layers of  $\text{Na}_x[\text{Ni}_{1/3}\text{Mn}_{2/3}]\text{O}_2$  supercell is represented by the red balls along with the adjacent TM slab. The corresponding spin densities in the pristine and fully charged materials are shown in Figure 4.6 (b) and (c), respectively. Though the plane is cut through O layer, the spin density of Ni and Mn-ions can still be observed partially. In the pristine material ( $x = 2/3$ , Figure 4.6 (b)), well bonded O 2p electrons can be clearly observed, however, the shape of O 2p electron clouds change significantly in fully charged phase ( $x=0$ ), suggesting the obvious changes in O valence. Compared with the dramatic changes around O, the electron densities of Mn-ions are slightly increased due to the charge re-hybridization around O. The above results demonstrate that the extra electrons, which cannot be provided by Ni redox couples, come from O-ions during the charging stage. Similar phenomena have also been proposed in some Li compounds<sup>169, 170</sup>. Such phenomena are likely to attribute the low rate and poor cycling capability at extremely low Na concentration. Detailed study to reveal the evolution of atomic and electronic structures of the TM upon cycling by in-situ XAS is currently in progress.

#### **4.3.6. Improved electrochemical properties of P2 – $\text{Na}_{2/3}[\text{Ni}_{1/3}\text{Mn}_{2/3}]\text{O}_2$**

The electrochemical properties of P2 -  $\text{Na}_{2/3}[\text{Ni}_{1/3}\text{Mn}_{2/3}]\text{O}_2$  are shown in Figure 4.7. Cycling tests were carried out using different cut-off voltages (4.5 V and 4.1 V), as well as different C-rates, C/100, C/20 and C/5. The cycling performances are significantly affected by the P2-O2 phase transformation above 4.2 V. As shown in Figure 4.7 (a), the voltage cut-off at 4.1 V prevents the P2-O2 phase transformation avoiding the dramatic changes in oxygen framework of the host structure. The 1<sup>st</sup>

discharge capacity was  $134 \text{ mAh g}^{-1}$  if the cut-off voltage is 4.5V, however the capacity retention at the 2<sup>nd</sup> discharge was 89%, and only 64% of capacity can be obtained after 10 cycles. However, the cycling excluding the phase transformation region shows excellent capacity retentions at both C/20 and C/5. The capacity at the 1<sup>st</sup> discharge was  $87.8 \text{ mAh g}^{-1}$  at C/20, which is corresponding to the insertion of 1/3 Na-ions. 94.9% of capacity can be retained after the 50<sup>th</sup> cycle at the average voltage of 3.4 V vs.  $\text{Na}^+/\text{Na}$ . In C/5 cycling, the 1<sup>st</sup> discharge capacity was  $81.85 \text{ mAh g}^{-1}$ , corresponding to 93% of capacity obtained at C/20. The capacity retention after the 50<sup>th</sup> cycle was 92% and the coulombic efficiency reached higher than 96% during the 50 cycles. Since no battery grade Na metal is commercially available, our Na anode contains a certain amount of impurities. Nonetheless, the cathode still shows excellent capacity retentions during the cycling. The rate capability is also significantly improved when excluding the phase transformation region (Figure 4.7 (b)). The electrode delivered  $89.0 \text{ mAh g}^{-1}$  at C/20,  $83.3 \text{ mAh g}^{-1}$  at C/2,  $75.7 \text{ mAh g}^{-1}$  at 1C, corresponding to 85% of capacity at C/20 and  $62.4 \text{ mAh g}^{-1}$  at 2C, 70% of capacity at C/20. Based on the electrochemical performances, it has been demonstrated that the  $\text{P2} - \text{Na}_{2/3}[\text{Ni}_{1/3}\text{Mn}_{2/3}]\text{O}_2$  material in Na-ion batteries exhibits excellent cycling stability and rate capability which are comparable to Li-ion batteries. Improvement on capacity beyond  $100 \text{ mAh g}^{-1}$  in P2 structure is possible with different transition metals ratio and alkali metal substitution.

#### 4.4. Conclusions

In summary, ambient temperature Na-ion batteries have the potential to meet the requirements for large-scale stationary energy storage sources as well as an alternative to

Li-ion batteries due to the natural abundance and low cost of sodium. We prepared P2 -  $\text{Na}_{2/3}[\text{Ni}_{1/3}\text{Mn}_{2/3}]\text{O}_2$  with excellent cycling property and high rate capability as a cathode material for Na-ion batteries. The phase transformation from P2 to O2 at 4.22 V was investigated by first principles formation energy calculation and confirmed by synchrotron XRD. The specific Na-ions orderings were found at  $\text{Na} = 1/3$  and  $1/2$ , which are corresponding to the voltage steps in the charging profile. Based on both GITT measurement and NEB calculation, the diffusivity of Na-ions in P2 structure is indeed higher than that in the corresponding O3 structured Li compounds. The electronic structures have been studied and DOS calculation suggested that oxygen partially participates the redox reaction at the end of the electrochemical charge. Consequently, it was demonstrated that the capacity retention of 95% after 50 cycles could be obtained by excluding the P2–O2 phase transformation and 85% of the reversible capacity could be retained at a 1C rate. In addition, a simple synthesis method can be used to prepare this material without any special nano-scale fabrication. Our study demonstrate that P2 -  $\text{Na}_{2/3}[\text{Ni}_{1/3}\text{Mn}_{2/3}]\text{O}_2$  is a strong candidate for cathode in Na-ion batteries for large-scale energy storage.

Chapter 4, in full, is a reprint of the material “Advanced cathode for Na-ion batteries with high rate and excellent structural stability” as it appears in the Physical chemistry chemical physics, Dae Hoe Lee, Jing Xu, Ying S. Meng, Physical chemistry chemical physics 2013, 15, 3304. The dissertation author was the co-primary investigator and author of this paper. All computational parts were performed by the author except for the experiment parts.

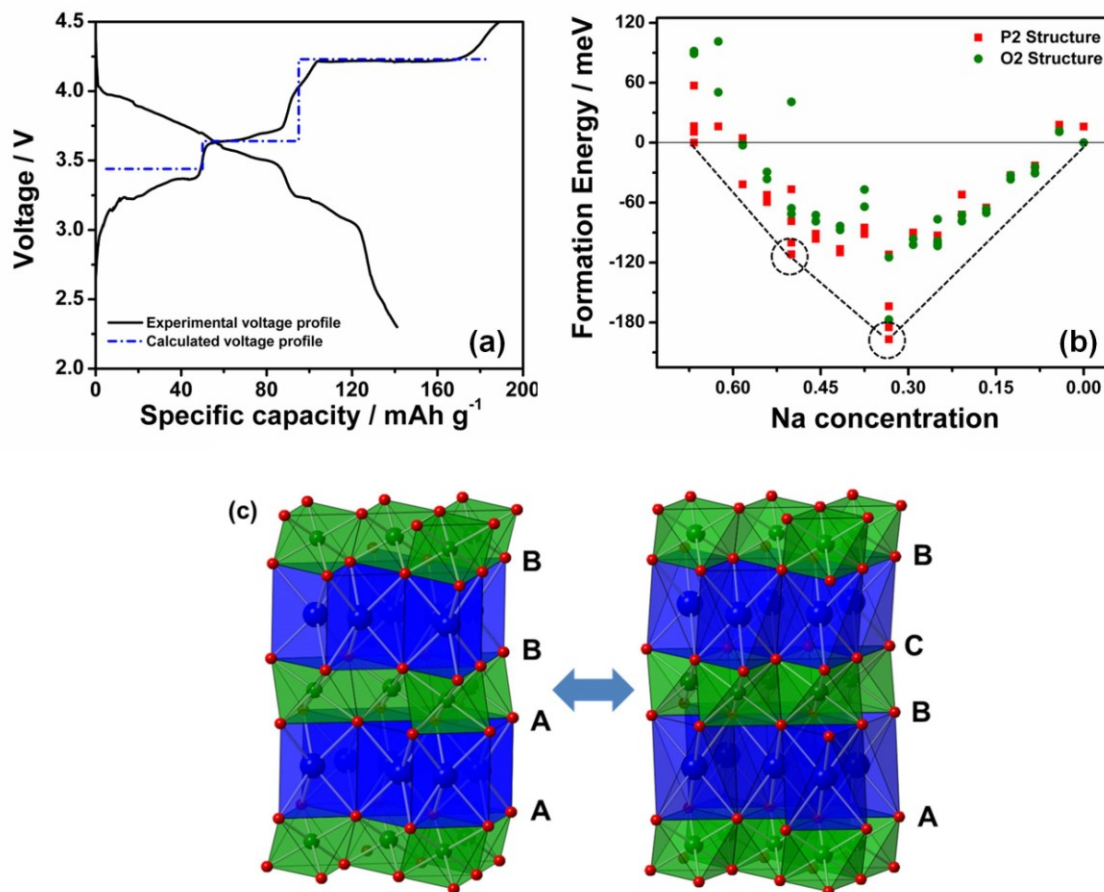
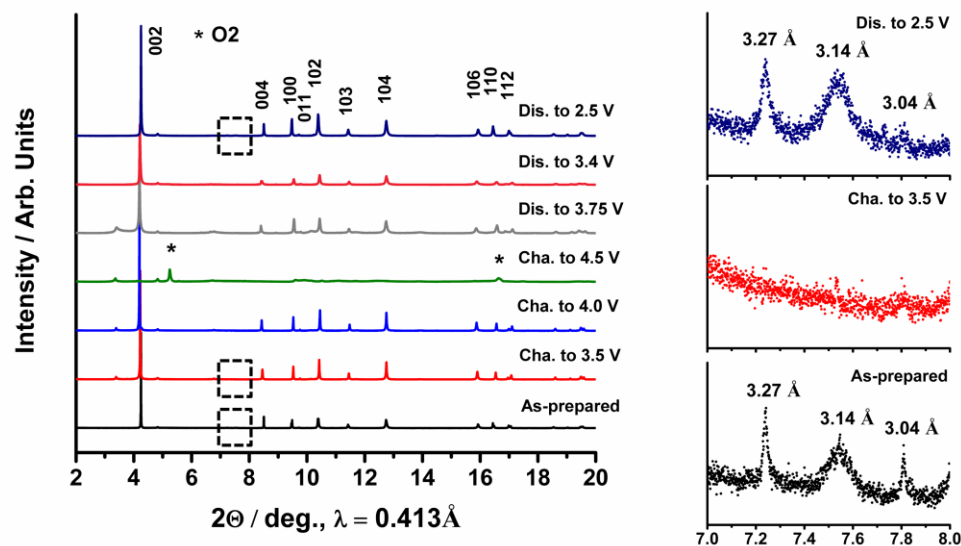
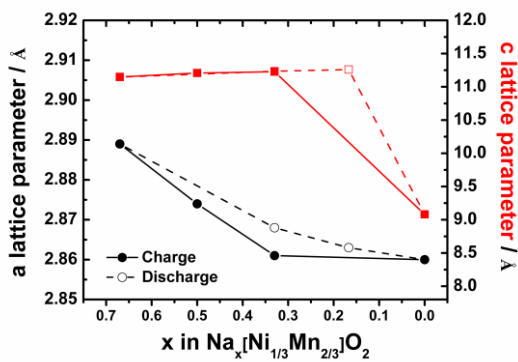


Figure 4.1 (a) Electrochemical profiles for Na/Na<sub>2/3</sub>[Ni<sub>1/3</sub>Mn<sub>2/3</sub>]O<sub>2</sub> cells between 2.3 to 4.5 V at C/100 current rate including the calculated voltage profiles (dotted line), (b) Calculated formation energies at different Na concentration including the convex hull (dotted line), and (c) Structural schematics of P2 and O2 including the stacking sequence of oxygen layers, Continued

(a)



(b)



(c)

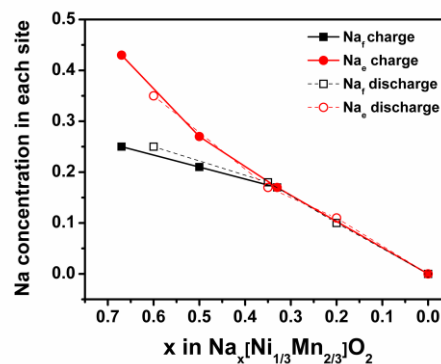


Figure 4.2 (a) Synchrotron X-ray diffraction patterns of  $\text{Na}_x[\text{Ni}_{1/3}\text{Mn}_{2/3}]\text{O}_2$  at different  $x$  concentration during the 1st cycle and (right) enlarged XRD patterns of pristine, charged to 3.5 V and fully discharged electrodes between  $7^\circ$  to  $8^\circ$  including d-spacing, (b) Changes in a and c lattice parameters, and (c) Changes in  $\text{Na}_f$  and  $\text{Na}_e$  site occupancies upon the 1st cycle

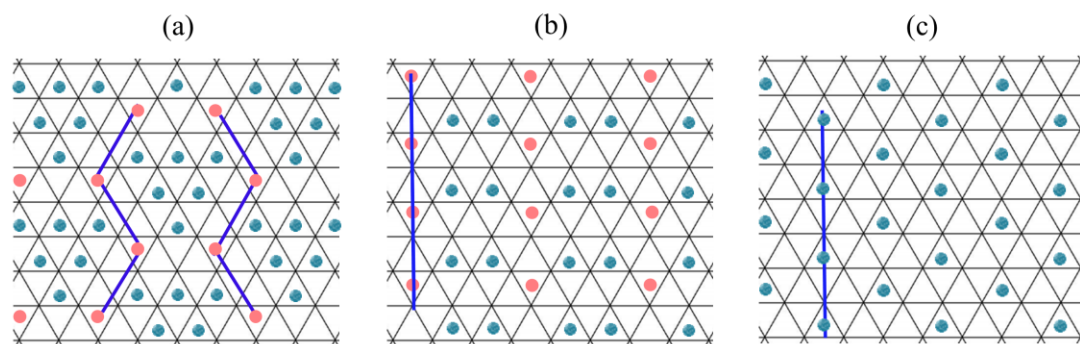


Figure 4.3 In-plane Na-ions orderings of  $\text{Na}_x[\text{Ni}_{1/3}\text{Mn}_{2/3}]\text{O}_2$  in the triangular lattice (a)  $x = 2/3$ , (b)  $x = 1/2$ , and (c)  $x = 1/3$  (Blue balls: Na-ions on  $\text{Na}_e$  sites, pink balls: Na-ions on  $\text{Na}_f$  sites)

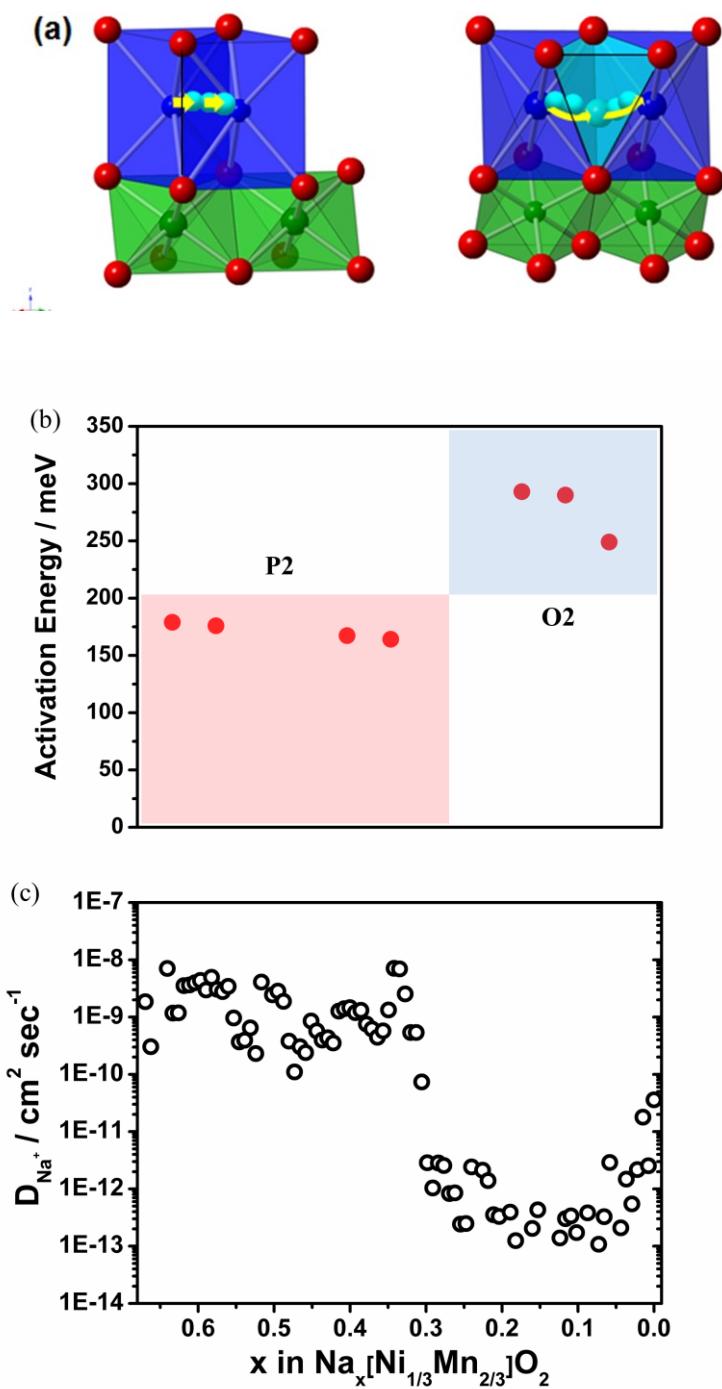


Figure 4.4 (a) The diffusion paths of P2 (left) and O2 (right), (b) Calculated activation energy using NEB method, and (c) Chemical diffusion coefficient of Na-ions ( $D_{Na}$ ) in  $Na_x[Ni_{1/3}Mn_{2/3}]O_2$  calculated from GITT as a function of the Na concentration.

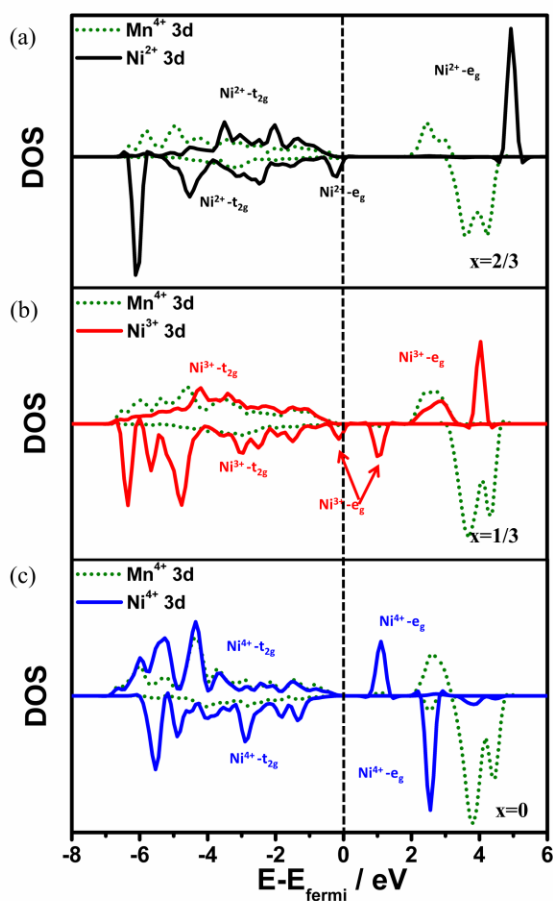


Figure 4.5 The electronic structures of Ni 3d and Mn 3d orbitals in  $\text{Na}_x[\text{Ni}_{1/3}\text{Mn}_{2/3}]\text{O}_2$  at (a)  $x = 2/3$ , (b)  $x = 1/3$ , and (c)  $x = 0$

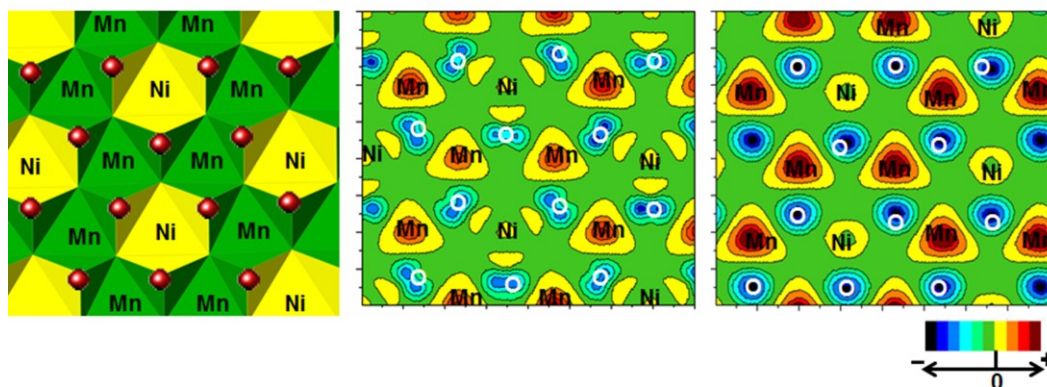
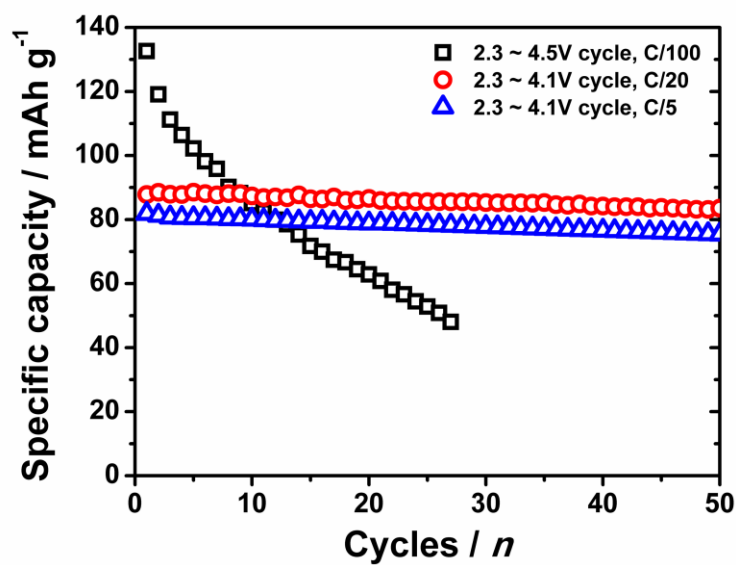


Figure 4.6 (a) Schematic illustration of the oxygen layer, (b) Calculated spin density cutting from oxygen layer at  $x = 2/3$ , and (c)  $x = 0$

(a)



(b)

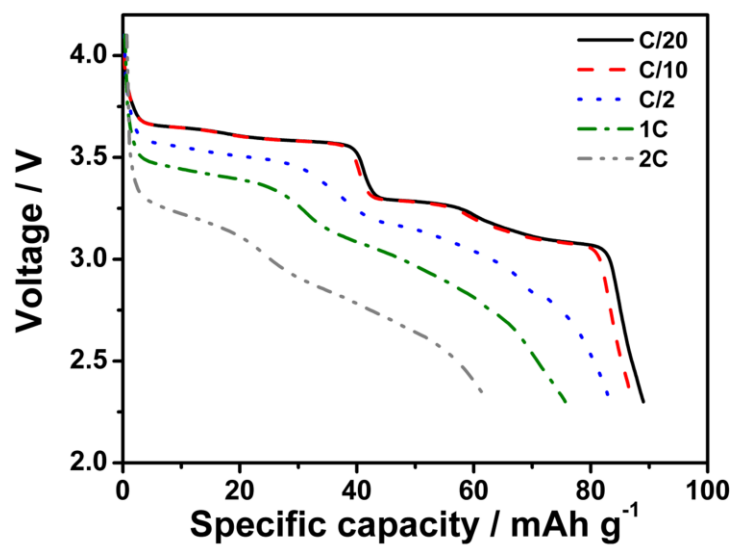


Figure 4.7 The electrochemical properties of Na/Na<sub>2/3</sub>[Ni<sub>1/3</sub>Mn<sub>2/3</sub>]O<sub>2</sub> cells, (a) Cycling performances at different voltage ranges (2.3 ~ 4.1 V and 2.3 ~ 4.5 V) and different C-rate (C/100, C/20 and C/5), and (b) Rate capability at C/20, C/10, C/2, 1C and 2C between 2.3 ~ 4.1 V

Table 4.1 Rietveld refinement results (lattice parameters, Na sites, and R-factors)

Pristine $\text{Na}_{2/3}[\text{Ni}_{1/3}\text{Mn}_{2/3}]\text{O}_2$ Space group: P 63/m m c						Charged to 3.5 V $\text{Na}_{1/2}[\text{Ni}_{1/3}\text{Mn}_{2/3}]\text{O}_2$ Space group: P 63/m m c					
Atom	Site	x	y	Z	Occ.	Atom	Site	x	y	z	Occ.
Ni	2a	0	0	0	1/3	Ni	2a	0	0	0	1/3
Mn	2a	0	0	0	2/3	Mn	2a	0	0	0	2/3
Na <sub>f</sub>	2b	0	0	0.25	0.25	Na <sub>f</sub>	2b	0	0	0.25	0.21
Na <sub>e</sub>	2d	2/3	1/3	0.25	0.43	Na <sub>e</sub>	2d	2/3	1/3	0.25	0.27
O	4f	1/3	2/3	0.08	2	O	4f	1/3	2/3	0.08	2
a = b = 2.889 Å, c = 11.149 Å						a = b = 2.874 Å, c = 11.208 Å					
R <sub>wp</sub> = 0.73%, R <sub>B</sub> = 4.42%						R <sub>wp</sub> = 0.57%, R <sub>B</sub> = 6.24%					
Charged to 4.0 V P2 - $\text{Na}_{1/3}[\text{Ni}_{1/3}\text{Mn}_{2/3}]\text{O}_2$ Space group: P 63/m m c						Charged to 4.5 V $\text{Na}_0[\text{Ni}_{1/3}\text{Mn}_{2/3}]\text{O}_2$ Space group: P 63 m c					
Atom	Site	x	y	Z	Occ.	Atom	Site	x	y	z	Occ.
Ni	2a	0	0	0	1/3						
Mn	2a	0	0	0	2/3						
Na <sub>f</sub>	2b	0	0	0.25	0.17						
Na <sub>e</sub>	2d	2/3	1/3	0.25	0.17						
O	4f	1/3	2/3	0.08	2						
a = b = 2.861 Å, c = 11.227 Å						a = b = 2.860 Å, c = 9.081 Å					
R <sub>wp</sub> = 1.11%, R <sub>B</sub> = 5.75%						R <sub>wp</sub> = 0.64%, R <sub>B</sub> = 0.29%					

Table 4.1 Rietveld refinement results (lattice parameters, Na sites, and R-factors),  
Continued

Discharged to 3.75 V $\text{Na}_{1/6}[\text{Ni}_{1/3}\text{Mn}_{2/3}]\text{O}_2$ Space group: P 63/m m c						Discharged to 3.4 V $\text{Na}_{1/3}[\text{Ni}_{1/3}\text{Mn}_{2/3}]\text{O}_2$ Space group: P 63/m m c					
Atom	Site	x	y	Z	Occ.	Atom	Site	x	y	z	Occ.
Ni	2a	0	0	0	1/3	Ni	2a	0	0	0	1/3
Mn	2a	0	0	0	2/3	Mn	2a	0	0	0	2/3
Na <sub>f</sub>	2b	0	0	0.25	0.10	Na <sub>f</sub>	2b	0	0	0.25	0.18
Na <sub>e</sub>	2d	2/3	1/3	0.25	0.11	Na <sub>e</sub>	2d	2/3	1/3	0.25	0.17
O	4f	1/3	2/3	0.08	2	O	4f	1/3	2/3	0.08	2
$a = b = 2.863 \text{ \AA}, c = 11.260 \text{ \AA}$						$a = b = 2.868 \text{ \AA}, c = 11.235 \text{ \AA}$					
$R_{\text{wp}} = 1.34\%, R_{\text{B}} = 10.33\%$						$R_{\text{wp}} = 0.76\%, R_{\text{B}} = 7.98\%$					
Discharged to 2.5 V $\text{Na}_{1/2}[\text{Ni}_{1/3}\text{Mn}_{2/3}]\text{O}_2$ Space group: P 63/m m c											
Atom	Site	X	y	Z	Occ.						
Ni	2a	0	0	0	1/3						
Mn	2a	0	0	0	2/3						
Na <sub>f</sub>	2b	0	0	0.25	0.25						
Na <sub>e</sub>	2d	2/3	1/3	0.25	0.35						
O	4f	1/3	2/3	0.08	2						
$a = b = 2.889 \text{ \AA}, c = 11.147 \text{ \AA}$											
$R_{\text{wp}} = 1.14\%, R_{\text{B}} = 6.69\%$											

## Chapter 5. Identifying the Critical Role of Li Substitution in

### P2–Na<sub>x</sub>[Li<sub>y</sub>Ni<sub>z</sub>Mn<sub>1-y-z</sub>]O<sub>2</sub> (0 < x, y, z < 1) Intercalation Cathode Materials for High Energy Na-ion Batteries

Li substituted layered P2–Na<sub>0.80</sub>[Li<sub>0.12</sub>Ni<sub>0.22</sub>Mn<sub>0.66</sub>]O<sub>2</sub> is investigated as an advanced cathode material for Na-ion batteries. Both neutron diffraction and nuclear magnetic resonance (NMR) spectroscopy are used to elucidate the local structure and they reveal that most of the Li ions are located in transition metal (TM) sites, preferably surrounded by Mn ions. In order to characterize structural changes occurring upon electrochemical cycling, *in situ* synchrotron X-ray diffraction is conducted. It is clearly demonstrated that no significant phase transformation is observed up to 4.4 V charge for this material, unlike Li-free P2 type Na cathodes. The presence of monovalent Li ions in the TM layers allows more Na ions to reside in the prismatic sites, stabilizing the overall charge balance of the compound. Consequently, more Na ions remain in the compound upon charge, the P2 structure is retained in the high voltage region and the phase transformation is delayed. *Ex situ* NMR is conducted on samples at different states of charge / discharge to track Li-ion site occupation changes. Surprisingly, Li is found to be mobile - some Li ions migrate from the TM layer to the Na layer at high voltage - yet this process is highly reversible. Novel design principles for Na cathode materials are proposed on the basis of an atomistic level understanding of the underlying electrochemical processes. These principles enable us to devise an optimized, high capacity, and structurally stable compound as a potential cathode material for high-energy Na-ion batteries.

## 5.1. Introduction

The pressing demands for economically accessible and environmentally benign energy storage technologies in large-scale applications are strong drivers for fundamental research in novel materials discovery. Though Li-ion batteries offer the highest energy density among all secondary battery chemistries, concerns regarding lithium availability and its rising cost have driven researchers to investigate sustainable energy-storage alternatives.<sup>135</sup> In this light, Na-ion battery systems have made a major comeback because of the natural abundance and wide distribution of Na resources. Although Li and Na ions share many common features, such as similar valence states and outer shell configurations, the various Na compounds used in batteries have demonstrated unique characteristics resulting in different electrochemical performances. For example, layered  $\text{LiCrO}_2$  is electrochemically inactive towards Li-ion extraction, however,  $\text{NaCrO}_2$  can work reversibly as a cathode in rechargeable Na-ion batteries.<sup>28, 29</sup> Moreover, the Ti(IV)/Ti(III) redox couple in  $\text{Na}_2\text{Ti}_3\text{O}_7$  has shown a surprisingly low average voltage (0.3V) in Na-ion batteries, which has never been observed in any  $\text{Li}_x\text{Ti}_y\text{O}_z$ -type compound ( $x, y, z > 0$ ).<sup>171, 172</sup> Therefore, in-depth insight into the Na-ion electrochemistry is essential as Na-ion intercalation processes exhibit many features in stark contrast to Li-ion electrochemistry.

Among most of the Na cathode compounds reported to date, Na layered oxides with a P2 structure ( $\text{Na}_x\text{TMO}_2$ , TM = Transition Metal) have drawn significant attention. Their layered structures are able to accommodate large Na-ions and provide spacious diffusion paths as well as structural stability. Research on the structural properties of  $\text{Na}_x\text{TMO}_2$  started in the 70's with Delmas et al.,<sup>21, 23</sup> who, by studying  $\text{Na}_x\text{CoO}_2$ ,

demonstrated that  $\text{Na}_x\text{TMO}_2$  compounds can be used as cathode materials.<sup>24</sup> However, limited efforts have been devoted to Na-ion batteries over the past two decades due to the tremendous success of Li-ion batteries. Recently, various P2- $\text{Na}_x\text{TMO}_2$  and their binary or ternary derivatives, have been extensively investigated and some of them have demonstrated superior electrochemical performances.<sup>98</sup> Berthelot et al. have reinvestigated P2- $\text{Na}_x\text{CoO}_2$  and demonstrated reversible battery performance between  $0.45 \leq x \leq 0.90$ .<sup>33</sup> It has been shown that P2- $\text{Na}_{2/3}[\text{Ni}_{1/3}\text{Mn}_{2/3}]\text{O}_2$  used as cathode in Na cells reversibly exchanges all of the Na ions, leading to a capacity of  $160 \text{ mAh g}^{-1}$  between 2.0 - 4.5 V.<sup>36, 173</sup> Very recently, Yabuuchi et al. reported that  $\text{Na}_{2/3}[\text{Fe}_{1/2}\text{Mn}_{1/2}]\text{O}_2$  delivers an exceptional initial capacity of  $190 \text{ mAh g}^{-1}$  between 1.5 ~ 4.2 V.<sup>40</sup> However, all of these materials undergo at least one or more phase transformations leading to several voltage steps in their electrochemical profiles. These transformations represent major practical issues for Na-ion batteries since they greatly shorten cycle life and reduce rate capabilities. To address this issue, the Li substituted P2 compound  $\text{Na}_{1.0}\text{Li}_{0.2}\text{Ni}_{0.25}\text{Mn}_{0.75}\text{O}_2$  was proposed by Kim et al. and displayed a single smooth voltage profile suggesting a solid-solution intercalation reaction.<sup>174</sup> This material delivered 95 - 100  $\text{mAh g}^{-1}$  of specific capacity in the voltage range of 2.0 - 4.2 V, and demonstrated excellent cycling and rate capabilities. In spite of these encouraging improvements, it is still unclear how phase transformations can be prevented and what the critical role of Li is in maintaining the P2 structure.

A comprehensive study on P2- $\text{Na}_x[\text{Li}_y\text{Ni}_z\text{Mn}_{1-y-z}]\text{O}_2$  ( $0 < x, y, z < 1$ ) materials is reported in this work. Single smooth voltage profiles are obtained in the voltage range of 2.0 ~ 4.4 V along with excellent rate and cycling performances. The crystal structure,

including the superlattice formed by partial ordering of the Li, Ni, and Mn ions is characterized using both X-ray powder diffraction (XRD) and neutron powder diffraction. Since Ni and Mn have similar electron densities, the superlattice formed by ordering of Ni and Mn atoms is difficult to be observed by X-ray measurements. Neutron diffraction, however, can distinguish between these elements since the scattering lengths of their most abundant natural isotopes are comparatively different: Ni = 10.3 fm, and Mn = -3.73 fm. While long-range structural information is available from diffraction methods, magic angle spinning (MAS) solid-state NMR provides detailed insight into the local environments experienced by both active and electrochemically inactive ions in the cathode, and can be applied to highly disordered systems. NMR characterisation of the  $^7\text{Li}$  local environments present in the pristine P2- $\text{Na}_{0.8}[\text{Li}_{0.12}\text{Ni}_{0.22}\text{Mn}_{0.66}]\text{O}_2$  phase and at different stages along the first electrochemical cycle enables us to determine both the electrochemical role of Li in the electrode and the importance of Li substitution in P2 phase stabilisation. The structural evolution of the electrode upon charge is tracked by *in situ* synchrotron XRD (SXRD). X-ray absorption spectroscopy (XAS) is performed to study charge compensation mechanisms. The critical role of Li substitution in phase stabilization is discussed, and novel design principles for this type of P2 materials are presented.

## 5.2. Experimental

The compounds were synthesized using a co-precipitation technique. TM nitrates,  $\text{Ni}(\text{NO}_3)_2 \cdot 6\text{H}_2\text{O}$  (99%, Acros Organics) and  $\text{Mn}(\text{NO}_3)_2 \cdot 4\text{H}_2\text{O}$  (98%, Acros Organics), were titrated into a stoichiometric NaOH (Sigma-Aldrich) solution at a rate of  $10 \text{ ml h}^{-1}$ .

Co-precipitated  $\text{TM}(\text{OH})_2$  was then filtered using a centrifuge, washed three times with deionized water and then dried at 150 °C for 12 h. Dried  $\text{TM}(\text{OH})_2$  precursors were ground with a stoichiometric amount of  $\text{Li}_2\text{CO}_3$  (99.3%, Fisher scientific) and  $\text{Na}_2\text{CO}_3$  (anhydrous, 99.5%, Strem chemicals) using agate mortar and pestle for 30 min. Pre-calcination was performed at 500 °C for 5 h in air. The powder was ground again and pressed into pellets. The final calcination process was conducted at 900 °C for 12 h in air. The stoichiometry of the as-synthesized compound was determined by inductively coupled plasma-optical emission spectroscopy (ICP-OES) and the formula of  $\text{Na}_{0.87}\text{Li}_{0.13}\text{Ni}_{0.22}\text{Mn}_{0.66}\text{O}_2$  (normalized to Mn) was confirmed. The presence of excess Na may be caused by a stoichiometric excess in the  $\text{Na}_2\text{CO}_3$  precursor added during the synthesis.

Time of flight (TOF) powder neutron diffraction data were collected on the POWGEN instrument at the Spallation Neutron Source (SNS) in the Oak Ridge National Lab (ORNL). A vanadium container was filled with around 2 g of powder and sent via the mail-in service to the SNS. Data were collected at a wavelength of 1.066 Å to cover a d-spacing range of 0.3–3.0 Å. The histograms were refined using Rietveld refinement with the GSAS software.<sup>175</sup>

All  $^7\text{Li}$  NMR experiments were performed at a magic-angle spinning (MAS) frequency of 60 kHz, using a Bruker 1.3 mm double-resonance HX probe and a recycle delay of 20 ms.  $^7\text{Li}$  NMR chemical shifts were referenced against solid  $^7\text{Li}_2\text{CO}_3$ . Isotropic shifts were extracted by using 2D adiabatic magic angle turning (aMAT)<sup>176</sup> and projection-magic angle turning phase-alternating spinning sideband (pj-MATPASS) experiments<sup>177</sup>, which are adaptations of conventional MAT experiments<sup>178</sup>. The 2D

aMAT experiment was performed on as-synthesized  $\text{P2-Na}_{0.8}[\text{Li}_{0.12}\text{Ni}_{0.22}\text{Mn}_{0.66}]\text{O}_2$  on a Bruker Avance III 500 wide-bore spectrometer operating at a  $^7\text{Li}$  Larmor frequency of -194.6 MHz. The sample temperature was regulated with a flow of  $\text{N}_2$  gas (273 K at a flow rate of 1200 l/h) using a Bruker BCU-X. Frequency-swept adiabatic pulses were used to obtain a uniform excitation of the broad  $^7\text{Li}$  resonances in paramagnetic  $\text{P2-Na}_{0.8}[\text{Li}_{0.12}\text{Ni}_{0.22}\text{Mn}_{0.66}]\text{O}_2$ . The aMAT spectrum was obtained using a train of six such  $\pi \tanh/\tan$  short high-power adiabatic pulses (SHAPs)<sup>179, 180</sup> of length 50  $\mu\text{s}$  and sweep width 5 MHz applied at an RF field amplitude of 357 kHz. 2D pj-MATPASS and rotor-synchronized 1D Hahn echo experiments on as-synthesized and cycled  $\text{P2-Na}_{0.8}[\text{Li}_{0.12}\text{Ni}_{0.22}\text{Mn}_{0.66}]\text{O}_2$  samples were recorded at room temperature on a Bruker Avance III 200 wide-bore spectrometer and at a  $^7\text{Li}$  Larmor frequency of -77.9 MHz. pj-MATPASS and Hahn echo spectra were obtained using  $\pi/2$  non-selective pulses of length 0.95  $\mu\text{s}$  at 260 kHz RF field. Each aMAT and pj-MATPASS experiment took between 8 and 13 hours. Lineshape analysis was carried out using the SOLA lineshape simulation package within the Bruker Topspin software and dmfit.<sup>181</sup>

High quality XRD patterns were continuously collected in transmission mode at the X14A beamline of the National Synchrotron Light Source (NSLS) using a linear position sensitive silicon detector. Customized coin cells with holes on both sides and covered with Kapton tape were used for in-situ measurement at a wavelength of 0.7784 Å. XRD patterns were collected between  $4.9^\circ$  and  $41.0^\circ$  in  $2\Theta$  angles. The data collection time for each XRD scan was 10 minutes. Rietveld refinement of the XRD data was carried out using the FullProf software package.

X-ray absorption spectroscopy experiments were performed at the X11B beamline of the National Synchrotron Light Source (NSLS) at Brookhaven national laboratory. Electrode samples were washed using battery grade diethylene carbonate (DEC) 3 times. Higher harmonics in the X-ray beam were minimized by detuning the Si (111) monochromator by 40% at the Ni K-edge (8333 eV) and at the Mn K-edge (6539 eV). Transmission spectra were collected along with a simultaneous spectrum on a reference foil of metallic Ni and Mn to ensure consistent energy calibration. Energy calibration was carried out using the first derivative of the spectra of the Ni and Mn metal foils. The data were analyzed and refined using the Ifeffit<sup>182</sup> and Horae<sup>183</sup> packages.

Cathode electrodes were prepared by mixing 85 wt% Na<sub>0.8</sub>[Li<sub>0.12</sub>Ni<sub>0.22</sub>Mn<sub>0.66</sub>]O<sub>2</sub> with 10 wt% acetylene black (Strem chemicals) and 5 wt% polytetrafluoroethylene (PTFE). Na metal (Sigma-Aldrich) was used as the counter electrode. 1M NaPF<sub>6</sub> (99%, Stremchemicals) dissolved in a 2:1 mixture of battery grade DEC and ethylene carbonate (EC) (Novolyte) was used as the electrolyte and the glass fiber GF/D (Whatman) was used as the separator. Swagelok type batteries were assembled in an Ar-filled glovebox (H<sub>2</sub>O < 0.1 ppm) and tested on an Arbin battery cycler in galvanostatic mode.

### 5.3. Results and discussion

#### 5.3.1 Electrochemical performances of Na<sub>0.80</sub>[Li<sub>0.12</sub>Ni<sub>0.22</sub>Mn<sub>0.66</sub>]O<sub>2</sub>

The theoretical capacity of P2–Na<sub>0.8</sub>[Li<sub>0.12</sub>Ni<sub>0.22</sub>Mn<sub>0.66</sub>]O<sub>2</sub> is 118 mAh g<sup>-1</sup>, considering the Ni<sup>2+</sup>/Ni<sup>4+</sup> redox reaction associated with 0.44 moles of Na ions. As shown in Figure 5.1(a), the material exhibits 133 mAh g<sup>-1</sup> capacity after the 1<sup>st</sup> charge, which is 15 mAh g<sup>-1</sup> higher than the theoretical value, presumably due to electrolyte decomposition and the formation of a solid electrolyte interphase.<sup>39</sup> Starting from the 2<sup>nd</sup>

cycle, the electrochemical profiles of the subsequent 30 cycles almost completely overlap and reveal that about 115 mAh g<sup>-1</sup> of specific capacity is obtained reversibly. Even up to the 50<sup>th</sup> cycle, capacity retention is still as high as 91% without any optimization of the electrodes via, for example, carbon coating, nano-scale fabrication, and the use of electrolyte additives. More importantly, the voltage profile displays a smooth curve between 2.0 and 4.4 V for both charge and discharge, indicating that intercalation proceeds via a solid-solution mechanism. Similar phenomena have been observed for the compound Na<sub>1.0</sub>Li<sub>0.2</sub>Ni<sub>0.25</sub>Mn<sub>0.7</sub> by Kim et. al.<sup>39</sup> On the contrary, it has been reported that the structural analogue, P2 -Na<sub>2/3</sub>[Ni<sub>1/3</sub>Mn<sub>2/3</sub>]O<sub>2</sub>, displays multiple intermediate phases and a phase transformation in the voltage range of 2.0 ~ 4.5 V.<sup>184</sup> Therefore, it is speculated that the presence of Li in Na<sub>0.80</sub>[Li<sub>0.12</sub>Ni<sub>0.22</sub>Mn<sub>0.66</sub>]O<sub>2</sub> plays a crucial role in the electrochemical reaction mechanism. We further investigate the location and effect of Li substitution via *in situ* SXRD and *ex situ* NMR in later sections. Superior rate performance has been obtained and is illustrated in Figure 5.1(b). The electrode delivers 105.6 mAh g<sup>-1</sup> at C/2, 101.5 mAh g<sup>-1</sup> at 1C, 84.9 mAh g<sup>-1</sup> at 2C, corresponding to 72% of the theoretical capacity, and 70.8 mAh g<sup>-1</sup> at 5C, 60% of the theoretical value.

### 5.3.2. Structural characterization by neutron diffraction and NMR spectroscopy

Long- and short-range structural properties of as-synthesized Na<sub>0.80</sub>[Li<sub>0.12</sub>Ni<sub>0.22</sub>Mn<sub>0.66</sub>]O<sub>2</sub>, such as the formation of superlattice structures and the Li-ion local environments, were investigated using XRD, neutron diffraction and <sup>7</sup>Li solid-state NMR spectroscopy. All the XRD peaks (Figure 5.2(a)) could be indexed using the space group *P6<sub>3</sub>/mmc*, and results from refinement are listed in Table 5.2. Figure 5.3 (a) shows

the neutron diffraction pattern along with the Rietveld refinement. The inset presents a magnified view of the 2.0-2.25 Å region and clearly demonstrates the presence of superstructure. The Miller indices of the peaks indicating Ni/Mn ordering on a  $\sqrt{3}a \times \sqrt{3}a$  superlattice are (020), (021), (121), and (122); these are technically “systematically absent” when using the “small hexagonal” model with cell length  $a$  ( $P6_3/mmc$ ). Previous work on  $\text{LiNi}_{1/2}\text{Mn}_{1/2}\text{O}_2$  and  $\text{Na}_{2/3}\text{Ni}_{1/3}\text{Mn}_{2/3}\text{O}_2$  layered materials has demonstrated that Ni/Mn ordering in the TM layer can be described by a “honeycomb” lattice.<sup>185, 186</sup> Therefore, a “large hexagonal” model ( $P6_3$ ) of the TM superlattice, with a  $\sqrt{3}a \times \sqrt{3}a$  unit cell (where  $a$  is the cell parameter of the material with no cation ordering), is used to fit the diffraction patterns.<sup>185</sup> In this model, three different TM positions at (0, 0, 0), (1/3, 2/3, 0) and (1/3, 2/3, 1/2), are present. The refined coordinates of all atoms, and their site occupancies in the large hexagonal model, are given in Table 5.1. The inset of Figure 5.3 (a) indicates that (020) and (021) peaks are present, although we were not able to obtain a good fit of their intensities. This indicates that there is Li/Ni/Mn ordering in the TM layer but XRD is unable to capture all the details even in the large hexagonal cell model. Solid-state NMR experiments were therefore performed to investigate the short-range structure.

Li-ion local environments in the pristine  $\text{P2-Na}_{0.8}[\text{Li}_{0.12}\text{Ni}_{0.22}\text{Mn}_{0.66}]\text{O}_2$  phase were studied using  $^7\text{Li}$  MAS NMR spectroscopy.  $^{23}\text{Na}$  MAS NMR experiments were also performed and the results will be presented in a separate publication. The  $^7\text{Li}$  resonance frequency of a Li ion surrounded by  $\text{Ni}^{2+}$  and  $\text{Mn}^{4+}$  ions is mainly affected by the Fermi contact interaction specific to the TM configuration around the observed nucleus.<sup>187</sup> Both pseudo-contact and quadrupolar contributions to the  $^7\text{Li}$  resonance frequency can be

considered negligible compared to the much larger hyperfine interactions.<sup>187, 188</sup> A 2D aMAT experiment was performed in order to resolve the multiple resonances of the  ${}^7\text{Li}$  sites. The 2D spectrum is plotted in Figure 5.3 (b) along with 1D projections from  ${}^7\text{Li}$  double adiabatic spin echo (DASE) experiment (top) and a sum projection of the isotropic dimension (left). At least seven  ${}^7\text{Li}$  isotropic shifts are clearly observed at 5, 237, 577, 753, 1186, 1486 and around 1700 ppm in the F1 sum spectrum, and their corresponding sideband manifolds are plotted on the right.

Based on a previous  ${}^6\text{Li}$  NMR study of  $\text{Li}_2\text{MnO}_3$ <sup>188</sup> we can assign the resonances of  $\text{Li}_1$  (ca. 1700 ppm),  $\text{Li}_2$  (1486 ppm), and  $\text{Li}_3$  (1186 ppm) to Li sites in a honeycomb-like arrangement within the  $\text{TMO}_2$  layer. By analogy with our results for  $\text{Li}_2\text{MnO}_2$ - $\text{Li}(\text{NiMn})_{0.5}\text{O}_2$  “lithium-excess” materials,<sup>189</sup> we further assign  $\text{Li}_1$  to Li ions surrounded by 6 nearest neighbour  $\text{Mn}^{4+}$ , and  $\text{Li}_2$  to 5  $\text{Mn}^{4+}$  and 1  $\text{Ni}^{2+}$ . The 1D Hahn echo spectrum collected on the pristine material (Figure 5.7) reveals that the  $\text{Li}_1$  resonance results from the overlap of signals from two distinct Li environments with isotropic shifts at ca. 1760 ppm and 1700 ppm. Inhomogeneous broadening of the aMAT spectrum, likely due to a combination of Anisotropic Bulk Magnetic Susceptibility (ABMS) effects, temperature gradients across the sample at 60 kHz MAS, and structural disorder, leads to significant broadening of the 1700 ppm peak, so as to inhibit the resolution of the neighbouring peak at ca. 1760 ppm. *Ab initio* and experimentally-derived TM-(O-)Li bond pathway contributions for Li-ions in octahedral environments in the  $\text{TMO}_2$  layer are in good agreement with these general trends and will be discussed in a future publication.

Cabana et al. have studied the T2/O2 ion-exchanged  $\text{Li}_{0.67}\text{Ni}_{0.33}\text{Mn}_{0.67}\text{O}_2$  compound and following their findings we assign  $\text{Li}_4$  (753 ppm) and  $\text{Li}_5$  (577 ppm)

resonances to octahedrally-distorted sites in the Na layer.<sup>190</sup> A greater concentration of Ni in the first coordination shell of Li<sub>5</sub> may account for its lower shift compared to that of Li<sub>4</sub> (by analogy with related Li phases<sup>189</sup>).

As the main lithium resonance in T2/O2 ion-exchanged Li<sub>0.67</sub>Ni<sub>0.33</sub>Mn<sub>0.67</sub>O<sub>2</sub> appears at 370 ppm we can assign Li<sub>6</sub> (237 ppm) and Li<sub>7</sub> (5 ppm) to tetrahedrally-distorted sites in the Na layer, occurring as small defects in the ideal structure. The difference in O-layer stacking (P2 vs. O2/T2) may account for the discrepancy in Li shifts in the two materials. The relatively low Li<sub>6</sub> and Li<sub>7</sub> hyperfine shifts can be rationalised in terms of the smaller number of TM-O-Li connectivities associated with tetrahedral Li, compared to 6-coordinate Li.

By taking slices along the F2 dimension of the aMAT spectrum (right-hand side figure 5.3 (b)) we can observe the sideband patterns of all distinguishable Li environments in P2-Na<sub>0.80</sub>[Li<sub>0.12</sub>Ni<sub>0.22</sub>Mn<sub>0.66</sub>]O<sub>2</sub>. Comparison of the F2 slices reveals a sudden change in the anisotropy of the through space (dipolar) interaction between the Li nucleus and neighbouring unpaired TM d-electrons from Li<sub>1</sub> to Li<sub>7</sub>. As observed previously, for example in Li<sub>2</sub>MnO<sub>3</sub><sup>188</sup>, ions in the TMO<sub>2</sub> layer (Li<sub>1</sub>, Li<sub>2</sub> and Li<sub>3</sub>) are expected to have an anisotropy with an opposite sign to that of ions in between TM layers (Li<sub>4</sub> and Li<sub>5</sub>), confirming their assignments.

The relative population of the Li sites was determined by integration of the 1D Hahn echo spectrum. After correcting for spin-spin relaxation during the NMR pulse sequence, the distribution of Li among the different local environments was found to be: Li<sub>1</sub>: 73.5 %; Li<sub>2</sub>: 11 %; Li<sub>3</sub>: 2 %; Li<sub>4</sub>: 5 %; Li<sub>5</sub>: 3 %; Li<sub>6</sub>: 5 %; Li<sub>7</sub>: 0.5 %, with an estimated error below ± 5 %. Detailed information about Li site-specific transversal

(spin-spin) relaxation times can be found in Table S6 (Supporting Information). A decrease in Li site population is observed in the aMAT spectrum as the concentration of Ni in the first coordination shell increases. The occupation of Li environments with more than two Ni nearest neighbours is probably too small for these environments to be seen experimentally.

Both neutron diffraction and  $^7\text{Li}$  NMR data confirm our initial assumption whereby  $\text{Li}^+$  primarily occupies octahedral sites in the  $\text{TMO}_2$  layer (85% of  $\text{Li}^+$  ions are present in the  $\text{TMO}_2$  layer according to NMR) and preferentially exchanges with a  $\text{Ni}^{2+}$  ion. The final Li/Ni/Mn distribution deviates from a simple honeycomb arrangement and exhibits a small amount of Ni/Mn exchange within the  $\text{TMO}_2$  layer.  $^7\text{Li}$  NMR also shows that about 15% of  $\text{Li}^+$  ions can be found in  $\text{O}_h/\text{T}_d$  sites in the Na layer.

### 5.3.3. Structural evolution during charge monitored by *in situ* synchrotron XRD

Phase transformations occurring upon Na-ion extraction were monitored using *in situ* SXRD. In Figure 5.4 (a), selected sections of the SXRD patterns are shown together with the pristine powder pattern at the bottom, and the voltage profile on the right. Refined  $a$  and  $c$  lattice parameters, which include the values found in the pristine material, are presented in Figure 5.4 (b). The *in situ* scan was set to start at 3.43 V and end at 4.40 V. Comparison of the whole set of *in situ* patterns to the pristine powder pattern reveals that all of the major reflections corresponding to the P2 phase are clearly maintained, which demonstrates that no significant phase transformation has occurred. Some of the shifts in peak positions are mainly due to lattice distortions induced by Na-ion extraction. In particular, a gradual shift of the (100) peak towards the high angle end is observed

upon charge, in agreement with a decrease in the  $a$  lattice parameter. Since the  $a$  lattice parameter corresponds to TM-TM distances, oxidation of TMs upon charge leads to slightly shorter distances between TM. On the other hand, it is obvious that the (004) peak moves towards the low angle end until the cell is charged up to 4.05 V, suggesting an expansion in  $c$  lattice parameter upon charge due to the increased electrostatic repulsion between successive oxygen layers caused by the removal of Na ions.<sup>35</sup> No noticeable change in the position of the (004) peak can be detected once the voltage has reached 4.05 V. Rietveld refinement suggests a slight decrease in  $c$  lattice parameter after 4.05 V charge. In the pristine material, Na ions occupy trigonal prismatic sites between neighboring oxygen layers. When some of the Na ions are extracted during charge, TMO<sub>2</sub> slabs glide along the  $a$ - $b$  plane to avoid close oxygen-oxygen contacts. There are two possible directions for these glides (Figure 5.4 (c) inset) resulting in a close-packed arrangement of neighboring oxygen layers. Consequently, stacking faults are formed instead of a long-range ordered phase. The presence of these stacking faults within the P2 phase severely broadens (10l) peaks (e.g. (104) and (106)) in the experimental SXRD pattern.<sup>141, 184, 191</sup> As shown in Figure 5.4 (c), such broadening of the XRD pattern due to stacking faults can be simulated using the software CrystalDiffract for Windows 1.4.5<sup>192, 193</sup>. An increase in the concentration of stacking faults results in a clear broadening of the (104) and (106) peaks, which is consistent with experimental observations. Therefore, it is believed that the concentration of stacking faults in the structure progressively increases as the material approaches the end of charge (4.4 V) and accounts for the decrease in  $c$  lattice parameter after a large amount of Na ions has been removed from the TMO<sub>2</sub> slabs. After one full cycle, complete recovery of the layered P2 structure is

confirmed by the presence of sharp, well-defined SXRD peaks at the same positions as those observed for the pristine structure (Figure 5.5 (a)). The reason for this is the alignment of TM ions along the  $c$  axis of the P2 structure to form trigonal prismatic Na sites. Hence, when Na ions are re-inserted back into the structure, stacking faults are eliminated in such a way that Na-ion prismatic sites can be reconstructed.

#### 5.3.4. Li site change studied by ex-situ NMR

In Figure 5.6,  $^7\text{Li}$  1D slices are extracted from 2D projection-MATPASS (pj-MATPASS) NMR spectra acquired at 200 MHz on as-synthesized P2- $\text{Na}_{0.8}[\text{Li}_{0.12}\text{Ni}_{0.22}\text{Mn}_{0.66}]\text{O}_2$  and at 4.1 V, 4.4 V charge, and 2 V discharge along the first electrochemical cycle. These 1D slices reveal the position of the  $^7\text{Li}$  isotropic shifts and enable us to monitor changes in  $^7\text{Li}$  local environments as a function of (dis)charge. Note that the intensity of the peaks in the pj-MATPASS isotropic row of the pristine material (Figure 5.6) do not match those found in the aMAT F1 sum (Figure 5.3(b)) spectrum of the same compound as these projections do not contain quantitative information on the population of the different Li sites.

While the  $^7\text{Li}$  NMR spectra at 4.1 V charge and 2 V discharge look very similar to the spectrum of the pristine sample, major changes in the relative occupation of Li local environments occur between 4.1 and 4.4 V on charge. Li site occupations were monitored as a function of cycling by integration of Hahn echo spectra recorded at the four stages of the first cycle mentioned above, and after 5 electrochemical cycles (see Table 5.3 below and Figure 5.7 of the Supporting Information). Contributions from individual Li sites were scaled by a transverse relaxation factor accounting for the loss of NMR signal

intensity over the signal acquisition time. The Li content in each layer was obtained by integration of  $^7\text{Li}$  Hahn echo spectra recorded at the four stages of the first cycle mentioned above, and after 5 electrochemical cycles and is expressed as a percentage of the total Li content in the pristine phase. The Li stoichiometry decreases from 0.12 to 0.086 Li per formula unit upon initial charging to 4.1 V, mainly due to the loss of Li in  $\text{O}_h$  and  $\text{T}_d$  sites in the Na layer, and, to a smaller extent, to Li loss in the  $\text{TMO}_2$  layer. Between 4.1 and 4.4 V charge the  $^7\text{Li}$  NMR spectrum changes significantly. Most Li present in  $\text{TMO}_2$  layers moves to Na layers and only 5% of the total Li content in the pristine sample is left in the  $\text{TMO}_2$  layer at the end of the first charge. This result can be rationalized using *in situ* XRD data, which demonstrate the presence of O2-like stacking faults and octahedral (rather than prismatic) sites in the Na layer, inducing Li migration from  $\text{TMO}_2$  to Na layers or driven by Li migration. It is difficult to say at this stage if stacking faults enable Li migration, or conversely, if Li-ion mobility facilitates the formation of stacking faults. By the end of charge, most of the Li left in the cathode has moved to  $\text{O}_h$ ,  $\text{T}_d$  or other low coordination sites in the Na layer, giving rise to a sharp end-of-charge peak at ca. 100 ppm. The low hyperfine shift may indicate a  $\text{Ni}^{4+}$ -rich environment, since this cation is diamagnetic (low spin  $d^0$  configuration) and will not contribute to the  $^7\text{Li}$  Fermi contact shift.

An NMR and first-principles calculations study on  $\text{O3-Li}[\text{Li}_{(1-2x)/3}\text{Mn}_{(2-x)/3}\text{Ni}_x]\text{O}_2$  by Grey et al.<sup>194</sup> showed that the small amount of  $\text{Li}^+$ -ions occupying octahedral sites in  $\text{TMO}_2$  layers participates in the electrochemistry of the cathode by moving spontaneously to a  $\text{T}_d$  site in Li layers at low potentials, when the four octahedral sites (three in the Li layer and one in the TM layer) that share faces with this  $\text{T}_d$  site are vacant. A similar

scenario may occur in P2- $\text{Na}_{0.8}[\text{Li}_{0.12}\text{Ni}_{0.22}\text{Mn}_{0.66}]\text{O}_2$ , whereby Li directly above a face-sharing Na drops into the space left by Na after the latter is removed during charge and occupies a tetrahedral or trigonal site in the Na layer. This may give rise to a low coordination Li environment, and, if Li is surrounded by a majority of diamagnetic  $\text{Ni}^{4+}$  ions, account for the 100 ppm NMR resonance.

The Li stoichiometry of the sample, which dropped from 0.086 to 0.051 between 4.1 and 4.4 V charge, increases again to 0.086 by the end of the first discharge. The spectrum at 2 V discharge is very similar to that of the pristine phase, suggesting the reversibility of O2-like stacking faults and of Li migration back to  $\text{TMO}_2$  layer sites upon discharge. There is no significant change in total Li content between the end of the first and of the fifth cycles, hence no more irreversible loss of Li in the electrode after the first cycle. The ratio of Li occupation of Na layer sites to that of  $\text{TMO}_2$  sites is higher in the pristine phase (ca. 0.08) than in the fully discharged sample (ca. 0.04) and suggests higher reversibility of Li in the transition metal layer than in the Na layer.

### 5.3.5. Electronic and local structural changes by XAS

In order to investigate charge compensation mechanisms, XAS measurements were conducted at the Ni (8333 eV) and Mn K-edges (6539 eV) at different states of charge (see Figure 5.8(a) and 5.9(a)). It is evident that the as-synthesized  $\text{Na}_{0.8}[\text{Li}_{0.12}\text{Ni}_{0.22}\text{Mn}_{0.66}]\text{O}_2$  compound predominantly consists of  $\text{Ni}^{2+}$  and  $\text{Mn}^{4+}$  ions. The Ni K-edge absorption shifts to a higher energy region when the electrode is charged to 4.1 V, and moves further when the electrode is charged to 4.4 V. The energy shift for the 4.4 V charged electrode is  $\sim 3$  eV, which is larger than that of the  $\text{Ni}^{2+}$  to  $\text{Ni}^{3+}$  shift ( $\sim 2$  eV)

suggesting that the oxidation state of Ni is close to  $\text{Ni}^{4+}$ .<sup>30</sup> After the electrode is discharged to 2.0 V, the Ni-ions return back to their divalent state, demonstrating that the Ni redox reaction is completely reversible in the Na-ion cell. In contrast to the Ni XANES, Mn stays in its tetravalent state during charge and discharge (see Figure S4 (a)). Based on the reversible capacity shown in Figure 1 (a), 0.44 moles of Na-ions per formula unit migrate upon cycling, delivering  $118 \text{ mAh g}^{-1}$  of capacity. This means that all  $\text{Ni}^{2+}$  ions present in the pristine phase are fully oxidized to  $\text{Ni}^{4+}$  to balance the overall charge of the system.

Extended X-ray absorption fine structure (EXAFS) spectra were further analyzed. As shown in Figure 5.8 (b), the Ni EXAFS clearly shows that the Ni-O interatomic distance, around 1.5 Å in the pristine phase, decreases upon charge due to the oxidation of  $\text{Ni}^{2+}$  to  $\text{Ni}^{4+}$ . The Ni-O distance reverts back to its initial value by the end of the first discharge, in good agreement with XANES results. On the other hand, the Mn EXAFS does not show any obvious changes in the Mn-O interatomic distance. (Figure 5.9 (b)) The XAS proves that Ni is the only electrochemically active species and Mn maintains the structural stability in the absence of Jahn-Teller active  $\text{Mn}^{3+}$ .

### 5.3.6. The role of Li substitution in $\text{Na}_{0.8}[\text{Li}_{0.12}\text{Ni}_{0.22}\text{Mn}_{0.66}]\text{O}_2$

The sites substituted by Li in the as-synthesized  $\text{Na}_{0.8}[\text{Li}_{0.12}\text{Ni}_{0.22}\text{Mn}_{0.66}]\text{O}_2$  compound were identified by using both NMR and neutron diffraction. Although a small amount of Li ions can be found in octahedrally-coordinated Na layer sites, presumably as a result of O-type defects (ABCABC or ABAB oxygen stacking<sup>195</sup>), most Li-ions are not stable in the large prismatic Na sites and occupy TM sites. As expected, Li-ions

preferentially occupy TM sites with a high number of nearest neighbor  $\text{Mn}^{4+}$  ions (4, 5 or 6). This suggests that they preferentially replace  $\text{Ni}^{2+}$  ions in the  $\text{TMO}_2$  layer, since the monovalent  $\text{Li}^+$  ion can reduce in-plane electrostatic repulsion between cations as well as disrupt the cation orderings. As opposed to Li-free P2 cathodes, single smooth voltage curves are obtained rather than step-like electrochemical profiles suggesting that no significant structural changes occur during cycling. Rather than a P2-O2 phase transformation, *in situ* SXRD suggests the presence of local O2-like stacking faults at the end of charge. The presence of stacking faults has also been confirmed by *ex situ* NMR, which reveals a five-fold increase in the occupation of octahedral Na layer sites by Li between 4.1 and 4.4 V charge.

The effect of Li substitution upon the electrode's electrochemical performance was studied by charging the cell using constant current constant voltage (CCCV) to pull all of the Na ions out (0.80 moles of Na-ions per formula unit) below 4.4 V, in order to avoid electrolyte decomposition. After all Na-ions were extracted from the structure, the O2 phase was clearly observed in *ex situ* XRD (Figure 5.5(b)), demonstrating that the P2–O2 phase transformation is delayed instead of being completely prevented. In other words, the O2 phase forms inevitably once all Na-ions are removed from the P2 phase. Therefore, the main characteristics of Li substitution and their possible consequences on phase transformation can be summarized as follows. Li ions prefer to occupy octahedrally-coordinated sites in the  $\text{TMO}_2$  layer with a high number of Mn nearest neighbor atoms, concurrently, the lower valence state of Li ions (monovalent) compared to that of Ni ions (divalent) requires more Na ions to be inserted in the as-synthesized material in order to maintain the overall charge balance of the compound. As a result,

approximately 0.36 moles of Na ions are left in prismatic sites after 4.4 V charge, which is enough to suppress the O2 phase transformation. Although Li ions in substituted TM sites migrate to octahedral sites or to tetrahedral sites in the Na layer created by local stacking faults, the amount of Li in the TM layer in the cycled electrode is largely recovered, suggesting that the migration of Li between octahedral sites in the Na layer and in the TM layer is highly reversible. We note that a fraction of Li is lost on the 1<sup>st</sup> cycle but that little seems to be lost in subsequent cycles. The excellent reversibility of Li migration of the remaining Li in this compound may account for its excellent capacity retention and its single smooth voltage curves throughout the whole cycling process.

### 5.3.7 Material design principles and $\text{Na}_{0.83}[\text{Li}_{0.07}\text{Ni}_{0.31}\text{Mn}_{0.62}]\text{O}_2$

In order to achieve both high energy density and structural stability, the stoichiometry of Li substituted P2 type cathodes can be further optimized. The above discussion, which focused on the crystallographic and electronic structural changes occurring upon cycling  $\text{Na}_{0.8}[\text{Li}_{0.12}\text{Ni}_{0.22}\text{Mn}_{0.66}]\text{O}_2$ , has led to the identification of several key conditions which need to be fulfilled for good electrochemical performance in P2 type cathodes. Here, we propose novel principles for the design of positive electrodes to obtain higher energy density cathode materials with stoichiometry  $\text{Na}_x[\text{Li}_y\text{Ni}_z\text{Mn}_{1-y-z}]\text{O}_2$  ( $0 < x, y, z < 1$ ). First, an increase in Na-ion concentration in the structure is required to deliver higher energy density and to maintain the P2 phase up to the end of charge. However, Na concentration in the as-synthesized material cannot be higher than 0.9 per formula unit if the extremely unfavorable simultaneous occupancy of nearest-neighbor Na sites in the P2 structure is to be prevented.<sup>33, 196, 197</sup> Second, a high proportion of Ni-

ions in the TM layer is essential to provide enough electrons via the oxidation of  $\text{Ni}^{2+}$  to  $\text{Ni}^{4+}$  for high voltage electrochemical processes. Third, the Ni to Mn ratio significantly affects the phase of the synthesized product. The highest ratio we can achieve is 1:2, and a further increase in Ni-ion concentration leads to the formation of impurities including transition metal oxides, or O3 phases. Fourth, overall charge balance of the compound has to be taken into account. The algebraic relationship between the x, y and z stoichiometric factors in the  $\text{Na}_x[\text{Li}_y\text{Ni}_z\text{Mn}_{1-y-z}]\text{O}_2$  formula is given by

$$x + y + 2 \times z + 4 \times (1 - y - z) = 2 \times 2 \quad (\text{eq. 5.1})$$

$$x < 0.9 \quad (\text{eq. 5.2})$$

$$1 - y - z = 2 \times z \quad (\text{eq. 5.3})$$

$$0 < x, y, z < 1 \quad (\text{eq. 5.4})$$

We suggest an optimum composition which fulfills all of the above conditions, in which  $x = 3 - 7z$ ,  $y = 1 - 3z$ , and  $0.3 < z < 0.33$ . A novel composition,  $\text{Na}_{0.83}[\text{Li}_{0.07}\text{Ni}_{0.31}\text{Mn}_{0.62}]\text{O}_2$ , is finally obtained, which can deliver  $140 \text{ mAh g}^{-1}$  of reversible capacity in the voltage range of  $2.0 \sim 4.4 \text{ V}$  (Figure 5.10). The stoichiometry was confirmed by ICP. As expected, no significant phase transformation was observed upon cycling based on our preliminary *in situ* XRD studies, except for a slight change in the voltage curves shown repeatedly in the high voltage region. This change may be the result of the formation of intermediate phases through Na-ion ordering.<sup>144, 196</sup> An in-depth study of Na-ion ordering this family of materials is currently in progress.

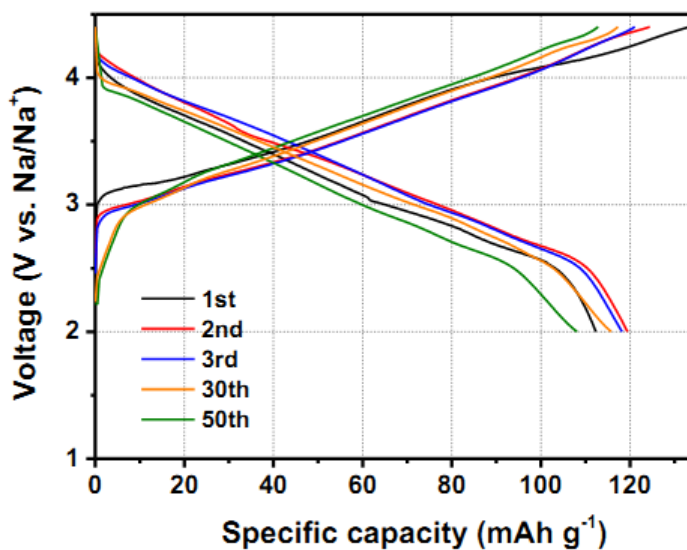
## 5.4 Conclusions

An in-depth understanding of the interplay between structural properties and electrochemical performances is required to improve the performances of Na-ion batteries. In this work, a promising Na cathode material,  $\text{P2-Na}_{0.8}[\text{Li}_{0.12}\text{Ni}_{0.22}\text{Mn}_{0.66}]\text{O}_2$ , has been comprehensively studied using neutron diffraction,  $^7\text{Li}$  solid-state MAS NMR, *in situ* SXR and XAS. Most of the substituted Li ions occupy TM sites with a high number of nearest-neighbor Mn ions (4, 5 or 6), a result confirmed by both neutron diffraction and NMR. Enhanced electrochemical properties, among which improved cycling performance and rate capability, are obtained along with single smooth voltage profiles. In contrast to most of the P2-type cathodes reported so far, *in situ* SXR proves that the frequently observed P2-O2 phase transformation is inhibited in this Li-substituted material even when the electrode is charged to 4.4 V. On the other hand, the P2 to O2 phase change is clearly observed when all of the Na ions are extracted from the structure under CCCV charge. Based on these observations, Li substitution in the TM layer enables enough Na ions to be left in the structure to maintain the P2 structure up to 4.4 V charge. Although Li-ions migrate to octahedral or, to a lesser extent, to low coordination sites in the Na layer formed by local stacking faults during the charging process, most of them return to the TM layer after discharge. XAS results show that  $\text{Ni}^{2+}/\text{Ni}^{4+}$  is the only active redox couple during cycling. Finally, an optimum composition,  $\text{Na}_{0.83}[\text{Li}_{0.07}\text{Ni}_{0.31}\text{Mn}_{0.62}]\text{O}_2$ , has been proposed on the basis of the design principles for Na-ion cathode elucidated as part of this study, opening up new perspectives for further exploration of high energy Na-ion batteries.

Chapter 5, in full, is a reprint of the “Identifying the Critical Role of Li Substitution in  $\text{P2-Na}_x[\text{Li}_y\text{Ni}_z\text{Mn}_{1-y-z}]\text{O}_2$  ( $0 < x, y, z < 1$ ) Intercalation Cathode Materials

for High Energy Na-ion Batteries”, as it appears in the Chemistry of Materials, Jing Xu, Dae Hoe Lee, Raphaele J. Clement, Xiqian Yu, Michal Leskes, Andrew J. Pell, Guido Pintacuda, Xiao-Qing Yang, Clare P. Grey, Ying Shirley Meng, 2014, 26, 1260-1269, The dissertation author was the co-primary investigator and author of this paper. The author conducted materials design, synthesis, electrochemical characterization, SXRD refinement and corresponding writing.

(a)



(b)

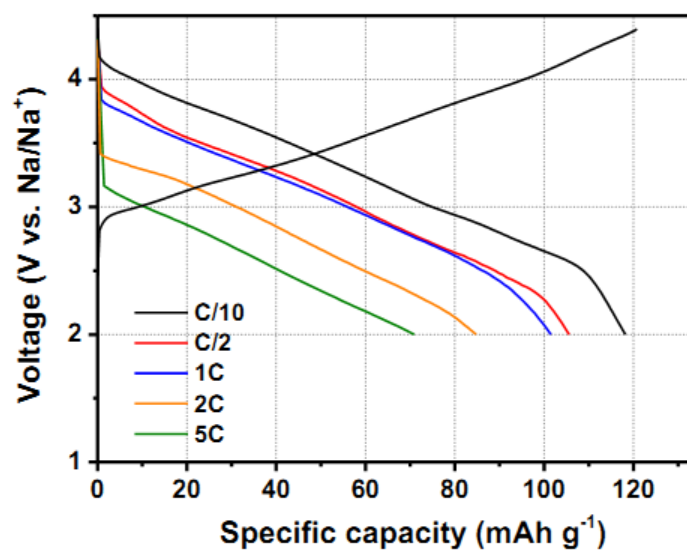
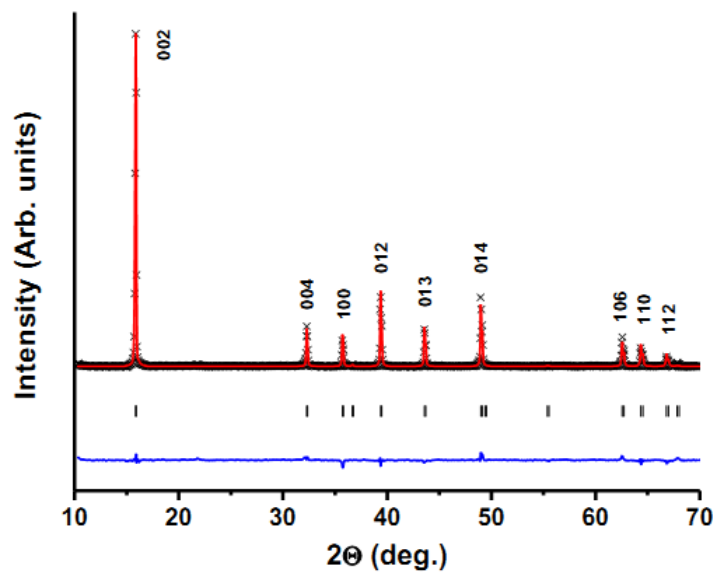


Figure 5.1 (a) Electrochemical profiles of  $\text{Na}_{0.80}[\text{Li}_{0.12}\text{Ni}_{0.22}\text{Mn}_{0.66}]\text{O}_2$  during the 1<sup>st</sup>, 2<sup>nd</sup>, 3<sup>rd</sup>, 30<sup>th</sup> and 50<sup>th</sup> cycles, and (b) its rate capability at different current densities from C/10 to 5C (calculated based on a theoretical capacity of  $118 \text{ mAhg}^{-1}$ ).

(a)



(b)

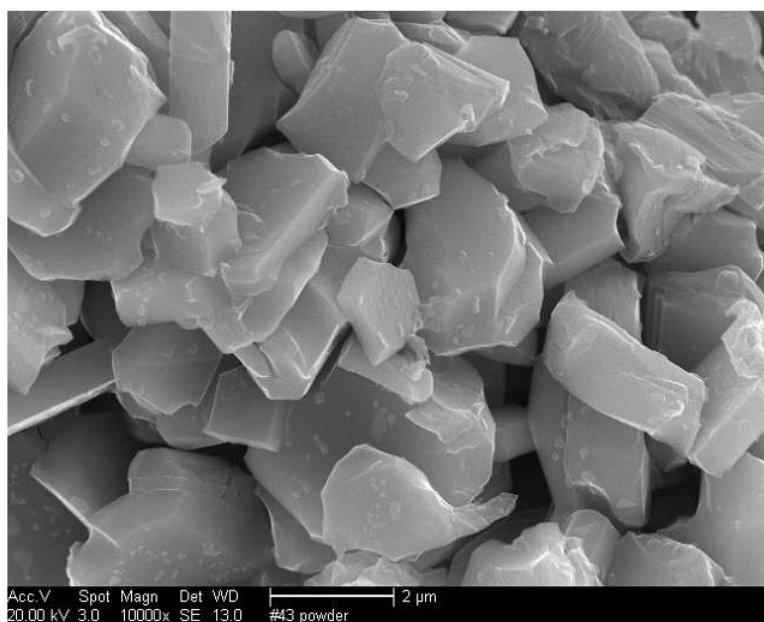
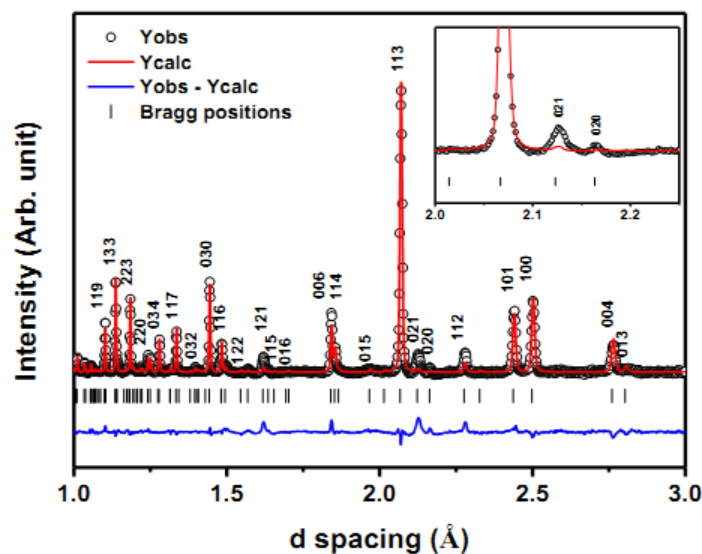


Figure 5.2 The (a) XRD and (b) SEM image of as-synthesized P2 –  $\text{Na}_{0.80}[\text{Li}_{0.12}\text{Ni}_{0.22}\text{Mn}_{0.66}]\text{O}_2$  powder.

(a)



(b)

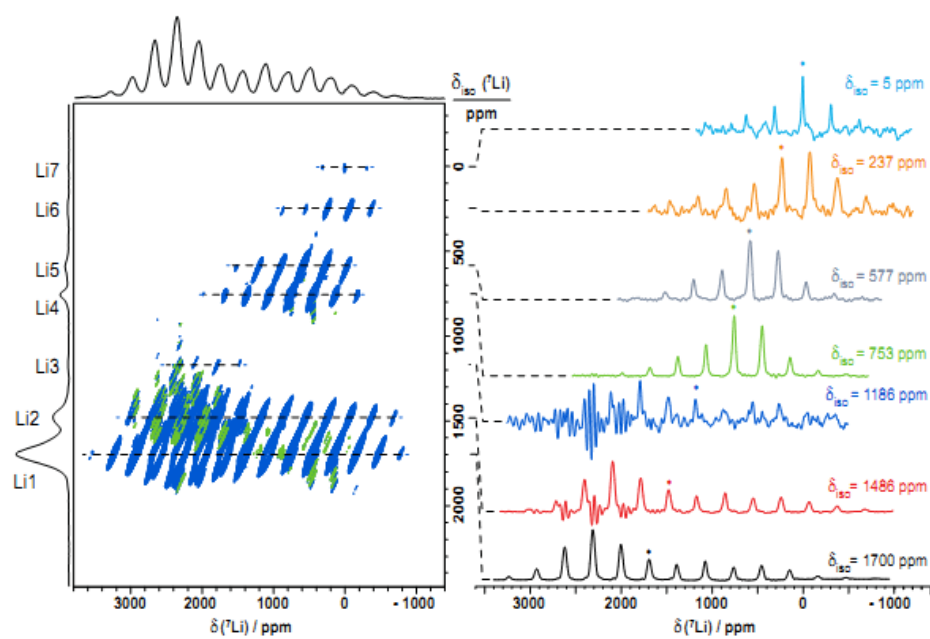


Figure 5.3 (a) Neutron diffraction patterns, including an extended view of the superlattice region (inset), and (b) the  $^7\text{Li}$  aMAT NMR spectrum of as-synthesized  $\text{P2-Na}_{0.80}[\text{Li}_{0.12}\text{Ni}_{0.22}\text{Mn}_{0.66}]\text{O}_2$  recorded at 500 MHz. In (b), the 1D double adiabatic spin echo (DASE) spectrum and the F1 sum spectrum are projected at the top and on the left-hand side of the 2D spectrum, respectively. Slices taken in the F2 dimension, centered about the  $^7\text{Li}$  isotropic shifts, are shown on the right-hand side.

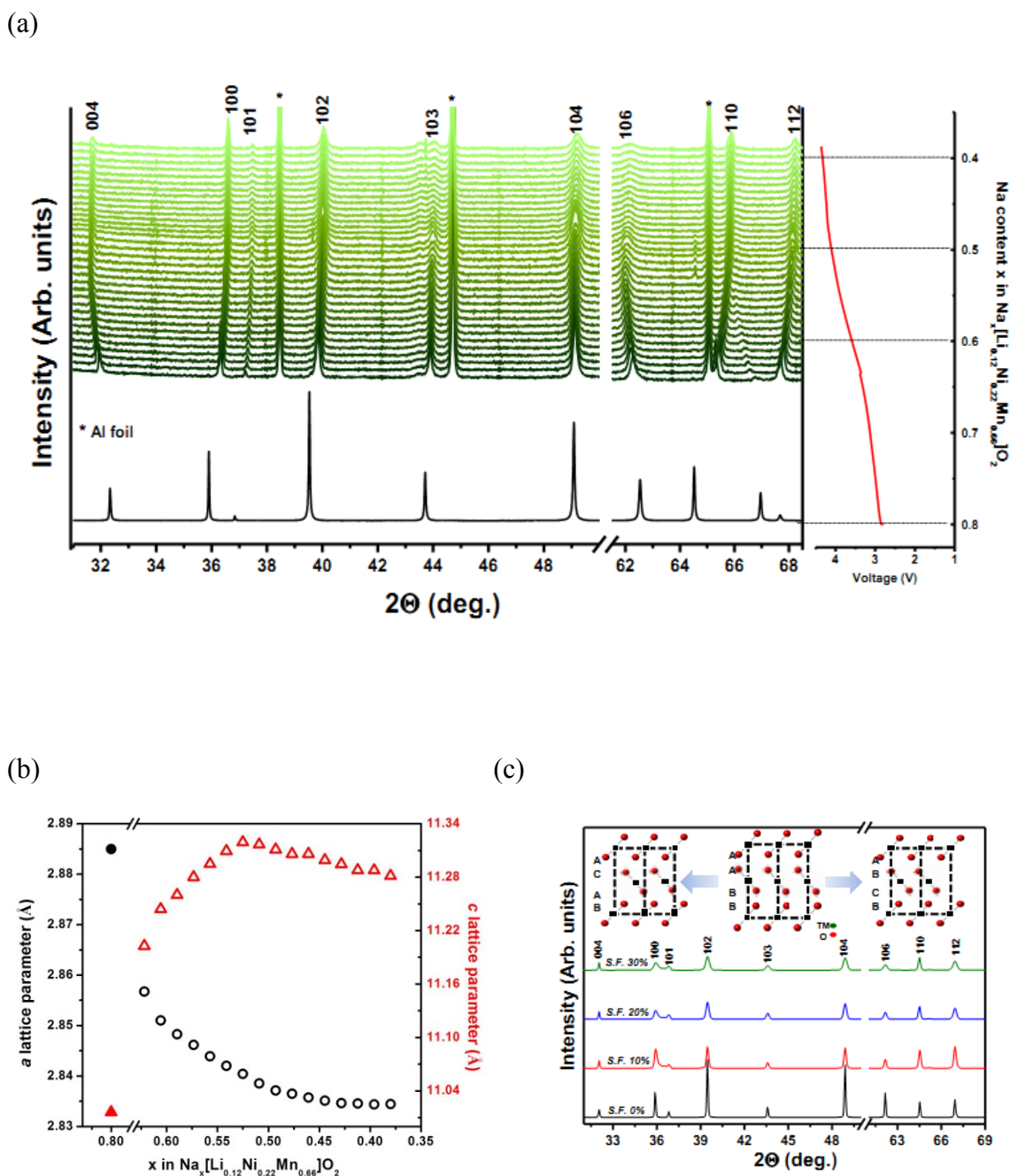
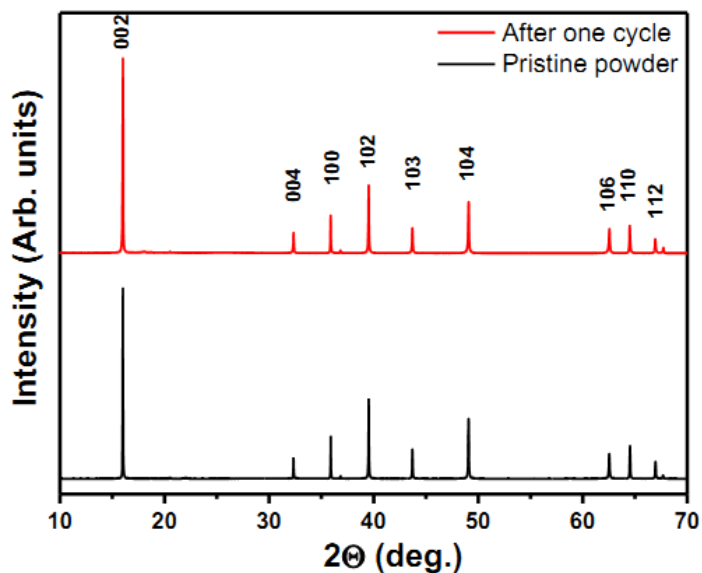


Figure 5.4 (a) *In situ* SXR D for  $\text{Na}_{0.80}[\text{Li}_{0.12}\text{Ni}_{0.22}\text{Mn}_{0.66}]\text{O}_2$  during the 1<sup>st</sup> charge. (\* indicates the Al current collector in the electrode), (b) changes in the  $a$  and  $c$  lattice parameters upon the 1<sup>st</sup> charge by the refinement. The solid markers represent the pristine state, and (c) simulated XRD patterns with different percentage of stacking faults by CrystalDiffract software

(a)



(b)

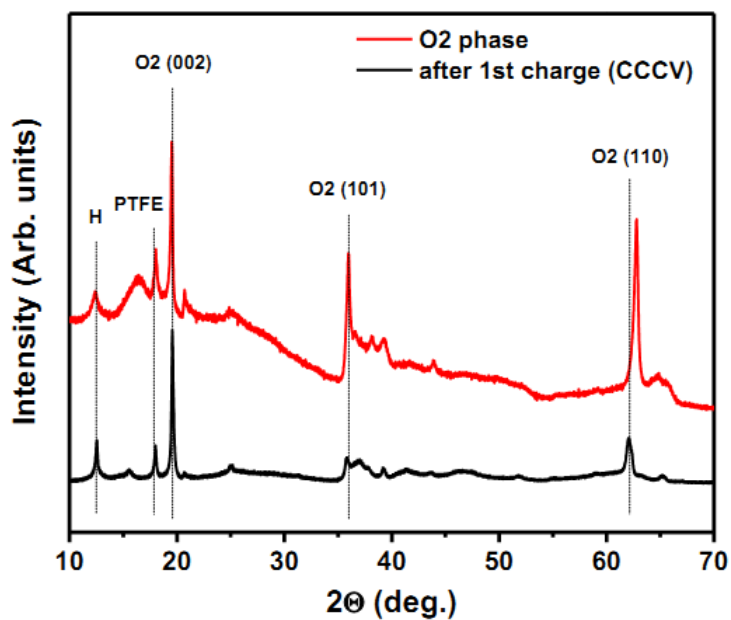


Figure 5.5 (a) Ex situ SXR D patterns of pristine and fully cycled  $\text{Na}_{0.80}[\text{Li}_{0.12}\text{Ni}_{0.22}\text{Mn}_{0.66}]\text{O}_2$ . (b) Comparison of ex situ SXR D pattern of  $\text{Na}_{0.80}[\text{Li}_{0.12}\text{Ni}_{0.22}\text{Mn}_{0.66}]\text{O}_2$  electrode after one full charge under CCCV to XRD pattern of the O<sub>2</sub> phase (including a hydrated phase).

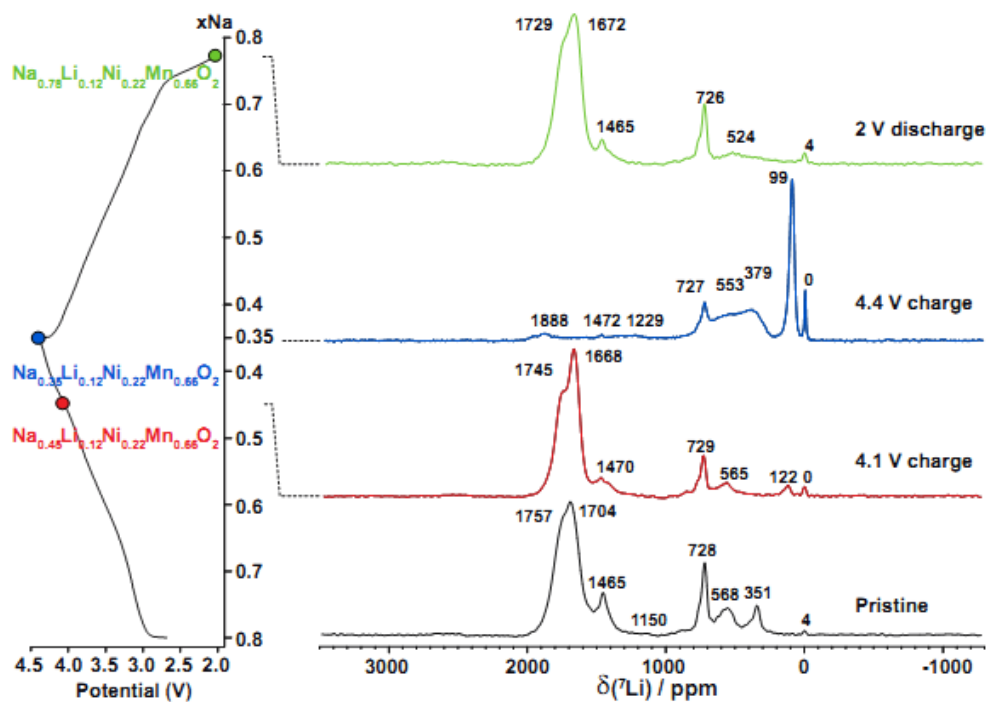


Figure 5.6 Isotropic slices of  ${}^7\text{Li}$  pj-MATPASS NMR spectra acquired at 200 MHz on as-synthesized  $\text{P2-Na}_{0.8}[\text{Li}_{0.12}\text{Ni}_{0.22}\text{Mn}_{0.66}]\text{O}_2$  and at three different stages along the first electrochemical cycle. pj-MATPASS experiments were performed using a train of five non-selective pulses. The spectra have not been scaled to represent the total Li content in the sample at each stage of the cycle.

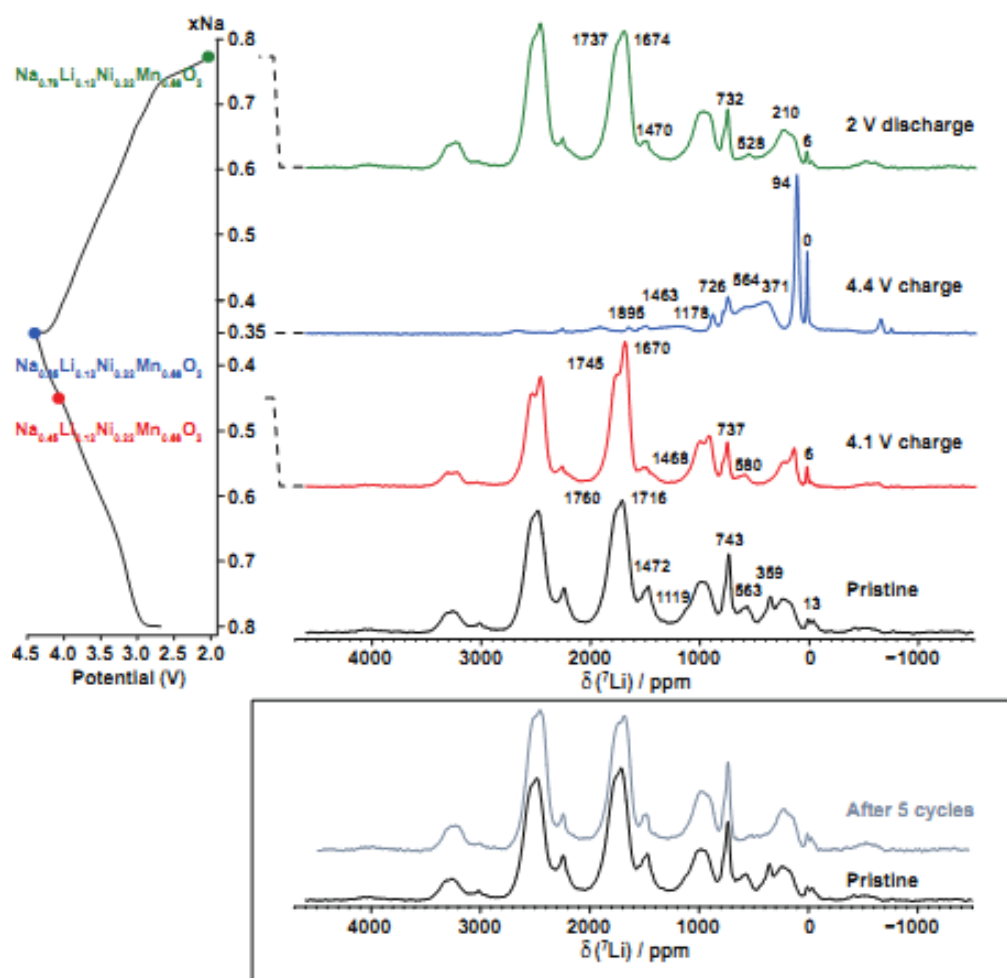
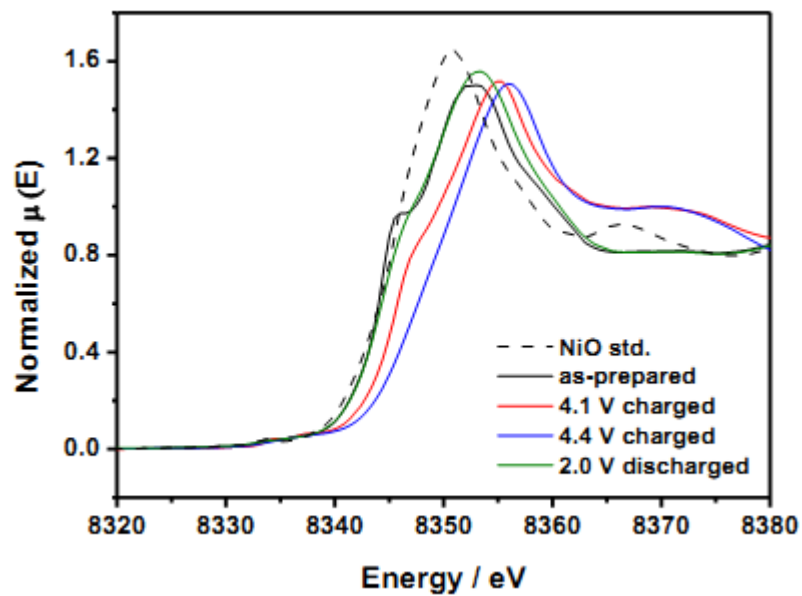


Figure 5.7  ${}^7\text{Li}$  Hahn echo spectra recorded of as-synthesized  $\text{Na}_{0.80}[\text{Li}_{0.12}\text{Ni}_{0.22}\text{Mn}_{0.66}]\text{O}_2$  and  $\text{Na}_{0.80}[\text{Li}_{0.12}\text{Ni}_{0.22}\text{Mn}_{0.66}]\text{O}_2$  charged to 4.1 V, 4.4 V, discharged to 2.0 V, and after 5 electrochemical cycles.

(a)



(b)

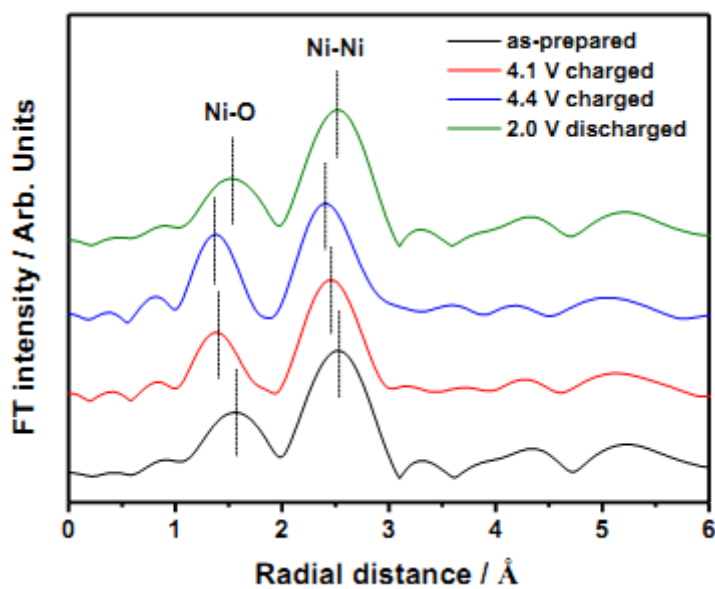
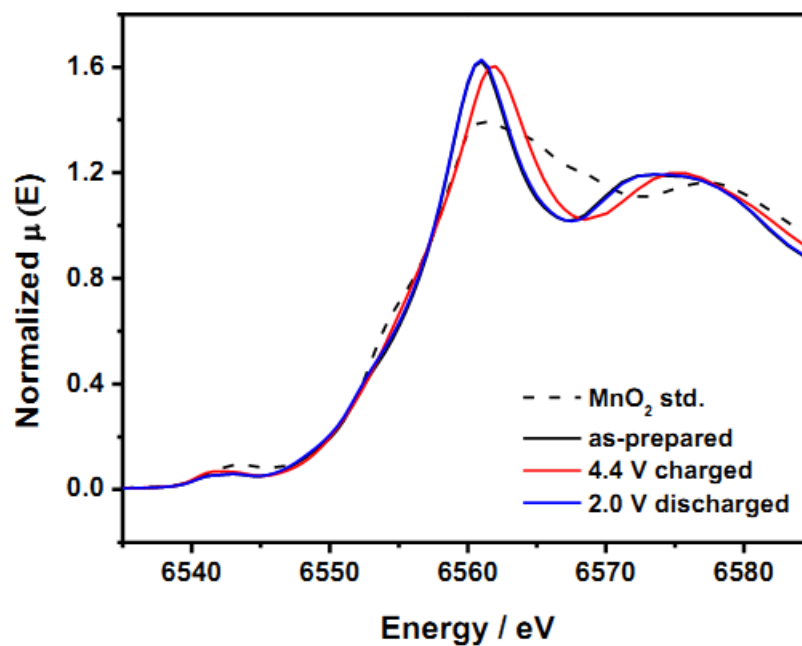


Figure 5.8 XAS analysis of the Ni K-edge for  $\text{Na}_{0.8}[\text{Li}_{0.12}\text{Ni}_{0.22}\text{Mn}_{0.66}]\text{O}_2$  charged to 4.1 V, 4.4 V and discharged to 2.0 V at the Ni K-edge (a) XANES region including a NiO standard and (b) the EXAFS spectra.

(a)



(b)

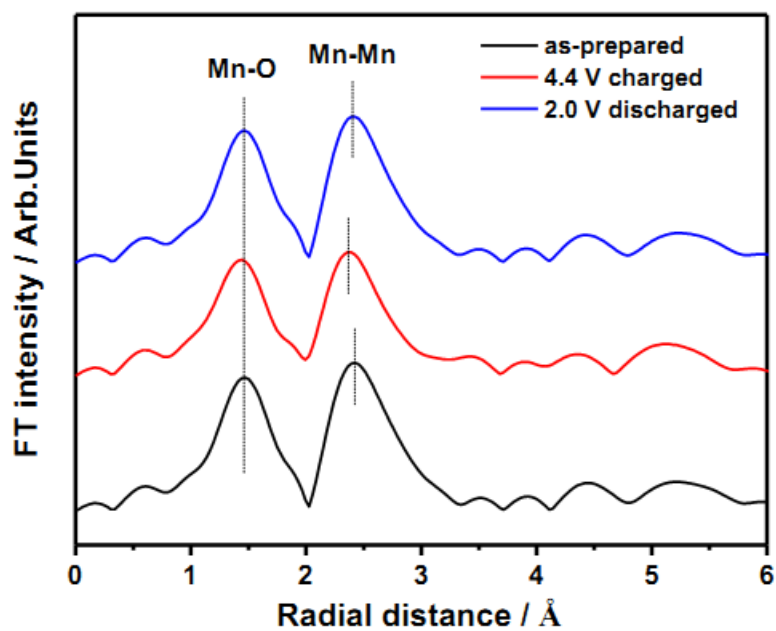


Figure 5.9 XAS analysis of the Mn K-edge for  $\text{Na}_{0.8}[\text{Li}_{0.12}\text{Ni}_{0.22}\text{Mn}_{0.66}]\text{O}_2$  charged to 4.4 V and discharged to 2.0 V at the Ni K-edge (a) XANES region including a  $\text{MnO}_2$  standard and (b) the EXAFS spectra.

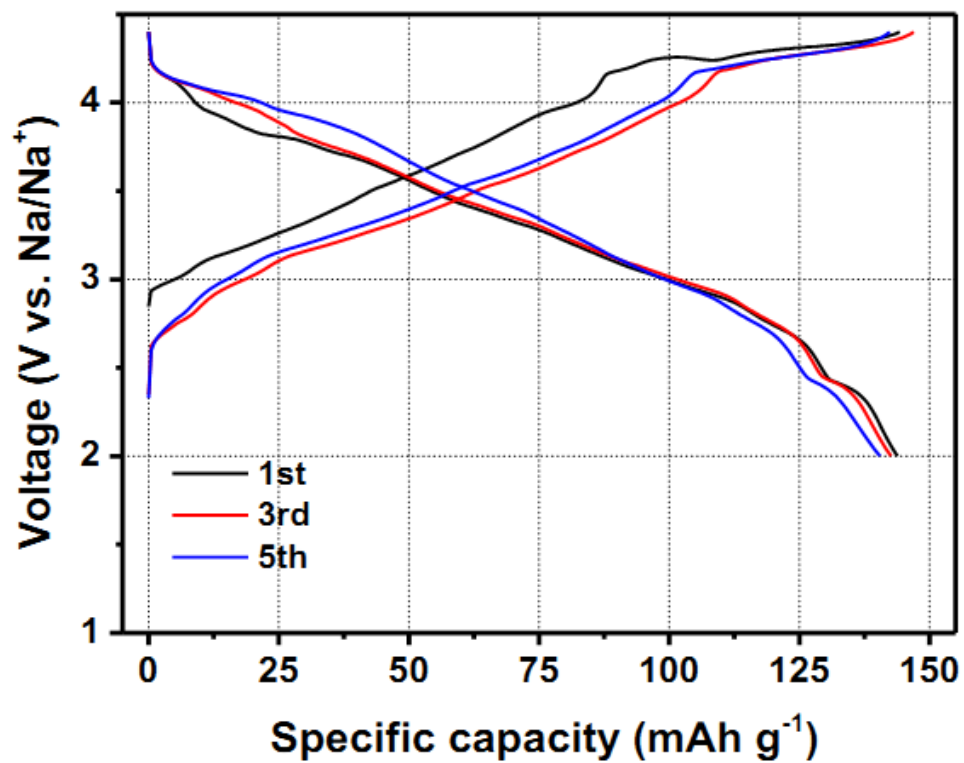


Figure 5.10 Electrochemical profiles for  $\text{Na}_{0.83}[\text{Li}_{0.07}\text{Ni}_{0.31}\text{Mn}_{0.62}]\text{O}_2$  in the voltage range of 2.0 ~ 4.4 V at the 1<sup>st</sup>, 3<sup>rd</sup>, and 5<sup>th</sup> cycle

Table 5.1 Parameters and reliability factors obtained by the Rietveld refinement of neutron diffraction for as-synthesized P2-Na<sub>0.8</sub>[Li<sub>0.12</sub>Ni<sub>0.22</sub>Mn<sub>0.66</sub>]O<sub>2</sub>

P2-Na <sub>0.8</sub> [Li <sub>0.12</sub> Ni <sub>0.22</sub> Mn <sub>0.66</sub> ]O <sub>2</sub> Space group: $P6_3$ (large hexagonal)					
Atom	Site	x	y	z	occ
Mn (1)	2a	0	0	0	0.935
Li (1)	2a	0	0	0	0.065
Ni	2b	1/3	2/3	0	0.660
Li (2)	2b	1/3	2/3	0	0.295
Mn (2)	2b	1/3	2/3	0	0.045
Mn (3)	2b	1/3	2/3	1/2	1.000
O (1)	6c	2/3	0	-0.418	3.000
O (2)	6c	0	0	0.395	3.000
Na <sub>f</sub> (1)	2a	0	0	1/4	0.300
Na <sub>e</sub> (2)	6c	1/3	0	1/4	1.500
Na <sub>f</sub> (3)	2b	1/3	2/3	1/4	0.300
Na <sub>f</sub> (4)	2b	2/3	1/3	1/4	0.300

$a = b = 4.996 \text{ \AA}$ ,  $c = 11.040 \text{ \AA}$   
 $R_{wp} = 8.6\%$ ,  $R_B = 10.1\%$

Table 5.2 Parameters and reliability factors obtained by the Rietveld refinement of X-ray diffraction for as-synthesized P2-Na<sub>0.8</sub>[Li<sub>0.12</sub>Ni<sub>0.22</sub>Mn<sub>0.66</sub>]O<sub>2</sub>

P2-Na <sub>0.8</sub> [Li <sub>0.12</sub> Ni <sub>0.22</sub> Mn <sub>0.66</sub> ]O <sub>2</sub> Space group: <i>P6<sub>3</sub>/mmc</i>					
Atom	Site	x	y	z	Occ.
Ni	2a	0	0	0	0.22
Mn	2a	0	0	0	0.66
Li	2a	0	0	0	0.12
O	4f	1/3	2/3	0.0784	2.00
Na <sub>f</sub>	2b	0	0	0.25	0.27
Na <sub>e</sub>	2d	1/3	2/3	0.75	0.45
$a = b = 2.885(2) \text{ \AA}, c = 11.016(2) \text{ \AA}$ $R_{wp} = 2.74\%, R_B = 8.01\%$					

Table 5.3 Distribution of Li-ions between TMO<sub>2</sub> and Na layer sites.

Site	Pristine	4.1 V charge	4.4 V charge	2 V discharge	After 5 cycles
TM layer	85	68	5	67	63
Na layer	15	4	38	5	8
Total	100	72	43	72	71

## Chapter 6. Breaking through the limitation of energy / power density for Na-ion battery cathodes

A new O3 -  $\text{Na}_{0.78}\text{Li}_{0.18}\text{Ni}_{0.25}\text{Mn}_{0.583}\text{O}_w$  is prepared as the cathode material for Na-ion batteries, delivering exceptionally high capacity and energy density. The single-slope profile and ex situ synchrotron XRD demonstrate that no phase transformation is happened, which is the first time to observe in O3-structured Na electrode materials.  $\text{Ni}^{2+} / \text{Ni}^{4+}$  is suggested to be the main redox center. More optimizations could be realized by tuning the combination and ratio of transition metals.

### 6.1. Introduction

Na-ion batteries have recently gained increasing recognition as intriguing candidates for next-generation large scale energy storage systems, owing to significant cost advantages stemming from the high natural abundance and broad distribution of Na resources. Although Na-ion battery materials are not comparable with their Li-ion counterparts which are one of the dominating energy technologies in this decade, there are studies suggesting that Na-ion systems should not be discarded.<sup>1</sup> In particular, Na-ion batteries operating at room temperature could be suitable for applications where specific volumetric and gravimetric energy density requirements are not as stringent as in EVs, namely in electrical grid storage of intermittent energy produced via renewable sources.<sup>2</sup> This would also contribute to a significant reduction of the costs connected to the use of renewable sources, which could then penetrate the energy market more easily and make Na-ion technology complementary to Li-ion batteries for stationary storage.<sup>3</sup>

For the past several years, a variety of novel materials have been explored as electrodes for Na-ion batteries. Since Na ion has a relatively larger ionic radius than that of the Li ion, materials with an open framework are required for facile Na ion insertion / extraction. Following this strategy, many breakthroughs in cathode materials have been achieved, such as layered and polyanion compounds.<sup>4</sup> Among most of the Na cathode compounds reported to date, the P2 and O3 structured Na oxides ( $\text{Na}_x\text{TMO}_2$ , TM = Transition Metal) have drawn significant attentions, since their relatively opened structures are able to accommodate large Na ions providing spacious diffusion path as well as the structural stability. The research on the structural properties of  $\text{Na}_x\text{TMO}_2$  was started in 70's by Delmas et al..<sup>5</sup> Recently, various P2- $\text{Na}_x\text{TMO}_2$ , and their binary or ternary derivatives, have been extensively investigated and some of them demonstrated superior electrochemical performances.<sup>6, 7</sup> However, compared with P2 structures, O3 structured materials have shown relatively small progress. For example,  $\text{NaCrO}_2$  was investigated by Komaba *et al.*, and showed 120 mAh/g of specific capacity near 2.9 V.<sup>8,9</sup> The O3- $\text{NaNi}_{0.5}\text{Mn}_{0.5}\text{O}_2$  electrodes delivered 105 mAh/g at 1C (240 mA/g) and 125 mAh/g at C/30 (8 mA/g) in the voltage range of 2.2 - 3.8 V and displayed 75% of the capacity after 50 cycles.<sup>9, 10</sup> The Fe-substituted O3- $\text{Na}[\text{Ni}_{1/3}\text{Fe}_{1/3}\text{Mn}_{1/3}]\text{O}_2$  exhibited the specific capacity of 100 mAh/g with average operating voltage at 2.75 V.<sup>11</sup> The isostructural compound,  $\text{Na}[\text{Ni}_{1/3}\text{Mn}_{1/3}\text{Co}_{1/3}]\text{O}_2$ , showed reversible intercalation of 0.5 Na-ions leading to the specific capacity of 120 mAh/g in the voltage range of 2.0 - 3.75 V.<sup>12</sup> These relatively low capacity and limited cycling retention are presumably due to the fact that most of these materials undergo multiple phase transformations from O3 to O'3, P3, P'3 and then P''3 consecutively.<sup>13</sup> These transformations could be one of the major

problems that limit the practical uses of Na-ion batteries since it deteriorates the cycle life and rate capabilities. Herein, to overcome this issue, “Na-excess” O3 compound is prepared through Li-Na ion exchange, inspired by the idea in Li-ion batteries that Li-excess O3 compound has been demonstrated single slope voltage profile with significant improvement in capacity and cycling retention for Li layered electrodes.<sup>14</sup>

## 6.2. Experimental

A coprecipitation followed by two steps calcination was used for the synthesis of the O3 type Li-excess layered oxides.<sup>20</sup> Transition metal (TM) nitrates,  $\text{Ni}(\text{NO}_3)_2 \cdot 6\text{H}_2\text{O}$  (ARCROS, 99%), and  $\text{Mn}(\text{NO}_3)_2 \cdot 4\text{H}_2\text{O}$  (Alfa Aesar, 98%) were dissolved into deionized water then titrated into  $\text{LiOH} \cdot \text{H}_2\text{O}$  (Fisher) solution. The coprecipitated TM hydroxides were then filtered using vacuum filtration and washed three times with deionized water. The collected TM hydroxides were dried in an oven at 180°C for 10 h in air. The dried TM precursors were then mixed with a stoichiometric amount of  $\text{LiOH} \cdot \text{H}_2\text{O}$  (Fisher) corresponding to the amount of  $\text{TM}(\text{OH})_2$  from the coprecipitation step. This mixture was ground for 30 min to ensure adequate mixing and then placed into a furnace at 480°C for 12 h. The precalcinated powders were then calcinated at 900 °C for 12 h in air.

Cathodes of as-prepared O3 type Li-excess layered oxides were prepared by mixing the active material with 10 wt % Super P carbon (TIMCAL) and 10 wt % poly(vinylidene fluoride) (PVDF) in N-methylpyrrolidone (NMP) solution. The slurry was cast onto an Al foil using a doctor blade and dried in a vacuum oven overnight at 80 °C. The electrode discs were punched and dried again at 80 °C for 6 h before storing

them in an argon filled glovebox ( $\text{H}_2\text{O}$  level < 1 ppm). Then, the O3 type Na-excess layered oxides was prepared by ion-exchange. For example, the  $\text{Li}_{1.133}\text{Ni}_{0.3}\text{Mn}_{0.567}\text{O}_w$  electrode which contains more lithium ( $y > 0.6$ ) was charged with cut off voltage at 4.8 V (vs.Li metal, using 1M  $\text{LiPF}_6$ , 1:1 EC:DMC) and discharged with cut off voltage 1.5 V (vs.Na metal, using 1M  $\text{NaPF}_6$ , 1:1 EC:DEC), thus O3 type  $\text{Na}_{0.8}\text{Li}_{0.14}\text{Ni}_{0.3}\text{Mn}_{0.567}\text{O}_w$  electrode which contains more sodium ( $x > 0.6$ ) electrode was obtained.

Electrochemical properties were measured on an Arbin battery cycler in galvanostatic mode between 4.2 and 1.5 V. The 2016 coin cells were prepared in the Argon filled glovebox ( $\text{H}_2\text{O} < 0.1$  ppm) using sodium metal ribbon as an anode and a 1 M  $\text{NaPF}_6$  in a 1:1 ethylene carbonate/diethyl carbonate (EC:DEC) electrolyte solution. Glass fiber D separators were used as the separator. For full cell: Electrochemical properties were measured on an Arbin battery cycler in galvanostatic mode between 4.2 and 1 V. The 2032 coin cells were prepared in the Argon filled glovebox ( $\text{H}_2\text{O} < 0.1$  ppm) using  $\text{SnS}_2/\text{rGO}$  as an anode and a 1 M  $\text{NaPF}_6$  in a 1:1 ethylene carbonate/diethyl carbonate (EC:DEC) electrolyte solution. Glass fiber D separators were used as the separator. The cycled samples were recovered by disassembling cycled batteries in the same argon-filled glovebox. The cathode was washed with DMC 3 times and then allowed to dry in argon atmosphere overnight.

XAS measurements were carried out at the PNC-XSD bending magnet beamline (20-BM) of the Advanced Photon Source. Measurements at the Ni and Mn K- edge were performed in the transmission mode at room temperature using gas ionization chambers to monitor the incident and transmitted X-ray intensities. A third ionization chamber was used in conjunction with Mn / Ni-foil standards to provide internal calibration for the

alignment of the edge position. Monochromatic X-rays were obtained using a fixed-exit Si (111) double crystal monochromator. Energy calibration was carried out using the first derivative of the spectra of the Ni and Mn metal foils. The data were analyzed and refined using the Iffeffit<sup>21</sup> and Horae<sup>22</sup> packages.

The samples for XRD were obtained by disassembling cycled batteries in an argon-filled glovebox. The cathode was washed by battery grade dimethyl carbonate (DMC) 3 times and dried. The cathode film was sliced into thin pieces and mounted in the hermitically sealed capillary tubes for ex-situ XRD. Powder diffractions of all samples were taken using synchrotron XRD at the Advanced Photon Source (APS) at Argonne National Laboratory (ANL) on beamline 11-BM ( $\lambda = 0.459 \text{ \AA}$ ). The beamline uses a sagittal focused X-ray beam with a high precision diffractometer circle and perfect Si(111) crystal analyzer detection for high sensitivity and resolution. XRD patterns were analyzed by Rietveld refinement method using FullProf software.<sup>23</sup>

### 6.3 Results and Discussion

The  $\text{Li}_{1.133}\text{Ni}_{0.3}\text{Mn}_{0.567}\text{O}_2$  was synthesized by heating a mixture of  $\text{LiOH}\cdot\text{H}_2\text{O}$  and  $\text{Ni}_{0.346}\text{Mn}_{0.654}(\text{OH})_2$ . The obtained  $\text{Li}_{1.133}\text{Ni}_{0.3}\text{Mn}_{0.567}\text{O}_2$  was firstly charged in the Li half cell to extract Li ions and then discharged in the Na half cell to prepare  $\text{O}_3 - \text{Na}_{0.719}\text{Li}_{0.073}\text{Ni}_{0.3}\text{Mn}_{0.567}\text{O}_w$ . (Figure 6.1) To achieve higher capacity, the ratio among Li, Ni and Mn was further adjusted and the composition,  $\text{Li}_{1.167}\text{Ni}_{0.25}\text{Mn}_{0.583}\text{O}_2$  was finally chosen, which improved the initial Na-insertion capacity from 220 mAh/g to 240 mAh/g. Figure 6.2(a) illustrates the electrochemical profiles for the initial “delithiation” (Li-extraction) and “sodiation” (Na-extraction) processes for  $\text{Li}_{1.167}\text{Ni}_{0.25}\text{Mn}_{0.583}\text{O}_2$ . The

stoichiometry for the ion-exchanged material is  $\text{Na}_{0.78}\text{Li}_{0.18}\text{Ni}_{0.25}\text{Mn}_{0.583}\text{O}_w$ , as determined by the electrochemical capacity and energy-dispersive X-ray spectroscopy. The as-prepared  $\text{Na}_{0.78}\text{Li}_{0.18}\text{Ni}_{0.25}\text{Mn}_{0.583}\text{O}_w$  has particle size less than 500 nm, retaining same morphology with its parent material,  $\text{Li}_{1.167}\text{Ni}_{0.25}\text{Mn}_{0.583}\text{O}_2$ . (Figure 6.3) The cycling performance is tested between 1.5 and 4.2 V with current density at 125 mA/g. After 30 cycles, around 190 mAh/g capacity is well maintained as shown in Figure 6.2(b). With 1.25 A/g current, the reversible capacity is still as high as 160 mAh/g, suggesting its high-power capability. (Figure 6.4) Figure 6.2(c) compares capacity and energy density for most of the recent cathodes in Na-ion batteries (highest reversible value is selected.) The  $\text{Na}_{0.78}\text{Li}_{0.18}\text{Ni}_{0.25}\text{Mn}_{0.583}\text{O}_w$  exhibits not only the highest capacity but also the highest energy density: 675 Wh/kg energy density is delivered by this material during discharge, which is even higher than  $\text{LiFePO}_4$  (560 Wh/kg) and  $\text{LiCoO}_2$  (560 Wh/kg) in Li-ion batteries.<sup>16</sup> More interestingly, as displayed in the inset of Figure 6.2(b), no voltage steps are seen in the electrochemical profiles upon cycling. It indicates that no phase transformations happen for this O3 material even after all the Na ions are extracted. Besides, the voltage depression problem which is usually observed in its parent material,  $\text{Li}_{1.167}\text{Ni}_{0.25}\text{Mn}_{0.583}\text{O}_2$  in Li-ion batteries,<sup>17</sup> is reduced to some degree in this ion-exchanged product in Na-ion batteries.

The synchrotron X-ray Diffraction (SXR) was conducted at selected states to detect the structural change. (Figure 6.5(a)) The refined lattice parameters were summarized at Table 6.1. As shown with the black line in Figure 6.5(a), the as-synthesized material,  $\text{Li}_{1.167}\text{Ni}_{0.25}\text{Mn}_{0.583}\text{O}_2$ , is well crystallized and can be indexed as R-3m space group. The diffraction pattern illustrates typical Li-excess features, which have

been discussed by our previous work.<sup>17</sup> After initial delithiation (red line in Figure 6.5(a)), the *c* lattice is slightly increased (Table 6.1) due to less screening effect between neighbored oxygen layers when Li ions are mostly removed from the host.<sup>18</sup> Upon initial sodiation (green line in Figure 6.5(a)), the whole spectrum is significantly shifted to lower angle, such as (003) and (110) peak. The shift is resulted from the overall lattice expansion, as the inserted Na ions have much large ionic size than Li ions. Peak broadening is observed, which is probably ascribed to the stacking faults introduced during initial sodiation. More work is undergoing to comprehensively investigate this process. It should be noted that although the diffraction peaks are moved systematically, all the peaks still belong to R-3m space group, in other words, O3 phase (Figure 6.5(b)), proving that there is no change in the host structure during ion-exchange process. To further monitor the electrode structural change upon cycling in Na batteries, two ex-situ samples were characterized. When the electrode is charged to 4.2 V (pink line in Figure 6.5(a)), the material is still maintained at O3 structure though the majority of Na ions are removed as suggested by charging capacity. This is the first time that phase transformation is prohibited for O3 cathode materials in Na-ion batteries even after most of Na ions leave the host. Comparing with the material after initial sodiation, it is interesting to notice the (003) peak is moved to higher angle, indicating that *c* lattice is reduced at this state. All the peaks positions are close to those of the material after initial delithiation. Since it has been reported that in Li-excess materials, Li in tetrahedral sites are created after first charge,<sup>17, 18</sup> it is hypothesized that the tetrahedral Li would form similarly in our initial delithiation process as shown in Figure 6.5(c). These tetrahedral Li ions play a critical role in stabilizing the O3 phase at subsequent cycles by locking the

neighbored layer shifting. When the electrode is discharged to 1.5 V (blue line in Figure 6.5(a)), the spectrum is back to the similar positions with the material after initial sodiation, suggesting that the Na ions are re-inserted back reversibility. And most importantly, the O3 phase is still well maintained.

In order to investigate the charge compensation mechanism during Na-ions extraction and insertion, X-ray absorption spectroscopy (XAS) measurements were conducted with Ni and Mn K-edges at different state of charge. Normalized Ni and Mn K-edge X-ray absorption near edge structure (XANES) spectra are shown in Figure 6.6(a) and (b), respectively. For the standards, Ni K-edge spectra of divalent Ni-ion (NiO) and Mn K-edge spectra of tetravalent Mn-ion (MnO<sub>2</sub>) are included. It is evident that as-synthesized Li<sub>1.167</sub>Ni<sub>0.25</sub>Mn<sub>0.583</sub>O<sub>2</sub> compound predominantly consists of Ni<sup>2+</sup> and Mn<sup>4+</sup>. Obvious changes are shown in the Ni XANES spectra upon the initial delithiation, sodiation, and followed charge and discharge process. The Ni K-edge absorption energy of initially delithiated electrode shifts to the higher energy region compared to that of as-synthesized state. The amount of absorption energy shift is ~3 eV, suggesting that oxidation state of Ni after initial delithiation is close to Ni<sup>4+</sup>.<sup>17</sup> After initial sodiation, the oxidation state of Ni ions returns back to divalent. The similar edge shift and recover are seen again between 4.2 V and 1.5 V ex-situ electrode samples suggesting that the Ni<sup>2+</sup>/Ni<sup>4+</sup> redox reaction is completely reversible in Na-ion batteries. In contrast to the Ni XANES, Mn K-edge XANES shows that Mn ions mainly stay at tetravalent state and no dramatic changes are occurred in the valence upon the charge and discharge. Based on the Ni and Mn XANES, it is proved that Ni is the only electrochemically active species and Mn supports the structural stability in the absence of Jahn-Teller active Mn<sup>3+</sup>. More

details on local structural change are revealed by the extended X-ray absorption fine structure (EXAFS) spectra. (Figure 6.6(c) and (d)) Ni EXAFS clearly shows that interatomic distances of Ni-O and Ni-TM are shortened after the initial delithiation and after the charge in Na-ion batteries, indicating that the oxidation of Ni ions. After initial sodiation, the interatomic distances are systematically larger than the as-synthesized state, resulted from lattice expansion when Na ions are inserted. However, Mn EXAFS does not show any significant changes in the Mn-O interatomic distance, although the second shell corresponding to Mn-TM distance is varied with different voltages. This is ascribed to the changes in the Ni oxidation states, which accordingly affect the distance among neighbored Mn-Ni.

To evaluate the practical application of  $\text{Na}_{0.78}\text{Li}_{0.18}\text{Ni}_{0.25}\text{Mn}_{0.583}\text{O}_2$ , the full cell was fabricated with  $\text{Na}_{0.78}\text{Li}_{0.18}\text{Ni}_{0.25}\text{Mn}_{0.583}\text{O}_w$  as cathode and  $\text{SnS}_2$  / rGO as anode. (Figure 6.7(a)) The anode is reported by our previous work before.<sup>19</sup> In our full cell configuration, both cathode material and anode material are casted on Al current collector, which will further reduce the cost and weight of Na ion battery. By charging, Na ions are extracted from the cathode and inserted into the anode. During discharge, Na ions are transferred reversely. By this process, the energy storage and released reversibly. Figure 6.7(b) represents voltage profiles of the full cell which shows a discharge capacity of  $\sim 210$  mAh / g (capacity based on cathode weight). The overall capacity of Na full cell using our advanced cathode and anode is able to achieve 175 mAh / g (considering the weight of cathode and anode materials). The operation discharge voltage is 2.5 V. As a result, the total energy density for this Na full cell is as high as 430 Wh / kg, which is to our best knowledge the highest energy so far reported for Na full cells. Furthermore, the

capacity is well maintained for this Na full cell. As shown in Figure 6.7(c), after 50 cycles, more than 165 mAh/g is delivered reversibly.

In fact, the ion-exchanged electrode performance could be further adjusted by mixing with other TM, such as Co. As shown in Figure 6.8(a), if the parent Li compound is designed with Co in the stoichiometry as  $\text{Li}_{1.167}\text{Ni}_{0.166}\text{Mn}_{0.5}\text{Co}_{0.166}\text{O}_2$ , the discharged capacity is further increased to 245 mAh/g. In addition, direct synthesis could be realized as seen in Figure 6.8(b). The directly obtained material,  $\text{NaLi}_{0.067}\text{Co}_{0.267}\text{Ni}_{0.267}\text{Mn}_{0.4}\text{O}_2$ , has demonstrated pure O3 phase, and its electrochemical properties are under development now.

#### 6.4 Conclusion

In conclusion, a new O3 -  $\text{Na}_{0.78}\text{Li}_{0.18}\text{Ni}_{0.25}\text{Mn}_{0.583}\text{O}_w$  is obtained by the electrochemical Na-Li ion exchange process of  $\text{Li}_{1.167}\text{Ni}_{0.25}\text{Mn}_{0.583}\text{O}_2$ . The new material shows exceptionally high discharge capacity of 240 mAh/g in the voltage range of 1.5-4.5 V, thus the total energy density at the materials level reaches 675 Wh/kg. It is the highest capacity as well as highest energy density so far among all the reported cathodes in Na-ion batteries. When cycled between 1.5-4.2 V, the discharge capacity is well maintained around 190 mAh/g after 30 cycles. The O3 phase is kept through ion-exchange and cycling process, as confirmed by SXRD. The stabilized O3 phase could be related to the tetrahedral Li formed upon initial lithiation, and breaks through the critical limitation for most O3 compounds. XAS results show that  $\text{Ni}^{2+}/\text{Ni}^{4+}$  is the main active redox couple during cycling while Mn ions basically stay at tetravalent state. The Na full cell utilizing  $\text{Na}_{0.78}\text{Li}_{0.18}\text{Ni}_{0.25}\text{Mn}_{0.583}\text{O}_w$  as cathode delivers 430 Wh / kg energy density.

Future improvement could be realized through further tuning the combination and ratio among TMs, and making the material by direct synthesis is under development, which would be reported very soon.

Chapter 6, in full, is currently being prepared for publication of the material “Breaking through the limitation of O<sub>3</sub> compounds as promising cathode for Na-ion batteries”. The dissertation author was the primary investigator and author of this paper. All the SXRD and XAS were collected and analyzed by author, and the paper is written by the author.

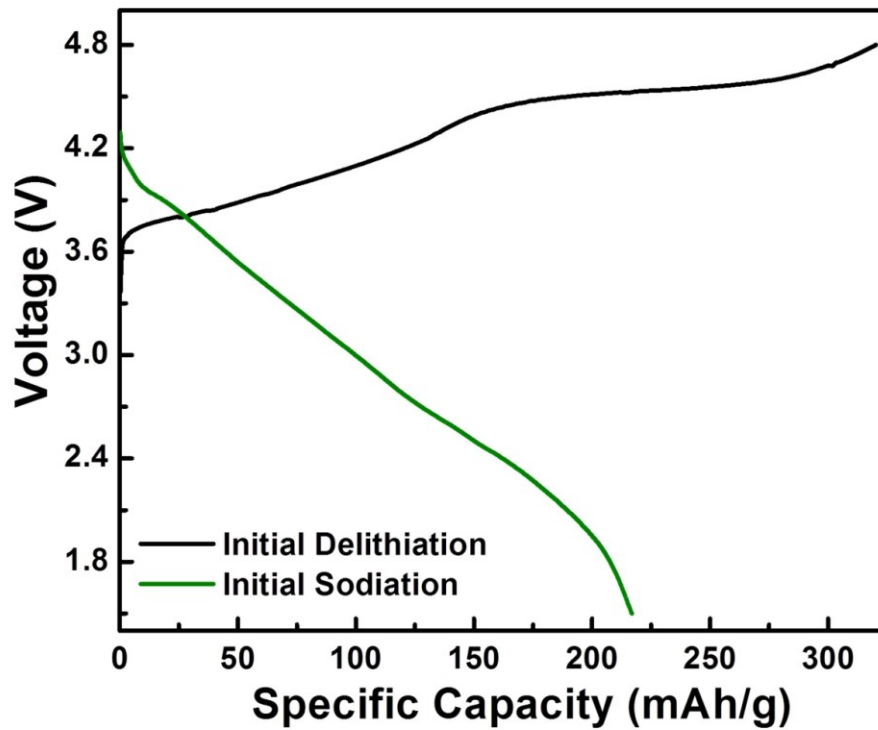


Figure 6.1 Electrochemical profile for  $\text{Li}_{1.133}\text{Ni}_{0.3}\text{Mn}_{0.567}\text{O}_2$  during initial delithiation and initial sodiation.

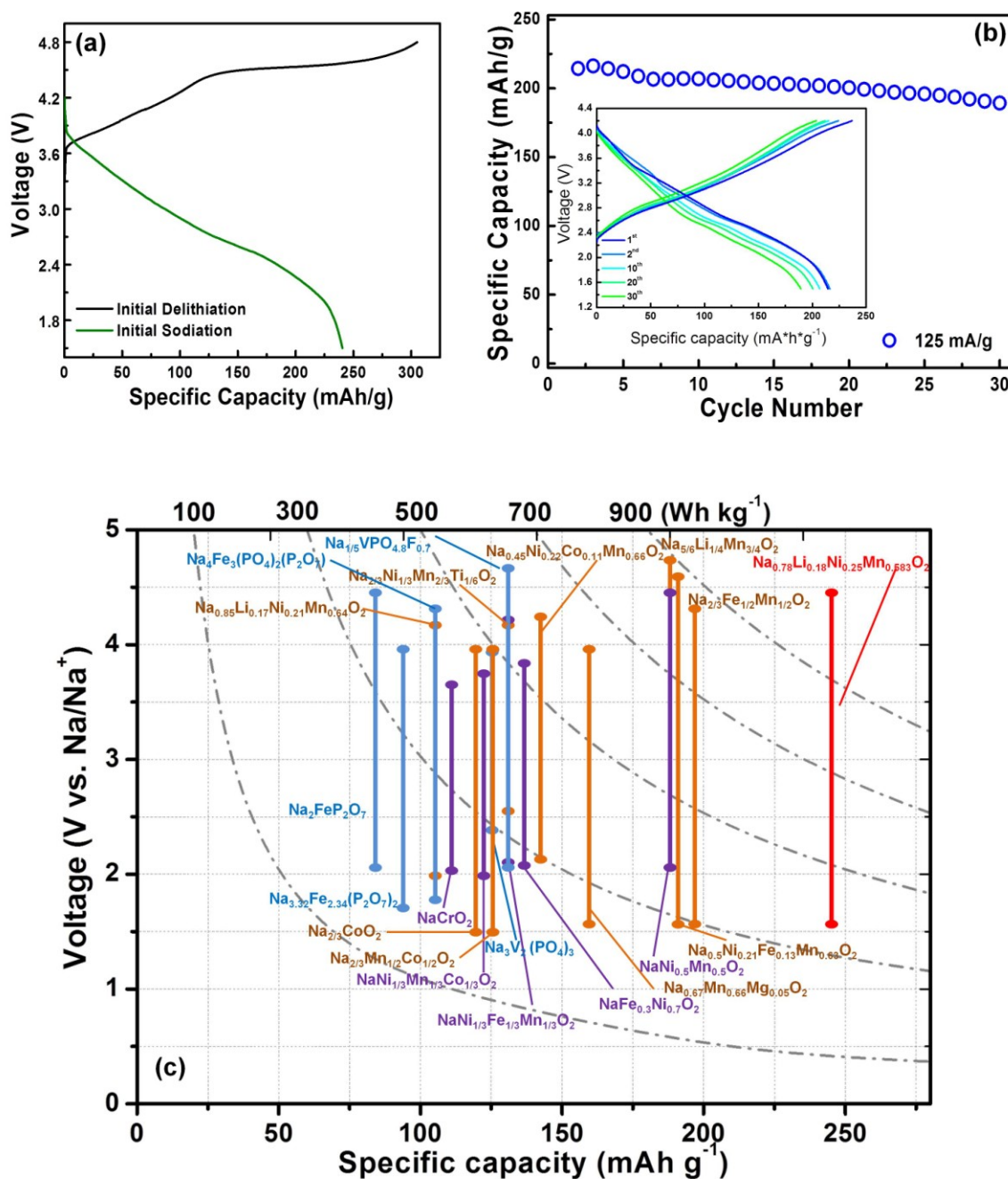


Figure 6.2 (a) Electrochemical profiles of initial delithiation and initial sodiation. (b) Electrochemical profile of  $\text{Na}_{0.719}\text{Li}_{0.073}\text{Ni}_{0.3}\text{Mn}_{0.567}\text{O}_2$  during the 1<sup>st</sup>, 2<sup>nd</sup>, 10<sup>th</sup>, 20<sup>th</sup>, 30<sup>th</sup> cycles in Na-ion batteries. (c) Comparison of reversible capacities for the intercalation-based Na cathodes.<sup>32, 40, 55, 72, 174, 201, 208-220</sup>

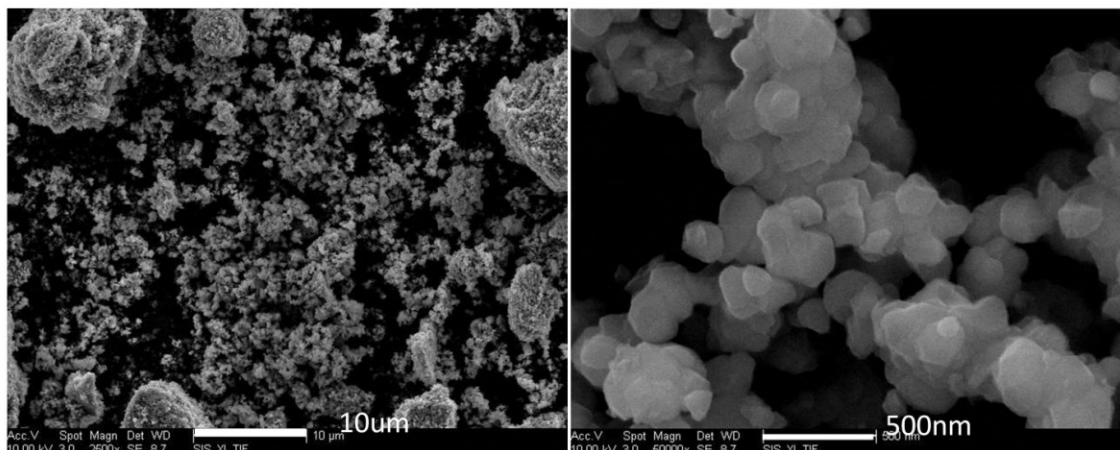


Figure 6.3 SEM images for as-synthesized  $\text{Na}_{0.78}\text{Li}_{0.18}\text{Ni}_{0.25}\text{Mn}_{0.583}\text{O}_2$ .

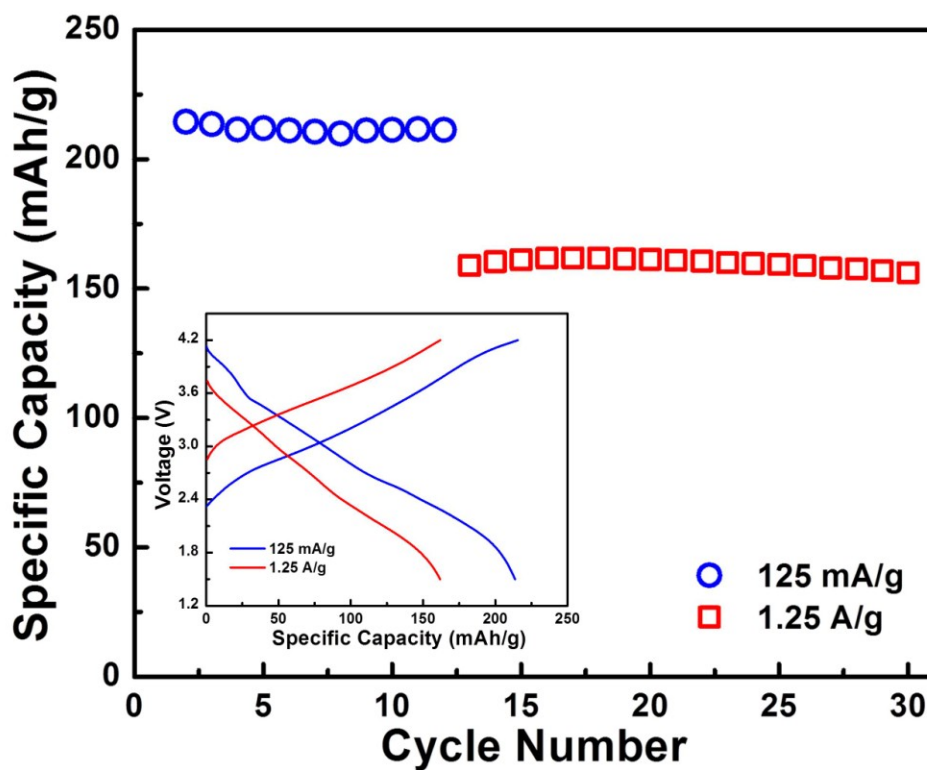


Figure 6.4 Rate performance of  $\text{Na}_{0.78}\text{Li}_{0.18}\text{Ni}_{0.25}\text{Mn}_{0.583}\text{O}_2$ .

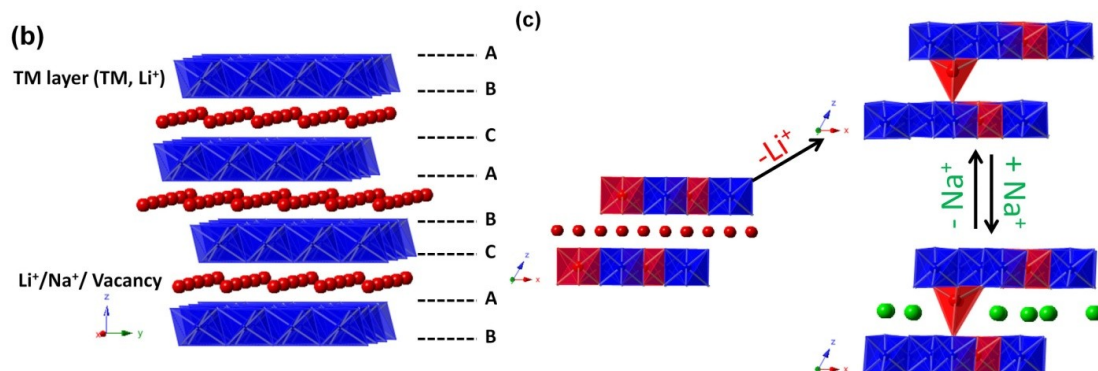
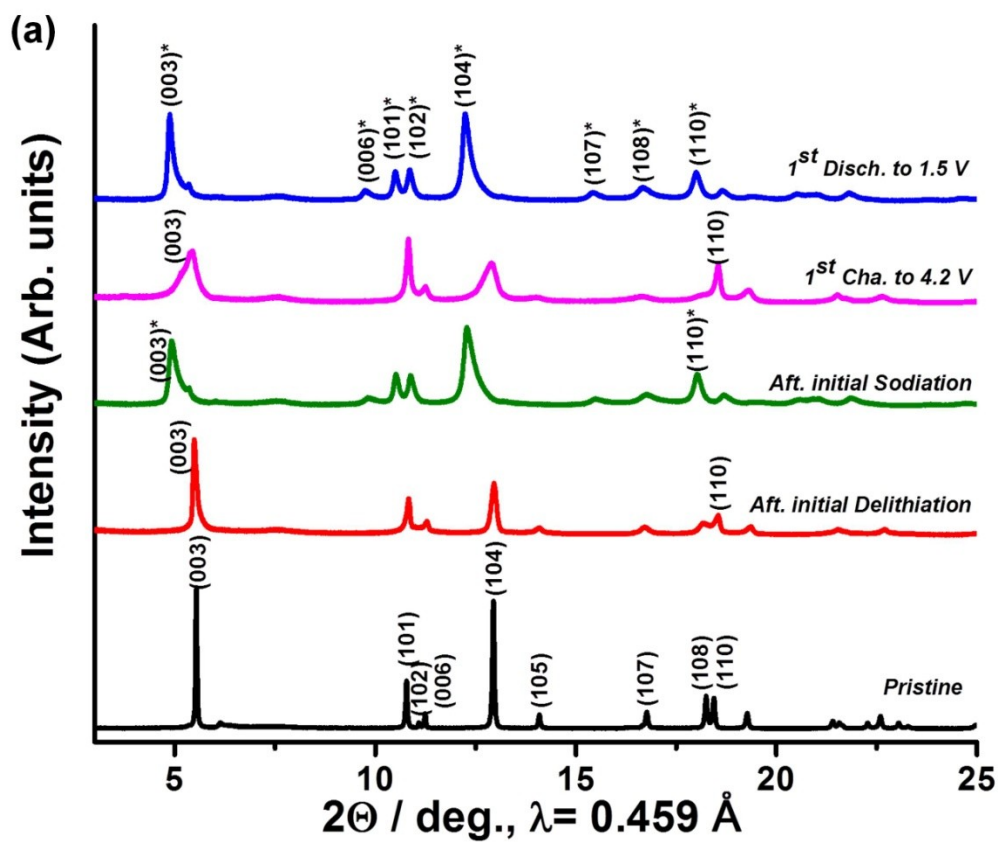


Figure 6.5 (a) Ex situ SXR D for  $\text{Li}_{1.167}\text{Ni}_{0.25}\text{Mn}_{0.583}\text{O}_2$  and  $\text{Na}_{0.78}\text{Li}_{0.18}\text{Ni}_{0.25}\text{Mn}_{0.583}\text{O}_2$  at different states. (b) Schematic of O3 structure. (c) Schematic of the proposed mechanism.

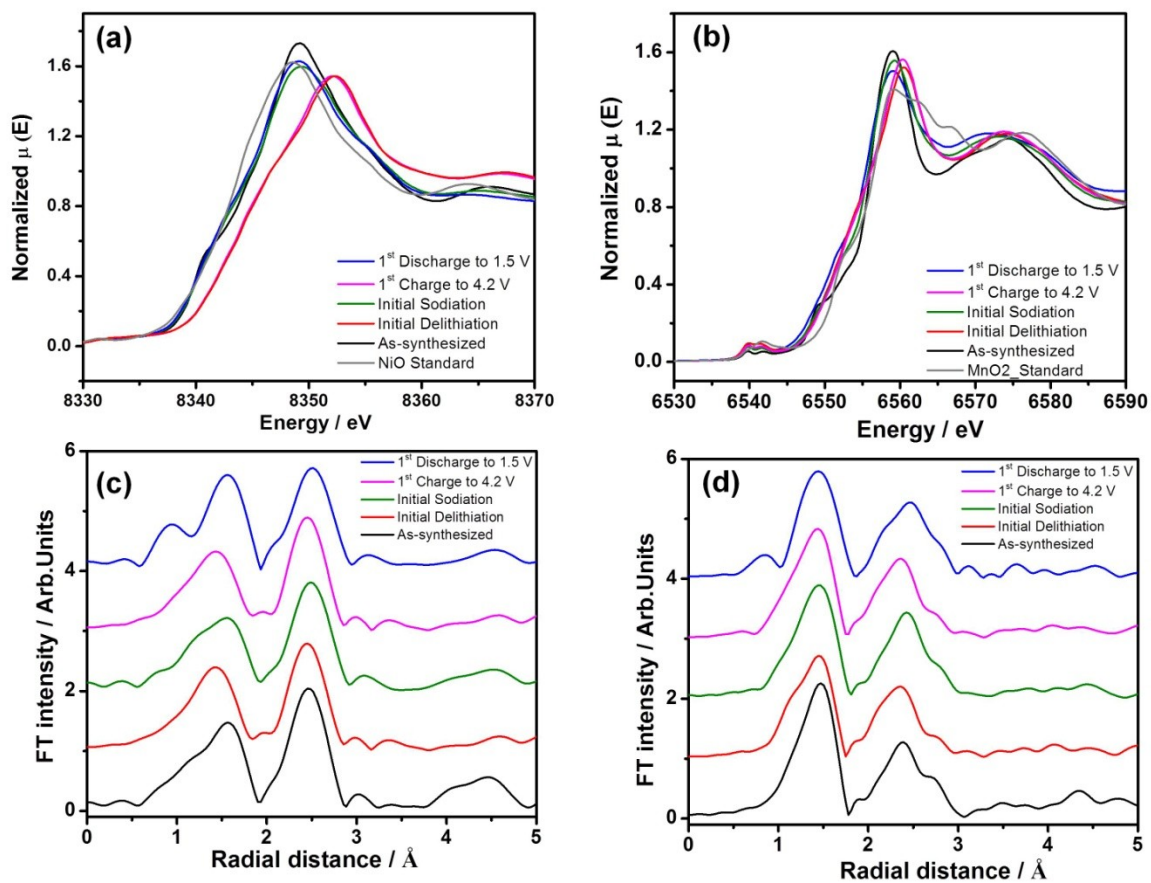


Figure 6.6 XAS analysis for  $\text{Li}_{1.167}\text{Ni}_{0.25}\text{Mn}_{0.583}\text{O}_2$  and  $\text{Na}_{0.78}\text{Li}_{0.18}\text{Ni}_{0.25}\text{Mn}_{0.583}\text{O}_2$  at different states. XANES spectra for (a) Ni and (b) Mn K-edge respectively. EXAFS spectra for (a) Ni and (b) Mn K-edge respectively.

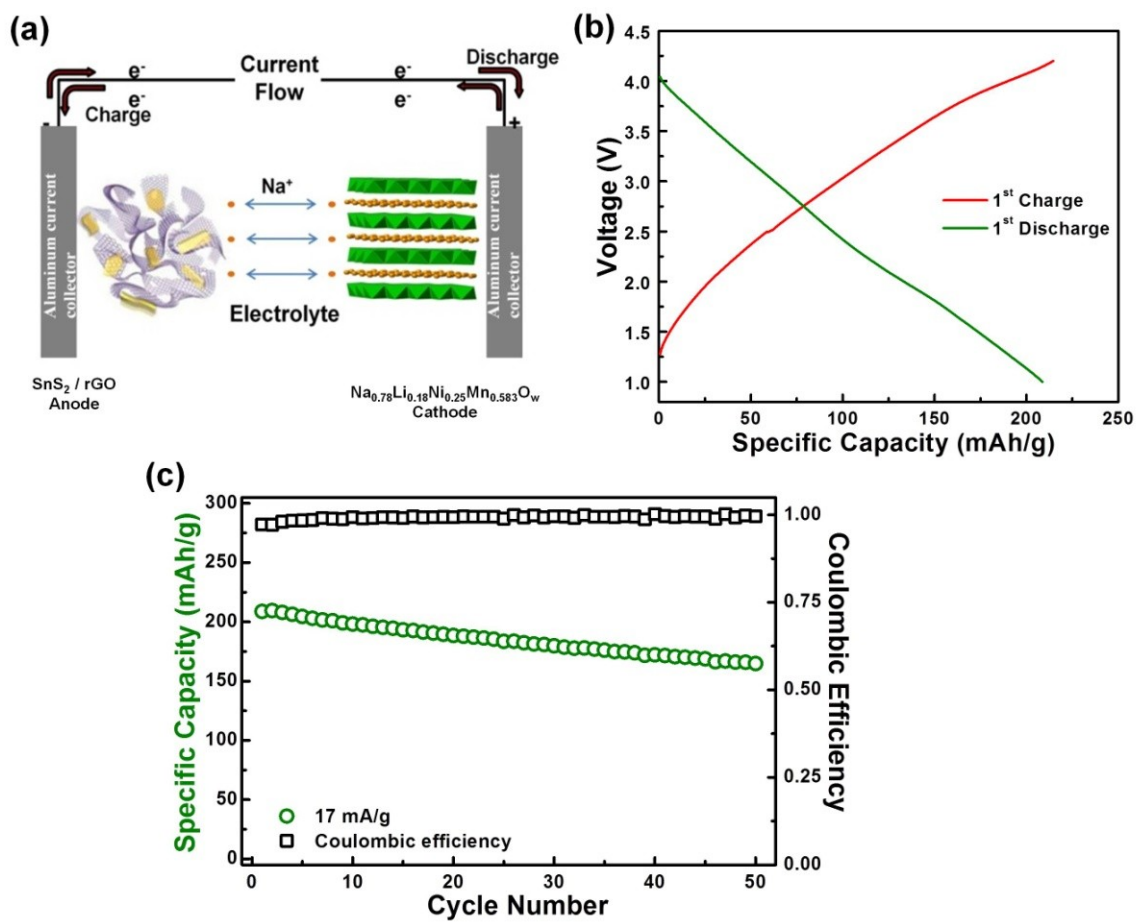


Figure 6.7 (a) Schematic of Na full. (b) The electrochemical profile at 1<sup>st</sup> cycle and (c) cycling performance for Na full cell.

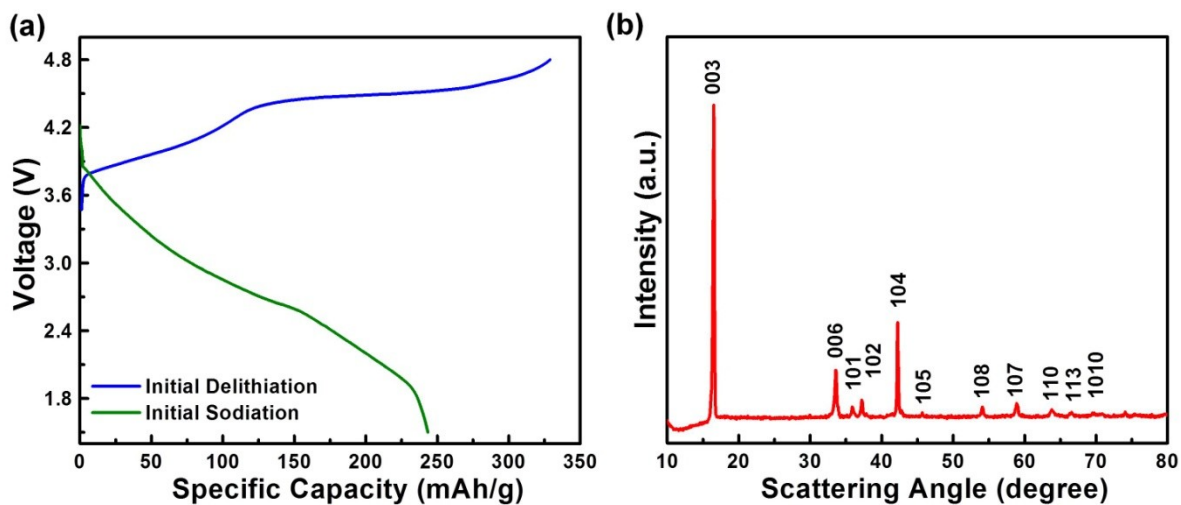


Figure 6.8 (a) The electrochemical profile for  $\text{Li}_{1.167}\text{Ni}_{0.166}\text{Mn}_{0.5}\text{Co}_{0.166}\text{O}_2$  during initial delithiation and initial sodiation. (b) XRD for as-synthesized  $\text{NaLi}_{0.067}\text{Co}_{0.267}\text{Ni}_{0.267}\text{Mn}_{0.4}\text{O}_2$ .

Table 6.1. Refined lattice parameters for  $\text{Li}_{1.167}\text{Ni}_{0.25}\text{Mn}_{0.583}\text{O}_2$  and  $\text{Na}_{0.78}\text{Li}_{0.18}\text{Ni}_{0.25}\text{Mn}_{0.583}\text{O}_w$  at different states.

	a (Å)	c (Å)
1 <sup>st</sup> discharge	2.9343	16.2007
1 <sup>st</sup> charge	2.8484	14.4783
Initial Sodiation	2.9316	16.0590
Initial Delithiation	2.8485	14.3886
As-synthesized	2.8643	14.2588

## **Chapter 7. Understanding $\text{Na}_2\text{Ti}_3\text{O}_7$ as an ultra-low voltage anode material for Na-ion battery**

A comprehensive understanding of  $\text{Na}_2\text{Ti}_3\text{O}_7$  as an anode for Na-ion batteries is reported. The electrochemical performance is significantly enhanced with carbon coating, as a result of increased electronic conductivity and reduced solid electrolyte interphase formation.  $\text{Ti}^{4+}$  reduction upon discharge is demonstrated by in-situ XAS. The self-relaxation behaviour of fully intercalated phase is revealed, for the first time, due to its structural instability

### **7.1. Introduction**

Na-ion batteries have recently gained increased recognition as intriguing candidates for next-generation large scale energy storage systems, stemming from the natural abundance and broad distribution of Na resources. Although the energy density of Na-ion battery is not as high as that of Li-ion battery, which is one of the most dominating energy technologies in this decade, there are studies suggesting that Na-ion systems should not be discarded.<sup>157, 198</sup> In particular, Na-ion batteries operating at room temperature could be suitable for applications where specific volumetric and gravimetric energy density requirements are not as stringent as in EVs, namely in electrical grid storage of intermittent energy produced via renewable sources.<sup>3</sup> This would also contribute to a significant reduction in the costs connected to the use of renewable sources, which could then penetrate the energy market more easily and make Na-ion technology complementary to Li-ion batteries for stationary storage.<sup>1, 89, 199</sup>

For the past several years, a variety of novel materials have been explored as electrode materials for Na-ion batteries. Since Na ion has a relatively larger ionic radius than Li ion, materials with an open framework are preferred for facile Na ion insertion / extraction. Following this strategy, many breakthroughs in cathode materials have been achieved, such as layered and polyanion compounds.<sup>20, 200</sup> However, the development of suitable anode materials for Na-ion batteries remains a considerable challenge.<sup>52, 77</sup> Graphite cannot be used as anode, since it is unable to intercalate Na ion reversibly.<sup>78, 79</sup> Metallic Na is also ruled out, because it forms dendrites easily and has an even lower melting point than Li. Hard carbons is shown to insert and de-insert Na ions, delivering capacities about 200–300 mAh g<sup>-1</sup>.<sup>79-81</sup> However, the reversibility for carbonaceous materials still requires further improvement.<sup>82, 83</sup> Na-alloys are proposed as possible alternatives, as they can potentially provide higher specific capacities.<sup>84-88</sup> These alloys, however, suffer from large volume changes upon uptake / removal of Na, in analogy to Li-alloys.<sup>89</sup> Another emerging class of materials is transition metal oxides. For example, NaVO<sub>2</sub> is shown to yield a reversible capacity (e.g. <130 mAh g<sup>-1</sup>) at C/100 current rate, but its operating voltage is at 1.5 V vs. Na<sup>+</sup>/Na, leading to a low energy density.<sup>90</sup> Ti-based oxides are suggested to be an attractive alternative, considering that Li<sub>4</sub>Ti<sub>5</sub>O<sub>12</sub> is one of the few commercialized anode materials in Li-ion battery.<sup>91, 92</sup> Several different sodium titanates have been explored as anodes for Na-ion battery.<sup>93-97</sup> Among them, a study by Palacín et. al. demonstrated that the layered oxide Na<sub>2</sub>Ti<sub>3</sub>O<sub>7</sub> could reversibly exchange Na ions with the lowest voltage ever reported for an oxide insertion electrode.<sup>96</sup> The ultra low voltage and intrinsic high reversibility of this material make it a strong anode candidate for Na-ion battery. Very recently, the same group identified the fully

intercalated phase,  $\text{Na}_4\text{Ti}_3\text{O}_7$ , and provided additional insight on the low intercalation potential of this material, using DFT calculations.<sup>97</sup> However, more work is still required to closely connect the fundamental properties with the battery performance and to systematically evaluate whether it can be a viable anode for Na-ion battery. Herein, we report a comprehensive study in order to unveil the underlying relationship between its intercalation mechanism and practical battery performance for  $\text{Na}_2\text{Ti}_3\text{O}_7$  anode.

## 7.2. Experimental

Pure  $\text{Na}_2\text{Ti}_3\text{O}_7$  was prepared from anatase  $\text{TiO}_2$  (>99.8%, Aldrich) and anhydrous  $\text{Na}_2\text{CO}_3$  (>99.995%, Aldrich) mixtures with 10% excess of the latter based on stoichiometric amounts. These mixtures were milled and calcinated at 800°C for 40h. The carbon coating was applied according to previous report.<sup>221</sup>  $\text{Na}_2\text{Ti}_3\text{O}_7$  particles was dispersed in distilled water and ethanol solution, and mixed with sucrose solution. Then, a heat treatment at 600°C was conducted after drying. The as-synthesized materials were characterized by a Philips XL30 environmental scanning electron microscope (ESEM) operating at 10 kV, and an FEI Tecnai G2 Sphera transmission electron microscopy (TEM) operating at 200 kV. XRD patterns were collected at ambient temperature on a Bruker D8 Advance diffractometer, using a LynxEye detector at 40 kV and 40 mA. Cu-anode ( $K\alpha$ ,  $\lambda = 1.5418 \text{ \AA}$ ) was used, with a scan speed 60 of 1 s/step, a step size of 0.02° in  $2\theta$ , and a  $2\theta$  range of 10–70°. XRD data analysis was carried out by utilizing Rietveld refinement using the FullProf software package. X-ray absorption spectroscopy measurements were performed at 20-BM-B beamline of Applied Photon Source (APS) at Argonne National Laboratory. Customized coin cells were used to prevent the sample

contamination. Measurements at the Ti K-edge were performed under transmission mode using gas ionization chamber to monitor the incident and transmitted X-ray intensities. A third ionization chamber was used in conjunction with a Ti-foil standard to provide internal calibration for the alignment of the edge positions. The incident beam was monochromatized using a Si (111) double-crystal fixed exit monochromator. Harmonic rejection was accomplished using a rhodium-coated mirror. The reference standard,  $\text{Ti}_2\text{O}_3$ , was prepared by spreading uniform layer of powders on Kapton. Each spectrum was normalized using data processing software package IFEFFIT.<sup>183</sup>

Electrochemical tests: Electrodes were prepared by mixing 70 wt% active material, 10 wt% polyvinylidene fluoride (PVdF), and 20 wt% Super P carbon black. For the electrodes fabricated with bare  $\text{Na}_2\text{Ti}_3\text{O}_7$  and carbon coated  $\text{Na}_2\text{Ti}_3\text{O}_7$ , same amount of external Super P carbon black (20 wt%) were added. A glass fiber GF/F (Whatman) filter was used as separator. 1 M  $\text{NaPF}_6$  in a 1:1 (v/v) mixture of ethylene carbonate (EC) and diethylene carbonate (DEC) solution was used as electrolyte. For half-cell test, the counter electrode was sodium metal foil (Sigma-Aldrich). For full cell tests, the counter electrode was  $\text{Na}_{0.80}\text{Li}_{0.12}\text{Ni}_{0.22}\text{Mn}_{0.66}\text{O}_2$ , reported in our previous work.<sup>222</sup> The cathode to anode weight ratio was around 2.36 : 1 in full cell. Both electrodes were directly assembled into the full cell without a pre-cycle with Na metal. All batteries were assembled in an MBraun glovebox ( $\text{H}_2\text{O} < 0.1\text{ppm}$ ). Galvanostatic discharge and charge at various current densities were performed on an Arbin BT2000 battery cycler. The voltage windows for half cell and full cell were 0.01 - 2.5 V and 2.0 - 4.2 V respectively.

Density functional theory (DFT) calculations were performed in the spin-polarized GGA + U approximations to the Density Functional Theory (DFT). Core

electron states were represented by the projector augmented-wave method<sup>152</sup> as implemented in the Vienna ab initio simulation package (VASP).<sup>153-155</sup> The Perdew-Burke-Ernzerhof exchange correlation<sup>156</sup> and a plane wave representation for the wave function with a cutoff energy of 400 eV were used. The Brillouin zone was sampled with a dense k-points mesh by Gamma packing. The supercell was composed of two formula units of  $\text{Na}_2\text{Ti}_3\text{O}_7$ . The atomic positions and cell parameters were fully relaxed to obtain total energy and optimized cell structure. The Hubbard U correction was introduced to describe the effect of localized d electrons of transition metal ions. Each transition metal ion has a unique effective U value applied in the rotationally invariant GGA + U approach. The applied effective U value given to Ti-ion was 3 eV, consistent with early work.<sup>109, 112, 157</sup>

### 7.3. Results and Discussion

$\text{Na}_2\text{Ti}_3\text{O}_7$  was prepared by a simple mechanical mixing of anatase  $\text{TiO}_2$  and anhydrous  $\text{Na}_2\text{CO}_3$ , followed by calcination at 800 °C. The as-synthesized material was well crystallized into P21/m space and adopted a pellet shape (Figure 7.1). The white color of the obtained powder suggested its intrinsic insulating property, which is undesired for battery application. Therefore, carbon coating by sucrose pyrolysis was applied to improve electronic conductivity.<sup>221</sup> The electrochemical properties were tested in Na half cell over a voltage window of 0.01–2.5 V. Figure 7.5 presents the first cycle electrochemical profile. The average intercalation potential is around 0.35 V, and a large amount of excess capacity in the first discharge is observed mainly due to irreversible Na intercalation into carbon additive (Super P) in the electrode, consistent with previous

literature.<sup>96</sup> Starting from the first charge, the theoretical capacity of  $177 \text{ mAh g}^{-1}$  (corresponding to 2 Na insertion per formula unit) is fully delivered and more than  $115 \text{ mAh g}^{-1}$  capacity is well maintained after 100 cycles for the carbon-coated  $\text{Na}_2\text{Ti}_3\text{O}_7$  (Figure 7.2(a)). Besides the excellent cycling properties, good rate performance is achieved as a result of improved electronic conductivity as illustrated in Figure 7.3. Compared with carbon-coated  $\text{Na}_2\text{Ti}_3\text{O}_7$ , the as-synthesized (henceforth referred to as “bare  $\text{Na}_2\text{Ti}_3\text{O}_7$ ”) displays notably reduced capacity (Figure 7.2(b)). Therefore, the coated carbon plays an important role in enhancing the battery performance.

To evaluate the practical application of  $\text{Na}_2\text{Ti}_3\text{O}_7$ , herein we demonstrate for the first time a full Na cell using  $\text{Na}_2\text{Ti}_3\text{O}_7$  as anode material. Figure 7.2(c) is the voltage profile of the  $\text{Na}_2\text{Ti}_3\text{O}_7 / \text{P2} - \text{Na}_{0.80}\text{Li}_{0.12}\text{Ni}_{0.22}\text{Mn}_{0.66}\text{O}_2$  full cell, in which the cathode material,  $\text{P2} - \text{Na}_{0.80}\text{Li}_{0.12}\text{Ni}_{0.22}\text{Mn}_{0.66}\text{O}_2$ , has been reported by us previously.<sup>222</sup> Due to the ultralow voltage of  $\text{Na}_2\text{Ti}_3\text{O}_7$  anode, the average voltage of this full cell is as high as 3.1 V, which is comparable to commercial Li-ion battery. As seen in Figure 7.2(c) inset, the Na full cell can easily light up a 2.5 V LED bulb. The cycling of the full cell at C/10 rate is displayed in Figure 7.2(d). The capacity is stabilized at  $105 \text{ mAh g}^{-1}$  after 25 cycles (capacity is determined by anode active material). At the same time, the coulombic efficiency is gradually increased to above 98% and maintained in the subsequent cycles. The overall energy density is  $100 \text{ Wh kg}^{-1}$ , based on the total weight of active materials from both cathode and anode. Although the energy density is lower than that of Li-ion battery, it should be noted that Na does not alloy with Al, so that the Al current collector can be used for both cathode and anode. This will help to further improve energy density of Na-ion battery and reduce manufacturing cost.

High resolution transmission electron microscopy (HRTEM) images revealed the surface morphologies for bare and carbon-coated  $\text{Na}_2\text{Ti}_3\text{O}_7$  samples. At pristine state (Figure 7.4(a) and 7.4(b)), the lattice fringes are clearly observed, implying good crystallinity. The width (0.84 nm) of neighbouring fringe distance is corresponded to (0 0 1) plane. As suggested by Figure 7.4(b), the carbon is uniformly coated on the surface of  $\text{Na}_2\text{Ti}_3\text{O}_7$  with a thickness around 3 nm. After 1<sup>st</sup> discharge, an amorphous layer with a thickness of 30-50 nm is seen on the bare  $\text{Na}_2\text{Ti}_3\text{O}_7$  particle (Figure 7.4(c)), indicating a severe side reaction at the solid electrolyte interface (SEI). In contrast, the SEI layer is largely inhibited in the carbon-coated  $\text{Na}_2\text{Ti}_3\text{O}_7$  (Figure 7.4(d)). Consequently, it is noticed that the initial coulombic efficiency is increased by 11 % from bare to carbon-coated sample (Figure 7.5). This demonstrates that in addition to improving the electronic conductivity, the coated carbon on the surface could also serve as a protection layer to prohibit side reactions of the electrolyte and enhance battery performance. It should be noted that the carbon coating could only partially improve the inefficiency in the 1<sup>st</sup> cycle, since the main irreversible capacity is resulted from Na react with super P.<sup>96</sup>

In order to understand the structural evolution and the ultra low voltage for  $\text{Na}_2\text{Ti}_3\text{O}_7$  upon cycling, the  $\text{Na}_x\text{Ti}_3\text{O}_7$  as well as its Li analogue  $\text{Li}_x\text{Ti}_3\text{O}_7$  ( $2 \leq x \leq 4$ ) was investigated by first principles calculation. The fully intercalated phase,  $\text{Na}_4\text{Ti}_3\text{O}_7$ , is identified by our calculation, which is in agreement with Dr. Palacin et.al.'s recent report.<sup>97</sup> More details of the phase transformation can be revealed by closely examining structural difference between  $\text{Na}_2\text{Ti}_3\text{O}_7$  and  $\text{Na}_4\text{Ti}_3\text{O}_7$ . As shown in Figure 7.6(a), although there is no bond broken in Ti-O frameworks, the Na sites experience drastic variations. The Na-ion coordination decreases from 9 and 7 at pristine state to 6 after

fully intercalation. In addition, to accommodate more Na ions in the structure, the lattice parameters are adjusted by shearing the Ti-O slabs. The *c* lattice parameter is considerably reduced due to better screening effect from high Na-ion concentration in Na layer. More interestingly, the dramatic Na site change is not just due to the shift of the Ti-O slab but also from contributions involving modifications within the Ti-O framework as well. After full intercalation, the joint angle between neighbouring Ti-O blocks is enlarged from 82.11° to 93.25° (Figure 7.6(b)). Therefore, it is fascinating to notice that this type of framework possesses structural flexibility to some degree, which is quite unique compared with traditional layered intercalation compounds, such as LiCoO<sub>2</sub>. As for the intercalation voltage, the calculated values for both Na<sub>*x*</sub>Ti<sub>3</sub>O<sub>7</sub> and Li<sub>*x*</sub>Ti<sub>3</sub>O<sub>7</sub> are basically consistent with experimental results.<sup>97</sup> (Figure 7.6(c)) Based on Nernst equation, the battery voltage is directly related to the Gibbs free energy change during chemical reaction. Thus, the lower voltage for Na<sub>*x*</sub>Ti<sub>3</sub>O<sub>7</sub> compared with Li<sub>*x*</sub>Ti<sub>3</sub>O<sub>7</sub> is associated with the smaller change in Gibbs free energy in the Na case. In addition, we have studied the electrostatic interaction in the crystal structure using Ewald summation.<sup>115</sup> It is interesting to see that there is a bigger jump in electrostatic energy for Na<sub>*x*</sub>Ti<sub>3</sub>O<sub>7</sub> from *x*=2 to *x*=4 than that for Li<sub>*x*</sub>Ti<sub>3</sub>O<sub>7</sub>, demonstrating a much stronger electrostatic repulsion in Na<sub>4</sub>Ti<sub>3</sub>O<sub>7</sub>. Such large electrostatic repulsion leads to structural instability and consequently, increases the Gibbs free energy for Na<sub>4</sub>Ti<sub>3</sub>O<sub>7</sub>. Therefore, the overall change in Gibbs free energy upon intercalation is reduced in Na case and the voltage is lowered accordingly.

Owing to the strong electrostatic repulsion in the fully discharged phase, Na<sub>4</sub>Ti<sub>3</sub>O<sub>7</sub>, a “self-relaxation” behaviour was observed. As shown in Figure 7.7(a), the diffraction pattern for Na<sub>4</sub>Ti<sub>3</sub>O<sub>7</sub> phase is obtained right after the full discharge was

completed. However, for the electrodes stored in the glovebox for 3 and 10 days after full discharge, the intensity of peaks from  $\text{Na}_4\text{Ti}_3\text{O}_7$  phase, such as (-3 0 2) and (1 0 4) gradually and systematically diminishes. Concomitantly, the diffraction peaks from the  $\text{Na}_2\text{Ti}_3\text{O}_7$  phase increases steadily. These observations suggest that the  $\text{Na}_4\text{Ti}_3\text{O}_7$  structure undergoes self-relaxation progressively. This property is also captured electrochemically. Figure 7.8(a) and 7.8(b) compare the voltage profiles for  $\text{Na}_2\text{Ti}_3\text{O}_7$  under cycling with and without interval rest (between charge and discharge) respectively. It is observed that the open circuit voltage for the cell with interval rest is increased gradually during the rest time, indicating the structural relaxation. Additionally, though the discharge performances are identical in the two cases, the cell with interval rest can only deliver 130 mAh  $\text{g}^{-1}$  capacity in the first charge and further decay is seen in the subsequent cycles (Figure 7.8(c) and 7.9). Considering that this self-relaxation in the anode material would lead to self-discharge in the actual full cell, it could be one of the main bottlenecks using  $\text{Na}_2\text{Ti}_3\text{O}_7$  as anode for Na-ion battery in practice.

The electronic transition was detected by in-situ X-ray absorption spectroscopy (XAS). Customized coin cells were used to prevent the sample contamination. As  $\text{Ti}^{3+}$  is extremely sensitive to oxidization ( $\text{Ti}^{3+} \rightarrow \text{Ti}^{4+}$ ), any ex-situ characterization attempts to detect Ti reduction during lithiation process were not successful. It is important to make sure that throughout the entire characterization process, the electrodes were never exposed to the ambient environment. In Figure 7.7(b), the Ti-K edge is gradually shifted towards lower energy region from pristine state to 0.01 V. The shape and position of the pre-edge as well as the position of the main edge for the fully discharged sample approach those found for  $\text{Ti}_2\text{O}_3$ , demonstrating that  $\text{Ti}^{4+}$  is reduced upon Na-ion

intercalation. The decrease in the pre-edge peak is ascribed to the reduced hybridization between Ti-3d and O-2p orbitals during Ti ion reduction.<sup>223, 224</sup> In fact, this Ti reduction is similar to its Li counterparts.<sup>223, 225, 226</sup> Therefore, it is speculated that the ultra-low voltage for Na<sub>2</sub>Ti<sub>3</sub>O<sub>7</sub> material during intercalation could mainly originate from crystal structural perspective as discussed above, instead of electronic contribution.

#### **7.4. Conclusion**

In summary, a comprehensive study on Na<sub>2</sub>Ti<sub>3</sub>O<sub>7</sub> as an ultra-low voltage anode for Na-ion batteries is reported. The cyclability and coulombic efficiency are significantly enhanced, due to increased electronic conductivity and reduced SEI formation by carbon coating. Na full cell with high operating voltage is demonstrated by taking advantage of the ultra-low voltage of Na<sub>2</sub>Ti<sub>3</sub>O<sub>7</sub> anode. The self-relaxation behaviour for fully intercalated phase, Na<sub>4</sub>Ti<sub>3</sub>O<sub>7</sub>, is shown for the first time, which results from structural instability as suggested by first principles calculation. Ti<sup>4+</sup> / Ti<sup>3+</sup> is the active redox couple upon cycling based on XANES characterization. These findings unravel the underlying relation between unique properties and battery performance of Na<sub>2</sub>Ti<sub>3</sub>O<sub>7</sub> anode, which should ultimately shed light on possible strategies for future improvement.

Chapter 7, in full, is currently being prepared for publication of the material “Understanding Na<sub>2</sub>Ti<sub>3</sub>O<sub>7</sub> as an ultra-low voltage anode material for Na-ion battery”. The dissertation author was the primary investigator and author of this paper. All the computation XAS were conducted by the author and the paper was written by the author.

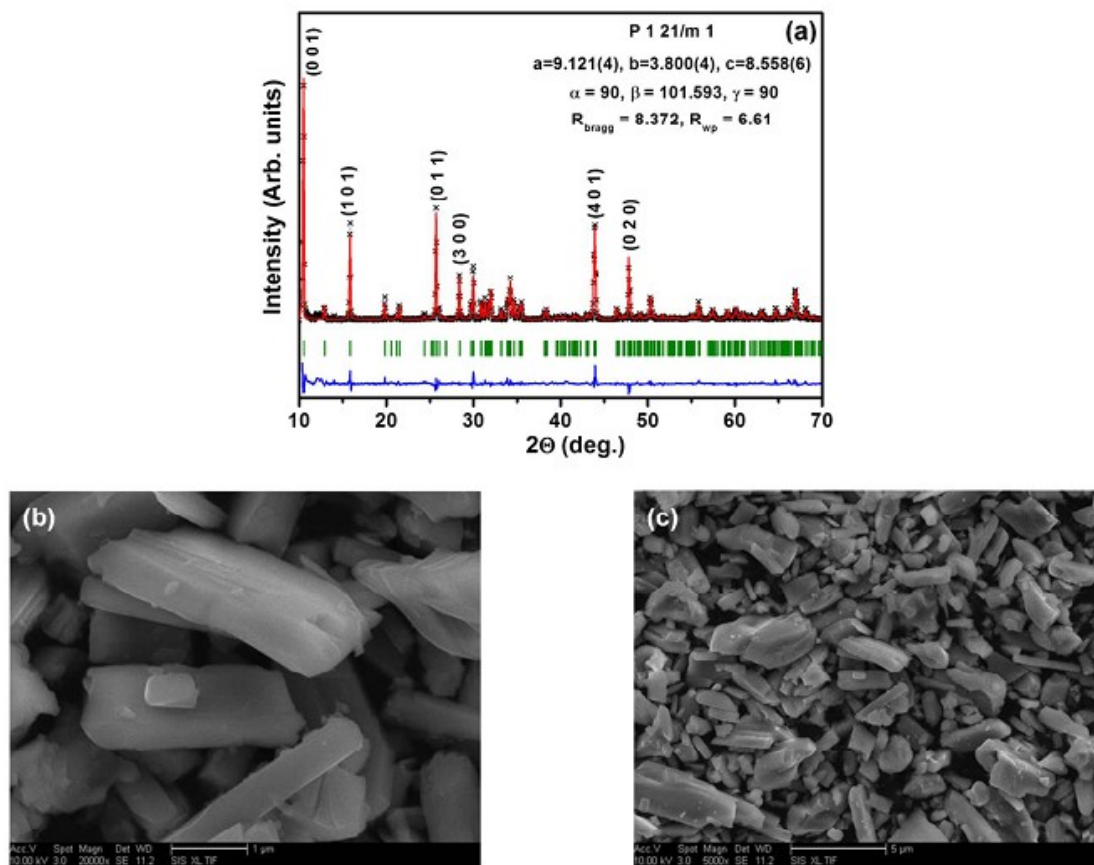


Figure 7.1 The (a) XRD and (b) (c) SEM images of as-synthesized  $\text{Na}_2\text{Ti}_3\text{O}_7$  powder.

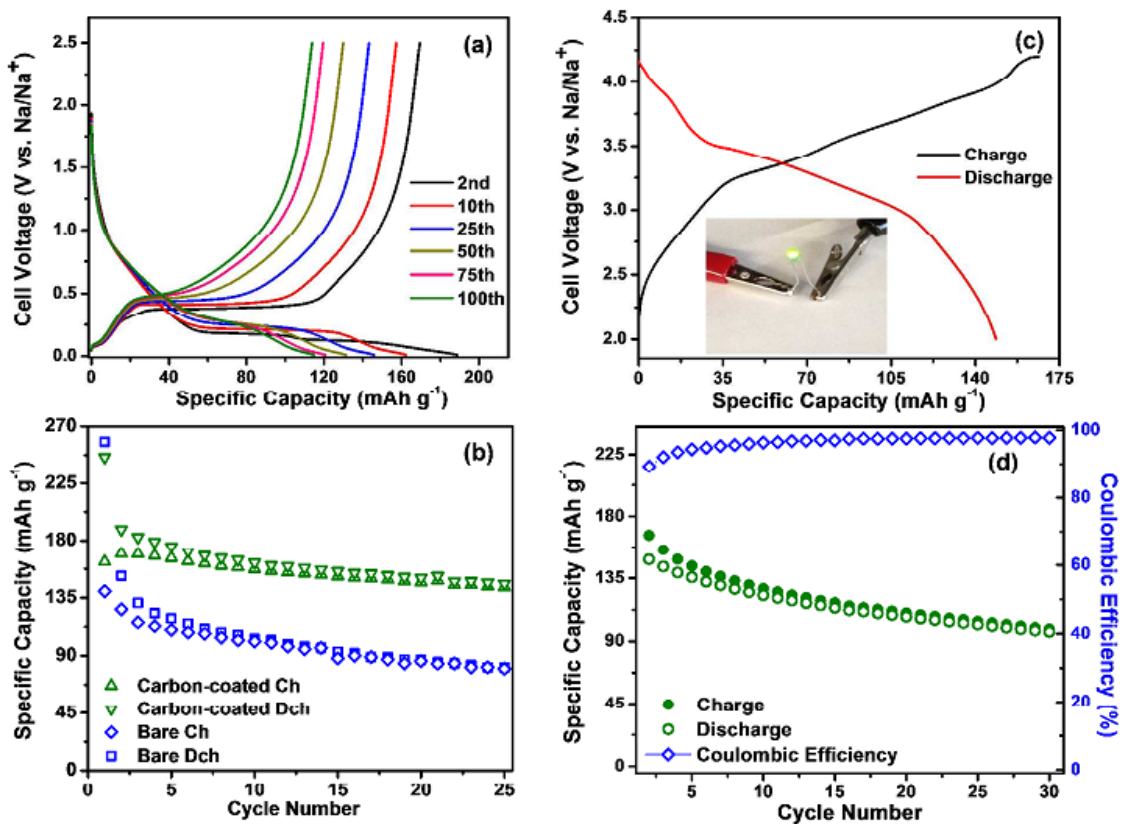


Figure 7.2 (a) Voltage profiles of carbon-coated  $\text{Na}_2\text{Ti}_3\text{O}_7$  in the 2<sup>nd</sup>, 10<sup>th</sup>, 25<sup>th</sup>, 50<sup>th</sup>, 75<sup>th</sup> and 100<sup>th</sup> cycles at C/10 rate. (b) Cycling performance for carbon-coated and bare  $\text{Na}_2\text{Ti}_3\text{O}_7$ . (c) Voltage profiles and (d) Cycling performance for the Na full cell (the specific capacity is calculated based on anode materials).

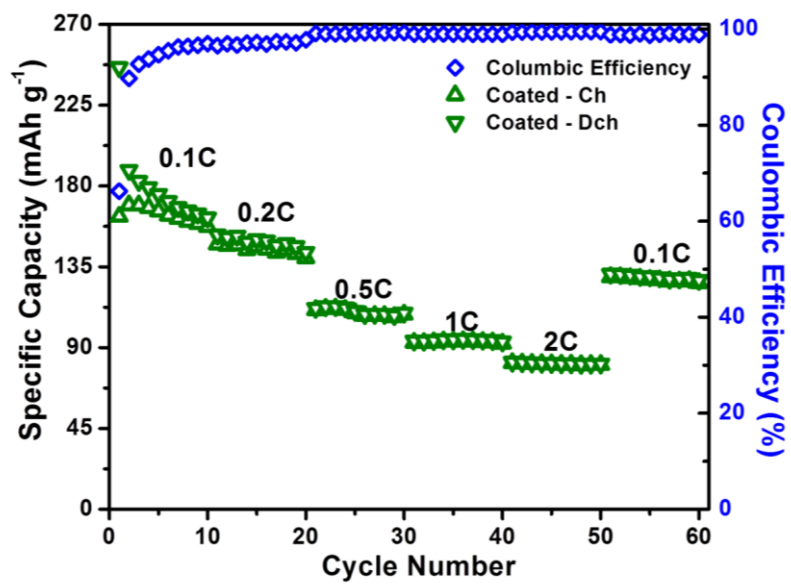


Figure 7.3 Rate performance of carbon-coated Na<sub>2</sub>Ti<sub>3</sub>O<sub>7</sub> electrode.

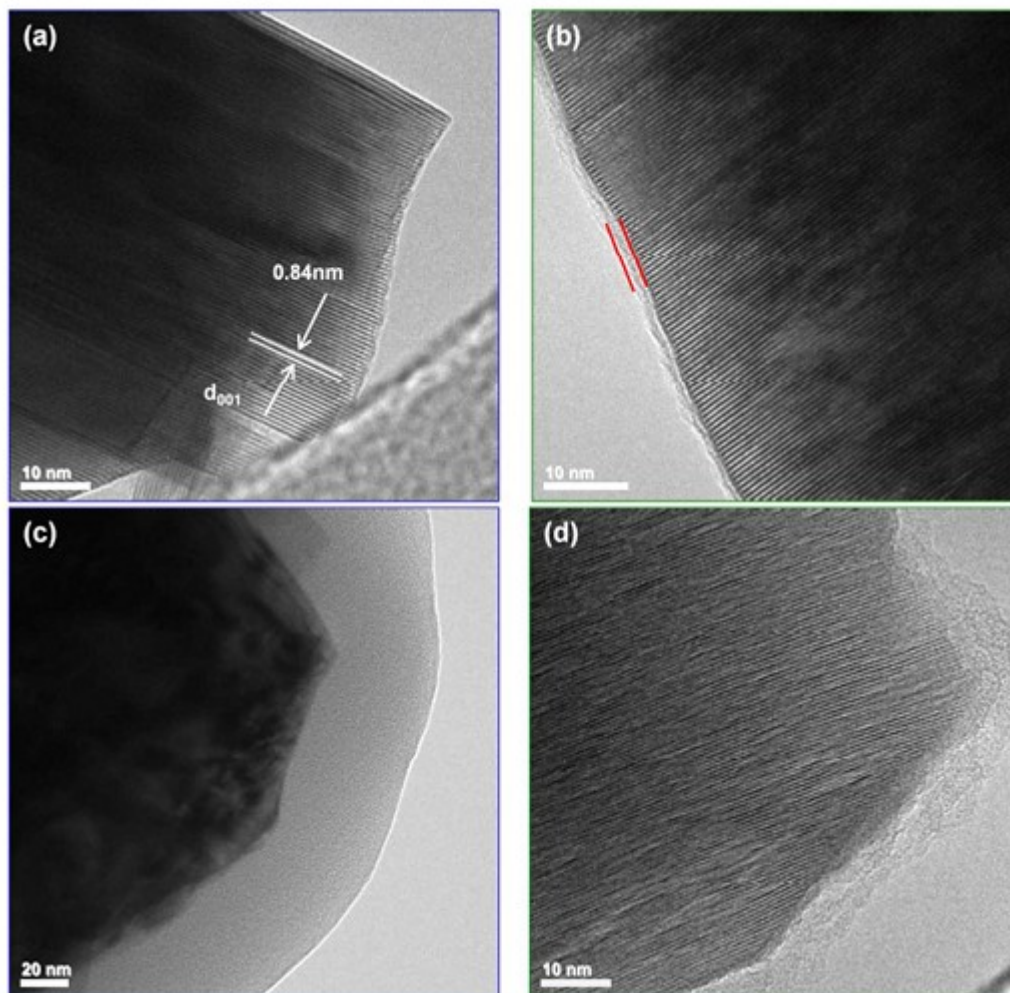


Figure 7.4 TEM images for (a) bare and (b) carbon-coated  $\text{Na}_2\text{Ti}_3\text{O}_7$  at pristine state. TEM images for (c) bare and (d) carbon-coated  $\text{Na}_2\text{Ti}_3\text{O}_7$  after 1<sup>st</sup> discharge.

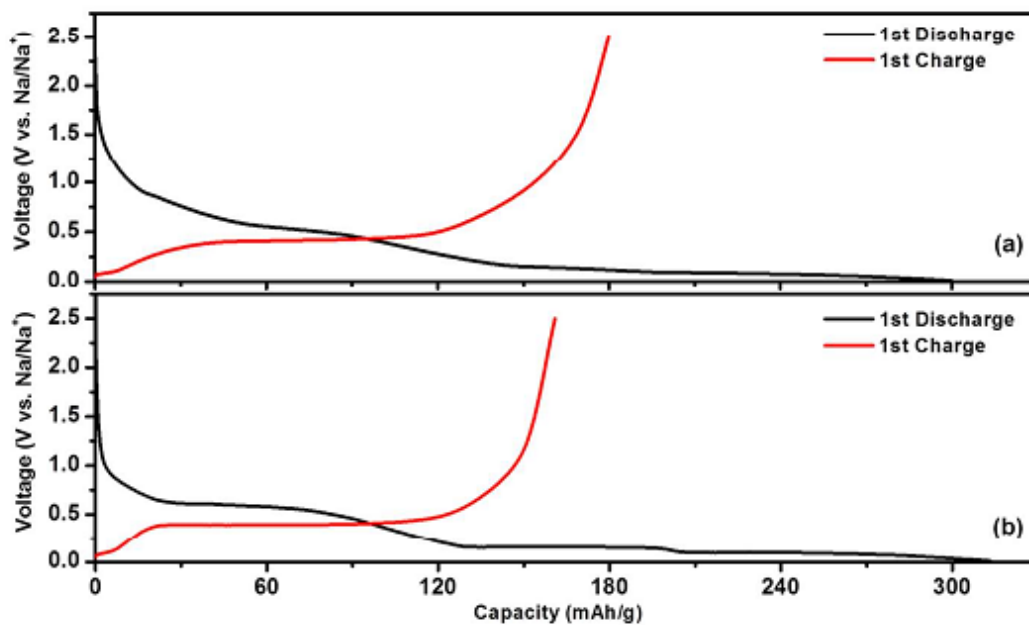


Figure 7.5 Electrochemical profiles at of (a) carbon-coated and (b) bare Na<sub>2</sub>Ti<sub>3</sub>O<sub>7</sub> at C/25.

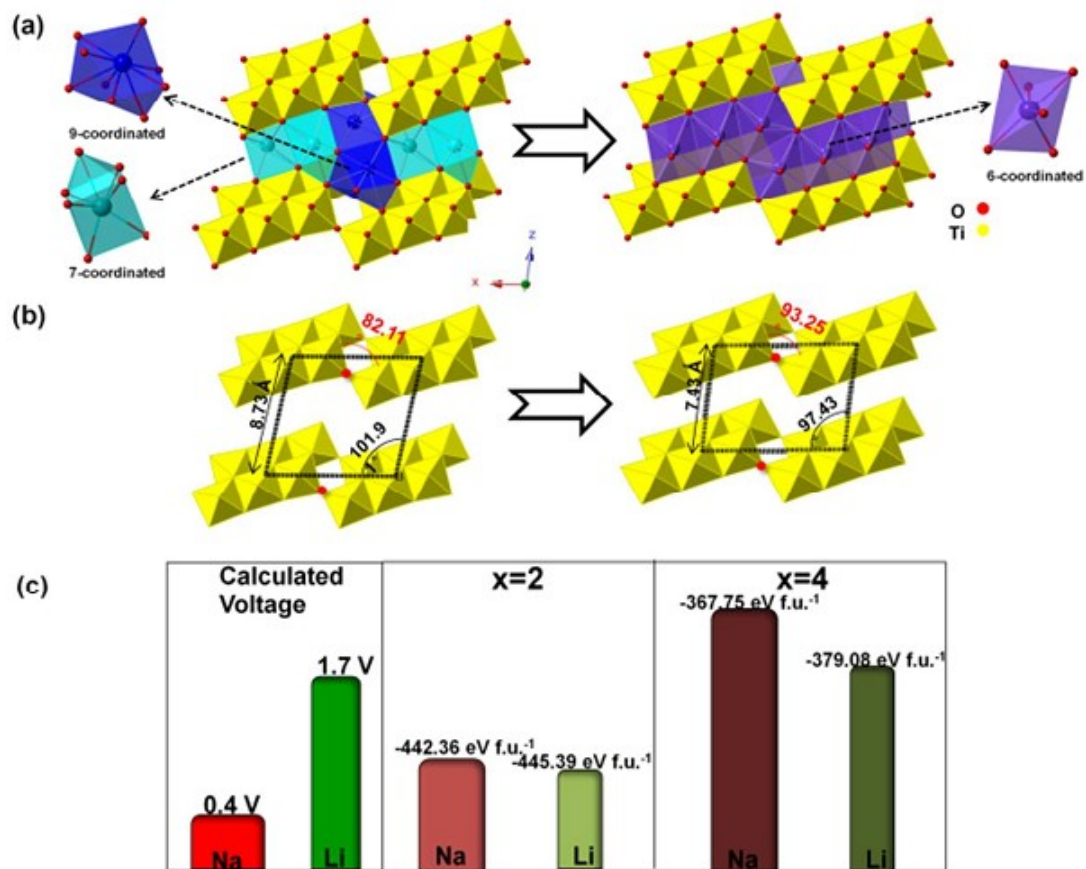


Figure 7.6 (a) The phase transformation (b) related structural change upon Na intercalation. (c) The calculated voltage and electrostatic energy at  $x=2$  and  $x=4$  for  $\text{Li}_x\text{Ti}_3\text{O}_7$  and  $\text{Na}_x\text{Ti}_3\text{O}_7$  respectively. The narrow bar is for  $\text{Li}_x\text{Ti}_3\text{O}_7$  and wide one for  $\text{Na}_x\text{Ti}_3\text{O}_7$ .

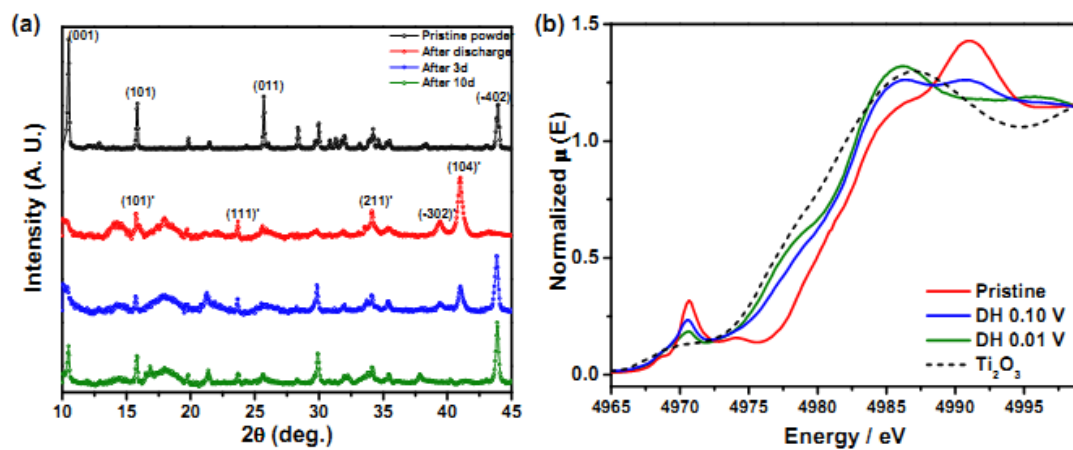


Figure 7.7 (a) Change in the XRD patterns with time for fully discharged electrodes. (b) Normalized Ti K-edge XANES for Na<sub>2</sub>Ti<sub>3</sub>O<sub>7</sub> at pristine state (red), after discharged to 0.10 V (blue), and after discharged to 0.01 V (green).

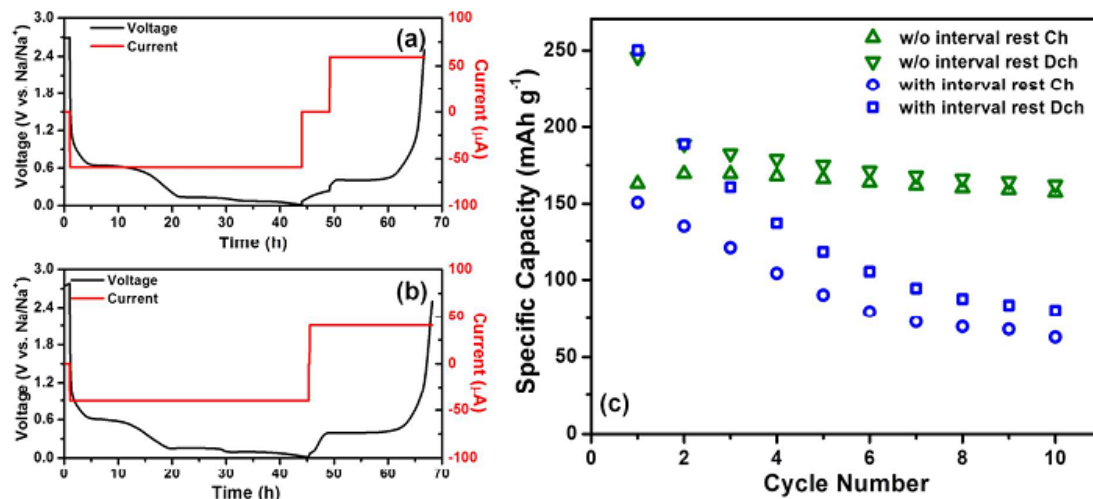


Figure 7.8 Voltage profiles for electrodes under cycling (a) with and (b) without interval rest (5 hour between charge and discharge). (c) Cycling performance for cell with (blue) and without (green) interval rest.

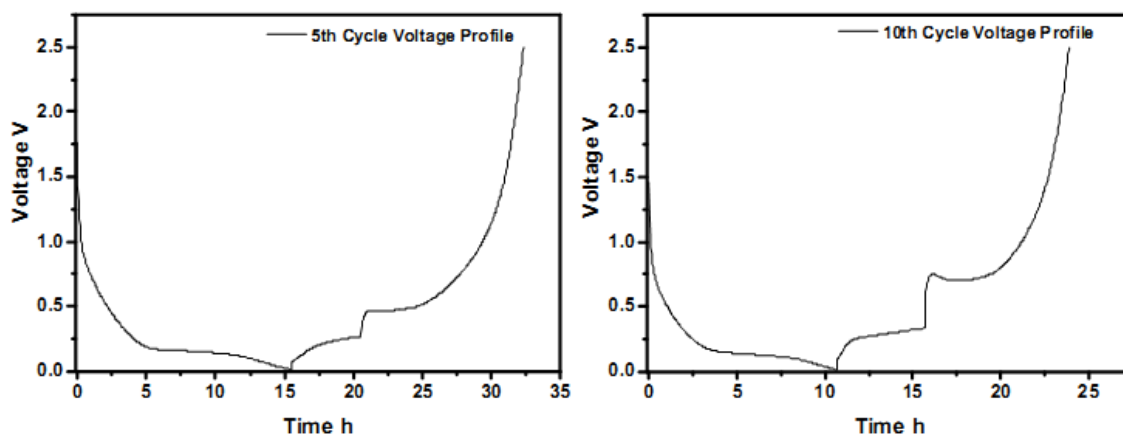


Figure 7.9 5<sup>th</sup> and 10<sup>th</sup> Voltage profiles for electrodes with interval rest (5 hour between charge and discharge).

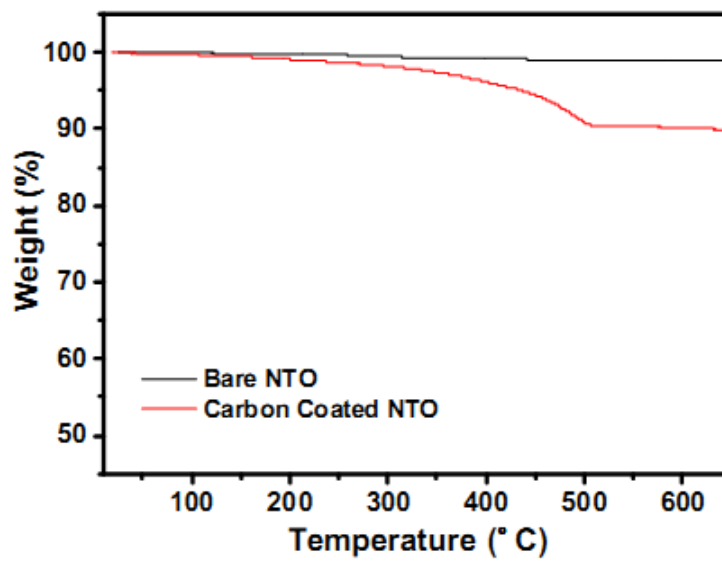


Figure 7.10 Thermogravimetric analysis for bare (black) and carbon coated (red)  $\text{Na}_2\text{Ti}_3\text{O}_7$  powder.

## Chapter 8. Summary and future work

The focus of this research is to design and diagnose novel electrode materials for Na-ion batteries by combining advanced characterization tools and first principles calculations. The iterative practice of experiment and computation provides pathways to tackle problems whenever either of the methods alone is insufficient. Integrating experimental and computational efforts together is proved to be effective and efficient in my research on Na-ion batteries. Na-ion battery has similar working principles with Li-ion battery: during charging, Na ions are extracted from the cathode and inserted into the anode; during discharging, they are transferred reversely. By this process, the energy storage and released reversibly. Therefore, in order to realize high energy-density, high power-density and long life for Na-ion batteries. Both cathode and anode materials should be designed and optimized.

In the cathode direction, I prepared P2 -  $\text{Na}_{2/3}[\text{Ni}_{1/3}\text{Mn}_{2/3}]\text{O}_2$  with excellent cycling property and high rate capability as a cathode material for Na-ion batteries. The phase transformation from P2 to O2 at 4.22 V was investigated by first principles formation energy calculation and confirmed by synchrotron XRD. The specific Na-ions orderings were found at  $\text{Na} = 1/3$  and  $1/2$ , which are corresponding to the voltage steps in the charging profile. Based on both GITT measurement and NEB calculation, the diffusivity of Na-ions in P2 structure is indeed higher than that in the corresponding O3 structured Li compounds. The electronic structures have been studied and DOS calculation suggested that oxygen partially participates the redox reaction at the end of the electrochemical charge. Consequently, it was demonstrated that the capacity retention

of 95% after 50 cycles could be obtained by excluding the P2–O2 phase transformation and 85% of the reversible capacity could be retained at a 1C rate. In addition, a simple synthesis method can be used to prepare this material without any special nano-scale fabrication. This study demonstrate that P2 -  $\text{Na}_{2/3}[\text{Ni}_{1/3}\text{Mn}_{2/3}]\text{O}_2$  is a strong candidate for cathode in Na-ion batteries for large-scale energy storage.

In order to further increase the energy density for cathodes, an in-depth understanding of the interplay between structural properties and electrochemical performances is required to improve the performances of Na-ion batteries. A promising Na cathode material, P2- $\text{Na}_{0.8}[\text{Li}_{0.12}\text{Ni}_{0.22}\text{Mn}_{0.66}]\text{O}_2$ , was comprehensively studied using neutron diffraction,  $^7\text{Li}$  solid-state MAS NMR, *in situ* SXR and XAS. Most of the substituted Li ions occupy TM sites with a high number of nearest-neighbor Mn ions (4, 5 or 6), a result confirmed by both neutron diffraction and NMR. Enhanced electrochemical properties, among which improved cycling performance and rate capability, are obtained along with single smooth voltage profiles. In contrast to most of the P2-type cathodes reported so far, *in situ* SXR proves that the frequently observed P2-O2 phase transformation is inhibited in this Li-substituted material even when the electrode is charged to 4.4 V. On the other hand, the P2 to O2 phase change is clearly observed when all of the Na ions are extracted from the structure under CCCV charge. Based on these observations, Li substitution in the TM layer enables enough Na ions to be left in the structure to maintain the P2 structure up to 4.4 V charge. Although Li-ions migrate to octahedral or, to a lesser extent, to low coordination sites in the Na layer formed by local stacking faults during the charging process, most of them return to the TM layer after discharge. XAS results show that  $\text{Ni}^{2+}/\text{Ni}^{4+}$  is the only active redox couple

during cycling. Finally, an optimum composition,  $\text{Na}_{0.83}[\text{Li}_{0.07}\text{Ni}_{0.31}\text{Mn}_{0.62}]\text{O}_2$ , has been proposed on the basis of the design principles for Na-ion cathode elucidated as part of this study, opening up new perspectives for further exploration of high energy Na-ion batteries.

In addition to P2-structured oxides, a new O3 -  $\text{Na}_{0.78}\text{Li}_{0.18}\text{Ni}_{0.25}\text{Mn}_{0.583}\text{O}_2$  was obtained by the electrochemical Na-Li ion exchange process of  $\text{Li}_{1.167}\text{Ni}_{0.25}\text{Mn}_{0.583}\text{O}_2$ . The new material shows exceptionally high discharge capacity of 240 mAh/g in the voltage range of 1.5-4.5 V, which is the highest capacity as well as highest energy density so far among all the reported Na cathode materials. When cycled between 1.5-4.2 V, the discharge capacity is well maintained around 190 mAh/g after 30 cycles. The O3 phase is kept through ion-exchange and cycling process, as confirmed by SXRD. XAS results show that  $\text{Ni}^{2+}/\text{Ni}^{4+}$  is the main active redox couple during cycling while Mn ions basically stay at tetravalent state. The Na full cell utilizing this material as cathode delivers 430 Wh / kg energy density. Future improvement could be realized through further tuning the combination and ratio among TMs, and the material by direct synthesis is under development, which would be reported very soon.

As for the anode direction, a comprehensive study on  $\text{Na}_2\text{Ti}_3\text{O}_7$  as an ultra-low voltage anode for Na-ion batteries was led by me. The cycling and coulombic efficiency are significantly enhanced, due to increased electronic conductivity and reduced SEI formation by carbon coating. Na full cell with high operating voltage is demonstrated by taking advantage of the ultra-low voltage of  $\text{Na}_2\text{Ti}_3\text{O}_7$  anode. The self-relaxation behavior for fully intercalated phase,  $\text{Na}_4\text{Ti}_3\text{O}_7$ , is shown for the first time, which results from structural instability as suggested by first principles calculation.  $\text{Ti}^{4+} / \text{Ti}^{3+}$  is the

active redox couple upon cycling based on XANES characterization. These findings unravel the underlying relation between unique properties and battery performance of  $\text{Na}_2\text{Ti}_3\text{O}_7$  anode, which should ultimately shed light on possible strategies for future improvement.

For future work, considering that about twice as many Na compounds as Li compounds are present in ICSD (inorganic crystallographic structure database),<sup>227</sup> there may be superior NIB electrode materials which have not been discovered yet. My research also suggests that in many cases the Na-reaction behavior of a material is not equivalently identical to its behavior in the Li-ion batteries. Therefore more novel candidates could be explored for the NIB electrode materials, and significant opportunity exists to demonstrate high capacity / long life. In the cathode field, the future of layered oxide materials as high capacity Na-ion battery cathodes is quite promising due to the many factors mentioned in this thesis, but there is much to learn about this system before this material can be used in a practical battery, including ion transport, band structure and reaction path. Additionally, more attention should be put on safety issues of the layered oxides cathodes, since it is one of the common problems for layered materials in Li-ion batteries. Regarding to the anode materials, for a low-cost and large-scale application system the hope is to develop better carbon based or titanium oxide or polyanionic based systems capable of reversibly inserting sodium at quite low voltages with stable SEI layer formation. Besides, to make breakthrough in the energy density, the research on anode materials in Na-ion batteries is moving on the search for novel anode materials. Alloy-, and conversion-based materials are considered as promising candidates because they have considerably high specific capacity. However, for these series of materials, dramatic

volume variations during sodiation / desodiation is one of the main limitations. Tailored design of electrode material and improved electrochemical cell engineering are required to mitigate these shortcomings.

In addition to the electrode materials, the investigation on the electrolyte should not be overlooked, because electrolytes are essential for the proper function of any battery technologies. As in any other battery system, a good electrolyte should possess: (i) good ionic conductivity, (ii) a large electrochemical window (i.e., high and low onset potential for electrolyte decomposition through oxidation and reduction at high and low voltages, respectively), (iii) no reactivity towards the battery components, and (iv) a large thermal stability window (i.e. melting point and boiling point lower and higher than the standard temperatures for the battery utilization, respectively). Finally, it should have as low toxicity as possible and meet cost requirements for the targeted applications. All these features are intrinsically dependent on the nature of the salt and the solvent(s) and the possible use of additives.<sup>228</sup>

More alternate approaches could be explored to increase the energy density for Na-ion batteries. Research on “low temperature” Na-S batteries, analogous to Li-S batteries which offer great promise as low-cost, high-capacity energy storage systems, is underway. The batteries operate either at room-temperature or just below 100 C, and rely on conventional separators and organic electrolytes containing sodium salts such as NaPF<sub>6</sub>; and a porous conductive carbon to contain the sulfur at the positive electrode. The theoretical gravimetric capacity of the sulfur electrode is 1672 mAh/g based on full reduction to Na<sub>2</sub>S, although currently only one third could be delivered reversibly. This problem is mainly due to the formation of soluble polysulfides which diffuse through the

electrolyte to the negative electrode to form lower-order polysulfides.<sup>3</sup> The future of this low-temperature Na-S battery lies in designing protective layers and supportive binders for both electrodes, and developing novel electrolytes.

## References

1. H. L. Pan, Y. S. Hu and L. Q. Chen, *Energy & Environmental Science*, 2013, **6**, 2338-2360.
2. J. M. Tarascon and M. Armand, *Nature*, 2001, **414**, 359-367.
3. B. L. Ellis and L. F. Nazar, *Current Opinion in Solid State & Materials Science*, 2012, **16**, 168-177.
4. F. Risacher and B. Fritz, *Aquatic Geochemistry*, 2009, **15**, 123-157.
5. A. Yaksic and J. E. Tilton, *Resources Policy*, 2009, **34**, 185-194.
6. S. Y. Hong, Y. Kim, Y. Park, A. Choi, N. S. Choi and K. T. Lee, *Energy & Environmental Science*, 2013, **6**, 2067-2081.
7. K. Xu, *Chemical Reviews*, 2004, **104**, 4303-4417.
8. R. Fong, U. Vonsacken and J. R. Dahn, *Journal of the Electrochemical Society*, 1990, **137**, 2009-2013.
9. L. Y. Beaulieu, T. D. Hatchard, A. Bonakdarpour, M. D. Fleischauer and J. R. Dahn, *Journal of the Electrochemical Society*, 2003, **150**, A1457-A1464.
10. V. Palomares, P. Serras, I. Villaluenga, K. B. Hueso, J. Carretero-Gonzalez and T. Rojo, *Energy & Environmental Science*, 2012, **5**, 5884-5901.
11. W. R. Liu, M. H. Yang, H. C. Wu, S. M. Chiao and N. L. Wu, *Electrochemical and Solid State Letters*, 2005, **8**, A100-A103.
12. J. Li, R. B. Lewis and J. R. Dahn, *Electrochemical and Solid State Letters*, 2007, **10**, A17-A20.
13. P. Arora and Z. M. Zhang, *Chemical Reviews*, 2004, **104**, 4419-4462.
14. A. J. Fry and J. Touster, *Journal of Organic Chemistry*, 1989, **54**, 4829-4832.
15. L. J. Krause, W. Lamanna, J. Summerfield, M. Engle, G. Korba, R. Loch and R. Atanasoski, *Journal of Power Sources*, 1997, **68**, 320-325.
16. M. Ue and S. Mori, *Journal of the Electrochemical Society*, 1995, **142**, 2577-2581.
17. D. Guyomard and J. M. Tarascon, *Solid State Ionics*, 1994, **69**, 222-237.
18. *Lithium-ion batteries. Fundamentals and performance*, 1998, 255 pp.

19. S. T. Myung, Y. Hitoshi and Y. K. Sun, *Journal of Materials Chemistry*, 2011, **21**, 9891-9911.
20. M. R. Palacin, *Chemical Society Reviews*, 2009, **38**, 2565-2575.
21. C. Delmas, C. Fouassier and P. Hagenmuller, *Physica B & C*, 1980, **99**, 81-85.
22. C. Delmas, C. Fouassier and P. Hagenmuller, *Journal of Solid State Chemistry*, 1975, **13**, 165-171.
23. C. Fouassier, C. Delmas and P. Hagenmuller, *Materials Research Bulletin*, 1975, **10**, 443-449.
24. C. DELMAS, J.-J. BRACONNIER, C. FOUASSIER and P. HAGENMULLER, *Solid State Ionics*, 1981, **3**, 165-169.
25. J. J. Braconnier, C. Delmas and P. Hagenmuller, *Materials Research Bulletin*, 1982, **17**, 993-1000.
26. A. Mendiboure, C. Delmas and P. Hagenmuller, *Journal of Solid State Chemistry*, 1985, **57**, 323-331.
27. Y. Takeda, K. Nakahara, M. Nishijima, N. Imanishi, O. Yamamoto, M. Takano and R. Kanno, *Materials Research Bulletin*, 1994, **29**, 659-666.
28. S. Komaba, C. Takei, T. Nakayama, A. Ogata and N. Yabuuchi, *Electrochemistry Communications*, 2010, **12**, 355-358.
29. S. Komaba, T. Nakayama, A. Ogata, T. Shimizu, C. Takei, S. Takada, A. Hokura and I. Nakai, *ECS Transactions*, 2009, **16**, 43-55.
30. S. Komaba, N. Yabuuchi, T. Nakayama, A. Ogata, T. Ishikawa and I. Nakai, *Inorganic Chemistry*, 2012, **51**, 6211-6220.
31. D. Kim, E. Lee, M. Slater, W. Lu, S. Rood and C. S. Johnson, *Electrochemistry Communications*, 2012, **18**, 66-69.
32. M. Sathiya, K. Hemalatha, K. Ramesha, J.-M. Tarascon and A. S. Prakash, *Chemistry of Materials*, 2012, **24**, 1846-1853.
33. R. Berthelot, D. Carlier and C. Delmas, *Nature Materials*, 2011, **10**, 74-80.
34. M. Guignard, C. Didier, J. Darriet, P. Bordet, E. Elkaïm and C. Delmas, *Nature Materials*, 2013, **12**, 74-80.
35. D. Carlier, J. H. Cheng, R. Berthelot, M. Guignard, M. Yoncheva, R. Stoyanova, B. J. Hwang and C. Delmas, *Dalton Transactions*, 2011, **40**, 9306.

36. Z. H. Lu and J. R. Dahn, *Journal of the Electrochemical Society*, 2001, **148**, A710-A715.
37. Z. H. Lu and J. R. Dahn, *Journal of the Electrochemical Society*, 2001, **148**, A1225-A1229.
38. D. H. Lee, J. Xu and S. Y. Meng, *Physical Chemistry Chemical Physics*, 2012.
39. D. Kim, S. H. Kang, M. Slater, S. Rood, J. T. Vaughey, N. Karan, M. Balasubramanian and C. S. Johnson, *Advanced Energy Materials*, 2011, **1**, 333-336.
40. N. Yabuuchi, M. Kajiyama, J. Iwatate, H. Nishikawa, S. Hitomi, R. Okuyama, R. Usui, Y. Yamada and S. Komaba, *Nature Materials*, 2012, **11**, 512–517.
41. S. Yao, S. Hosohara, Y. Shimizu, N. Miura, H. Futata and N. Yamazoe, *Chemistry Letters*, 1991, 2069-2072.
42. U. von Alpen, M. F. Bell and W. Wichelhaus, *Materials Research Bulletin*, 1979, **14**, 1317-1322.
43. P. Knauth, *Solid State Ionics*, 2009, **180**, 911-916.
44. C. Delmas, F. Cherkaoui, A. Nadiri and P. Hagenmuller, *Materials Research Bulletin*, 1987, **22**, 631-639.
45. C. Delmas, A. Nadiri and J. L. Soubeyroux, *Solid State Ionics*, 1988, **28**, 419-423.
46. J. Gopalakrishnan and K. K. Rangan, *Chemistry of Materials*, 1992, **4**, 745-747.
47. O. Tillement, J. Angenault, J. C. Couturier and M. Quarton, *Solid State Ionics*, 1992, **53**.
48. K. S. Nanjundaswamy, A. K. Padhi, J. B. Goodenough, S. Okada, H. Ohtsuka, H. Arai and J. Yamaki, *Solid State Ionics*, 1996, **92**, 1-10.
49. S. Patoux, G. Rouse, J. B. Leriche and C. Masquelier, *Chemistry of Materials*, 2003, **15**, 2084-2093.
50. L. S. Plashnitsa, E. Kobayashi, Y. Noguchi, S. Okada and J.-i. Yamaki, *Journal of the Electrochemical Society*, 2010, **157**.
51. Z. L. Jian, L. Zhao, H. L. Pan, Y. S. Hu, H. Li, W. Chen and L. Q. Chen, *Electrochemistry Communications*, 2012, **14**, 86-89.
52. K. Sung-Wook, S. Dong-Hwa, M. Xiaohua, G. Ceder and K. Kisuk, *Advanced Energy Materials*, 2012, **2**, 710-721.

53. Y. Uebou, T. Kiyabu, S. Okada and J. I. Yamaki, *The Rep Inst Adv Mater Study*, 2002, vol. 16, p. 1.
54. J. Kang, S. Baek, V. Mathew, J. Gim, J. Song, H. Park, E. Chae, A. K. Rai and J. Kim, *Journal of Materials Chemistry*, 2012, **22**, 20857-20860.
55. K. Saravanan, C. W. Mason, A. Rudola, K. H. Wong and P. Balaya, *Advanced Energy Materials*, 2012.
56. Z. L. Gong and Y. Yang, *Energy & Environmental Science*, 2011, **4**, 3223-3242.
57. A. K. Padhi, K. S. Nanjundaswamy and J. B. Goodenough, *Journal of the Electrochemical Society*, 1997, **144**, 1188-1194.
58. T. Shiratsuchi, S. Okada, J. Yamaki and T. Nishida, *Journal of Power Sources*, 2006, **159**, 268-271.
59. P. Moreau, D. Guyomard, J. Gaubicher and F. Boucher, *Chemistry of Materials*, 2010, **22**, 4126-4128.
60. K. Zaghbi, J. Trottier, P. Hovington, F. Brochu, A. Guerfi, A. Mauger and C. M. Julien, *Journal of Power Sources*, 2011, **196**, 9612-9617.
61. M. Casas-Cabanas, V. V. Roddatis, D. Saurel, P. Kubiak, J. Carretero-Gonzalez, V. Palomares, P. Serras and T. Rojo, *Journal of Materials Chemistry*, 2012, **22**.
62. K. T. Lee, T. N. Ramesh, F. Nan, G. Botton and L. F. Nazar, *Chemistry of Materials*, 2011, **23**, 3593-3600.
63. J. Barker, M. Y. Saidi and J. L. Swoyer, *Electrochemical and Solid State Letters*, 2003, **6**, A1-A4.
64. J. M. Le Meins, M. P. Crosnier-Lopez, A. Hemon-Ribaud and G. Courbion, *Journal of Solid State Chemistry*, 1999, **148**, 260-277.
65. J. Barker, R. K. B. Gover, P. Burns and A. J. Bryan, *Electrochemical and Solid State Letters*, 2006, **9**, A190-A192.
66. R. A. Shakoor, D. H. Seo, H. Kim, Y. U. Park, J. Kim, S. W. Kim, H. Gwon, S. Lee and K. Kang, *Journal of Materials Chemistry*, 2012, **22**, 20535-20541.
67. F. Sauvage, E. Quarez, J. M. Tarascon and E. Baudrin, *Solid State Sciences*, 2006, **8**, 1215-1221.
68. B. L. Ellis, W. R. M. Makahnouk, Y. Makimura, K. Toghill and L. F. Nazar, *Nature Materials*, 2007, **6**, 749-753.

69. N. Recham, J. N. Chotard, L. Dupont, K. Djellab, M. Armand and J. M. Tarascon, *Journal of the Electrochemical Society*, 2009, **156**, A993-A999.
70. Y. Uebou, S. Okada and J. Yamaki, *Electrochemistry*, 2003, **71**.
71. P. Barpanda, S.-i. Nishimura and A. Yamada, *Advanced Energy Materials*, 2012, **2**.
72. P. Barpanda, T. Ye, S. Nishimura, S. C. Chung, Y. Yamada, M. Okubo, H. S. Zhou and A. Yamada, *Electrochemistry Communications*, 2012, **24**, 116-119.
73. M. Ati, L. Dupont, N. Recham, J. N. Chotard, W. T. Walker, C. Davoisne, P. Barpanda, V. Sarou-Kanian, M. Armand and J. M. Tarascon, *Chemistry of Materials*, 2010, **22**, 4062-4068.
74. R. Tripathi, T. N. Ramesh, B. L. Ellis and L. F. Nazar, *Angewandte Chemie-International Edition*, 2010, **49**, 8738-8742.
75. B. L. Ellis, T. N. Ramesh, L. J. M. Davis, G. R. Goward and L. F. Nazar, *Chemistry of Materials*, 2011, **23**, 5138-5148.
76. R. Tripathi, G. R. Gardiner, M. S. Islam and L. F. Nazar, *Chemistry of Materials*, 2011, **23**, 2278-2284.
77. M. D. Slater, D. Kim, E. Lee and C. S. Johnson, *Advanced Functional Materials*, 2012.
78. G. E. Pascal and M. Fouletier, *Solid State Ionics*, 1988, **28**, 1172-1175.
79. D. A. Stevens and J. R. Dahn, *Journal of the Electrochemical Society*, 2001, **148**, A803-A811.
80. D. A. Stevens and J. R. Dahn, *Journal of the Electrochemical Society*, 2000, **147**, 1271-1273.
81. D. A. Stevens and J. R. Dahn, *Journal of the Electrochemical Society*, 2000, **147**, 4428-4431.
82. R. Alcantara, J. M. Jimenez-Mateos, P. Lavela and J. L. Tirado, *Electrochemistry Communications*, 2001, **3**, 639-642.
83. S. Komaba, W. Murata, T. Ishikawa, N. Yabuuchi, T. Ozeki, T. Nakayama, A. Ogata, K. Gotoh and K. Fujiwara, *Advanced Functional Materials*, 2011, **21**, 3859-3867.
84. A. Darwiche, C. Marino, M. T. Sougrati, B. Fraisse, L. Stievano and L. Monconduit, *Journal of the American Chemical Society*, 2012, **134**, 20805-20811.

85. X. Yunhua, Z. Yujie, L. Yihang and W. Chunsheng, *Advanced Energy Materials*, 2013, **3**, 128-133.
86. L. Wu, X. H. Hu, J. F. Qian, F. Pei, F. Y. Wu, R. J. Mao, X. P. Ai, H. X. Yang and Y. L. Cao, *Journal of Materials Chemistry A*, 2013, **1**, 7181-7184.
87. L. Wu, P. Pei, R. J. Mao, F. Y. Wu, Y. Wu, J. F. Qian, Y. L. Cao, X. P. Ai and H. X. Yang, *Electrochimica Acta*, 2013, **87**, 41-45.
88. M. Shimizu, H. Usui and H. Sakaguchi, *Journal of Power Sources*, 2014, **248**, 378-382.
89. M. Valvo, F. Lindgren, U. Lafont, F. Bjorefors and K. Edstrom, *Journal of Power Sources*, 2014, **245**, 967-978.
90. C. Didier, M. Guignard, C. Denage, O. Szajwaj, S. Ito, I. Saadoune, J. Darriet and C. Delmas, *Electrochemical and Solid State Letters*, 2011, **14**, A75-A78.
91. E. Ferg, R. J. Gummow, A. Dekock and M. M. Thackeray, *Journal of the Electrochemical Society*, 1994, **141**, L147-L150.
92. T. Ohzuku, A. Ueda and N. Yamamoto, *Journal of the Electrochemical Society*, 1995, **142**, 1431-1435.
93. M. Shirpour, J. Cabana and M. Doeff, *Energy & Environmental Science*, 2013, **6**, 2538-2547.
94. H. Xiong, M. D. Slater, M. Balasubramanian, C. S. Johnson and T. Rajh, *Journal of Physical Chemistry Letters*, 2011, **2**, 2560-2565.
95. A. Rudola, K. Saravanan, S. Devaraj, H. Gong and P. Balaya, *Chemical Communications*, 2013, **49**, 7451-7453.
96. P. Senguttuvan, G. Rousse, V. Seznec, J.-M. Tarascon and M. Rosa Palacin, *Chemistry of Materials*, 2011, **23**.
97. G. Rousse, M. E. Arroyo-de Domablo, P. Senguttuvan, A. Ponrouch, J. M. Tarascon and M. R. Palacin, *Chemistry of Materials*, 2013, **25**, 4946-4956.
98. J. Xu, D. H. Lee and Y. S. Meng, *Functional materials letters*, 2013, **6**, 1330001.
99. C. Lamberti, *Surface Science Reports*, 2004, **53**, 1-197.
100. B. D. Cullity, *Elements of X-ray diffraction, 2nd edition*, 1978, xii+555 pp.
101. A. K. Cheetham and A. P. Wilkinson, *Angewandte Chemie-International Edition in English*, 1992, **31**, 1557-1570.

102. J. McBreen, *Journal of Solid State Electrochemistry*, 2009, **13**, 1051-1061.
103. D. Majuste, V. S. T. Ciminelli, P. J. Eng and K. Osseo-Asare, *Hydrometallurgy*, 2013, **131**, 54-66.
104. F. Tannazi and G. Bunker, *Physica Scripta*, 2005, **T115**, 953-956.
105. Y. S. Meng and M. Elena Arroyo-de Dompablo, *Energy & Environmental Science*, 2009, **2**, 589-609.
106. P. Hohenberg and W. Kohn, *Physical Review B*, 1964, **136**, B864-+.
107. W. Kohn and L. J. Sham, *Physical Review*, 1965, **140**, A1133-A1138.
108. L. J. Sham and W. Kohn, *Physical Review*, 1966, **145**, 561-&.
109. A. I. Liechtenstein, V. I. Anisimov and J. Zaanen, *Physical Review B*, 1995, **52**, R5467-R5470.
110. J. P. Perdew, K. Burke and Y. Wang, *Physical Review B*, 1996, **54**, 16533.
111. F. Zhou, M. Cococcioni, C. A. Marianetti, D. Morgan and G. Ceder, *Physical Review B*, 2004, **70**.
112. L. Wang, T. Maxisch and G. Ceder, *Physical Review B*, 2006, **73**.
113. M. C. Payne, M. P. Teter, D. C. Allan, T. A. Arias and J. D. Joannopoulos, *Reviews of Modern Physics*, 1992, **64**, 1045-1097.
114. M. K. Aydinol and G. Ceder, *Journal of the Electrochemical Society*, 1997, **144**, 3832-3835.
115. M. K. Aydinol, A. F. Kohan, G. Ceder, K. Cho and J. Joannopoulos, *Physical Review B*, 1997, **56**, 1354-1365.
116. A. V. d. Ven and G. Ceder, *physical Review B*, 1999, **59**, 742-749.
117. A. Van der Ven, G. Ceder, M. Asta and P. D. Tepesch, *Physical Review B*, 2001, **64**.
118. A. Van der Ven and G. Ceder, *Electrochemistry Communications*, 2004, **6**, 1045-1050.
119. Y. Hinuma, Y. S. Meng, K. Kang and G. Ceder, *Chemistry of Materials*, 2007, **19**, 1790-1800.
120. G. H. Vineyard, *Journal of Physics and Chemistry of Solids*, 1957, **3**, 121-127.

121. P. Mazur, W. F. Rall and S. P. Leibo, *Cell Biophysics*, 1984, **6**, 197-213.
122. P. Mazur and B. Djafarirouhani, *Physical Review B*, 1984, **30**, 6759-6762.
123. C. W. J. Beenakker and P. Mazur, *Physica A*, 1984, **126**, 349-370.
124. L. Onsager, *Physical Review*, 1931, **37**, 405-426.
125. L. Onsager, *Physical Review*, 1931, **38**, 2265-2279.
126. H. B. Callen and T. A. Welton, *Physical Review*, 1951, **83**, 34-40.
127. H. B. Callen and R. F. Greene, *Physical Review*, 1952, **86**, 702-710.
128. M. S. Green, *Journal of Chemical Physics*, 1952, **20**, 1281-1295.
129. M. S. Green, *Journal of Chemical Physics*, 1954, **22**, 398-413.
130. R. Kubo, *Journal of the Physical Society of Japan*, 1957, **12**, 570-586.
131. R. Kubo, M. Yokota and S. Nakajima, *Journal of the Physical Society of Japan*, 1957, **12**, 1203-1211.
132. R. Zwanzig, *Journal of Chemical Physics*, 1964, **40**, 2527-&.
133. R. Zwanzig, *Annual Review of Physical Chemistry*, 1965, **16**, 67-&.
134. G. Mills, H. Jonsson and G. K. Schenter, *Surface Science*, 1995, **324**, 305-337.
135. Z. G. Yang, J. L. Zhang, M. C. W. Kintner-Meyer, X. C. Lu, D. W. Choi, J. P. Lemmon and J. Liu, *Chemical Reviews*, 2011, **111**, 3577-3613.
136. M. S. Whittingham, *Progress in Solid State Chemistry*, 1978, **12**, 41-99.
137. A. S. Nagelberg and W. L. Worrell, *Journal of Solid State Chemistry*, 1979, **29**, 345-354.
138. C. Delmas, J. J. Braconnier, C. Fouassier and P. Hagenmuller, *Solid State Ionics*, 1981, **3-4**, 165-169.
139. J. Molenda, C. Delmas and P. Hagenmuller, *Solid State Ionics*, 1983, **9-10**, 431-435.
140. J. M. Tarascon and G. W. Hull, *Solid State Ionics*, 1986, **22**, 85-96.
141. F. Tournadre, L. Croguennec, I. Saadoune, D. Carlier, Y. Shao-Horn, P. Willmann and C. Delmas, *Journal of Solid State Chemistry*, 2004, **177**, 2790-2802.

142. M. Pollet, M. Blangero, J. P. Doumerc, R. Decourt, D. Carlier, C. Denage and C. Delmas, *Inorganic Chemistry*, 2009, **48**, 9671-9683.
143. D. Carlier, M. Blangero, M. Menetrier, M. Pollet, J. P. Doumerc and C. Delmas, *Inorganic Chemistry*, 2009, **48**, 7018-7025.
144. R. Berthelot, D. Carlier and C. Delmas, *Nature Materials*, 2011, **10**, 74-U73.
145. Y. L. Cao, L. F. Xiao, W. Wang, D. W. Choi, Z. M. Nie, J. G. Yu, L. V. Saraf, Z. G. Yang and J. Liu, *Advanced Materials*, 2011, **23**, 3155-+.
146. F. Sauvage, L. Laffont, J. M. Tarascon and E. Baudrin, *Inorganic Chemistry*, 2007, **46**, 3289-3294.
147. H. Kim, D. J. Kim, D. H. Seo, M. S. Yeom, K. Kang, D. K. Kim and Y. Jung, *Chemistry of Materials*, 2012, **24**, 1205-1211.
148. S.-W. Kim, D.-H. Seo, X. Ma, G. Ceder and K. Kang, *Advanced Energy Materials*, 2012.
149. H. Kim, D. J. Kim, D.-H. Seo, M. S. Yeom, K. Kang, D. K. Kim and Y. Jung, *Chemistry of Materials*, 2012, **24**, 1205-1211.
150. S. P. Ong, V. L. Chevrier, G. Hautier, A. Jain, C. Moore, S. Kim, X. Ma and G. Ceder, *Energy & Environmental Science*, 2011, **4**, 3680-3688.
151. J. Rodriguez-Carvajal, *Physica B*, 1993, **192**, 55-69.
152. G. Kresse and D. Joubert, *Physical Review B*, 1999, **59**, 1758-1775.
153. G. Kresse and J. Furthmuller, *Computational Materials Science*, 1996, **6**, 15-50.
154. G. Kresse and J. Furthmuller, *Physical Review B*, 1996, **54**, 11169-11186.
155. G. Kresse, J. Furthmuller and J. Hafner, *Physical Review B*, 1994, **50**, 13181-13185.
156. J. P. Perdew, K. Burke and Y. Wang, *Physical Review B*, 1996, **54**, 16533-16539.
157. S. P. Ong, V. L. Chevrier, G. Hautier, A. Jain, C. Moore, S. Kim, X. H. Ma and G. Ceder, *Energy & Environmental Science*, 2011, **4**, 3680-3688.
158. A. V. d. Ven, C. Marianetti, D. Morgan and G. Ceder, *Solid State Ionics*, 2000, **135**, 21-32.
159. A. Caballero, L. Herna'n, J. Morales, L. Sa'nchez, J. S. Pen'a and M. A. G. Aranda, *Journal of Materials Chemistry*, 2002, **12**, 1142-1147.

160. Y. Hinuma, Y. S. Meng and G. Ceder, *Physical Review B*, 2008, **77**, 224111.
161. Y. S. Meng, Y. Hinuma and G. Ceder, *THE JOURNAL OF CHEMICAL PHYSICS*, 2008, **128**, 104708-104708.
162. W. W. Pai, S. H. Huang, Y. S. Meng, Y. C. Chao, C. H. Lin, H. L. Liu and F. C. Chou, *Physical Review Letters*, 2008, **100**, 4.
163. J. Breger, N. Dupre, P. J. Chupas, P. L. Lee, T. Proffen, J. B. Parise and C. P. Grey, *Journal of the American Chemical Society*, 2005, **127**, 7529-7537.
164. J. Breger, M. Jiang, N. Dupre, Y. S. Meng, Y. Shao-Horn, G. Ceder and C. P. Grey, *Journal of Solid state chemistry*, 2005, **178**, 2575–2585.
165. A. Van der Ven and G. Ceder, *Electrochem. Solid State Lett.*, 2000, **3**, 301-304.
166. K. Kang, Y. S. Meng, J. Breger, C. P. Grey and G. Ceder, *Science*, 2006, **311**, 977-980.
167. E. Markevich, M. D. Levi and D. Aurbach, *Journal of Electroanalytical Chemistry*, 2005, **580**, 231-237.
168. S. Yang, X. Wang, X. Yang, Y. Bai, Z. Liu, H. Shu and Q. Wei, *Electrochimica Acta*, 2012, **66**, 88-93.
169. J. Gao and A. Manthiram, *Journal of Power Sources*, 2009, **191**, 644-647.
170. B. Xu, C. R. Fell, M. Chi and Y. S. Meng, *Energy & Environmental Science*, 2011.
171. A. Rudola, K. Saravanan, C. W. Mason and P. Balaya, *J. Mater. Chem. A*, 2013, **1**, 2653-2662.
172. P. Senguttuvan, G. Rousse, V. Seznec, J.-M. Tarascon and M. R. Palacín, *Chemistry of Materials*, 2011, **23**, 4109–4111.
173. Z. Lu and J. R. Dahn, *Journal of the Electrochemical Society*, 2001, **148**, A1225-A1229.
174. D. Kim, S.-H. Kang, M. Slater, S. Rood, J. T. Vaughey, N. Karan, M. Balasubramanian and C. S. Johnson, *Advanced Energy Materials*, 2011, **1**, 333-336.
175. B. H. Toby, *Journal of Applied Crystallography*, 2001, **34**, 210-213.

176. R. J. Clement, A. J. Pell, D. S. Middlemiss, F. C. Strobridge, J. K. Miller, M. S. Whittingham, L. Emsley, C. P. Grey and G. Pintacuda, *Journal of the American Chemical Society*, 2012, **134**, 17178-17185.
177. I. Hung, L. N. Zhou, F. Pourpoint, C. P. Grey and Z. H. Gan, *Journal of the American Chemical Society*, 2012, **134**, 1898-1901.
178. H. Jian Zhi, D. W. Alderman, Y. Chaohui, R. J. Pugmire and D. M. Grant, *Journal of Magnetic Resonance, Series A*, 1993, **105**, 82-87.
179. T. L. Hwang, P. C. M. van Zijl and M. Garwood, *Journal of Magnetic Resonance*, 1998, **133**, 200-203.
180. G. Kervern, G. Pintacuda and L. Emsley, *Chemical Physics Letters*, 2007, **435**, 157-162.
181. D. Massiot, F. Fayon, M. Capron, I. King, S. Le Calve, B. Alonso, J. O. Durand, B. Bujoli, Z. H. Gan and G. Hoatson, *Magnetic Resonance in Chemistry*, 2002, **40**, 70-76.
182. M. Newville, *Journal of Synchrotron Radiation*, 2001, **8**, 322-324.
183. B. Ravel and M. Newville, *Journal of Synchrotron Radiation*, 2005, **12**, 537-541.
184. Z. Lu and J. R. Dahn, *Journal of the Electrochemical Society*, 2001, **148**, A1225-A1229.
185. Z. Lu, R. A. Donaberger and J. R. Dahn, *Chemistry of Materials*, 2000, **12**, 3583-3590.
186. Y. S. Meng, G. Ceder, C. P. Grey, W. S. Yoon, M. Jiang, J. Breger and Y. Shao-Horn, *Chemistry of Materials*, 2005, **17**.
187. J. Kim, D. S. Middlemiss, N. A. Chernova, B. Y. X. Zhu, C. Masquelier and C. P. Grey, *Journal of the American Chemical Society*, 2010, **132**, 16825-16840.
188. C. P. Grey and N. Dupre, *Chemical Reviews*, 2004, **104**, 4493-4512.
189. W. S. Yoon, S. Iannopollo, C. P. Grey, D. Carlier, J. Gorman, J. Reed and G. Ceder, *Electrochemical and Solid State Letters*, 2004, **7**, A167-A171.
190. J. Cabana, N. A. Chernova, J. Xiao, M. Roppolo, K. A. Aldi, M. S. Whittingham and C. P. Grey, *Inorganic Chemistry*, 2013, **52**, 8540-8550.
191. L. Zhonghua and J. R. Dahn, *Chemistry of Materials*, 2001, **13**, 2078-2083.
192. T. Mueller and G. Ceder, *Physical Review B*, 2010, **82**, 7.

193. X. Jiang, C. Århammar, P. Liu, J. Zhao and R. Ahuja, *Scientific Reports*, 2013, **3**.
194. C. P. Grey, W. S. Yoon, J. Reed and G. Ceder, *Electrochemical and Solid State Letters*, 2004, **7**, A290-A293.
195. J. M. Paulsen, R. A. Donaberger and J. R. Dahn, *Chemistry of Materials*, 2000, **12**, 2257-2267.
196. D. H. Lee, J. Xu and Y. S. Meng, *Physical Chemistry Chemical Physics*, 2013, **15**, 3304-3312.
197. M. Guignard, C. Didier, J. Darriet, P. Bordet, E. Elkaim and C. Delmas, *Nature Materials*, 2013, **12**, 74-80.
198. J. M. Tarascon, *Philosophical Transactions of the Royal Society a-Mathematical Physical and Engineering Sciences*, 2010, **368**, 3227-3241.
199. V. Palomares, M. Casas-Cabanas, E. Castillo-Martinez, M. H. Han and T. Rojo, *Energy & Environmental Science*, 2013, **6**, 2312-2337.
200. J. Xu, D. H. Lee and Y. S. Meng, *Functional Materials Letters*, 2013, **6**.
201. H. Yoshida, N. Yabuuchi, K. Kubota, I. Ikeuchi, A. Garsuch, M. Schulz-Dobrick and S. Komaba, *Chemical Communications*, 2014, **50**, 3677-3680.
202. Z. Jie, X. Jing, L. Dae Hoe, N. Dimov, Y. S. Meng and S. Okada, *Journal of Power Sources*, 2014, **264**, 235-239.
203. S. W. Kim, D. H. Seo, X. H. Ma, G. Ceder and K. Kang, *Advanced Energy Materials*, 2012, **2**, 710-721.
204. C. R. Fell, K. J. Carroll, M. Chi and Y. S. Meng, *Journal of The Electrochemical Society*, 2010, **157**, A1202.
205. H. Liu, C. R. Fell, K. An, L. Cai and Y. S. Meng, *Journal of Power Sources*, 2013, **240**, 772-778.
206. B. Xu, C. R. Fell, M. Chi and Y. S. Meng, *Energy & Environmental Science*, 2011, **4**.
207. B. H. Qu, C. Z. Ma, G. Ji, C. H. Xu, J. Xu, Y. S. Meng, T. H. Wang and J. Y. Lee, *Advanced Materials*, 2014, **26**, 3854-3859.
208. N. Yabuuchi, M. Kajiyama, J. Iwatate, H. Nishikawa, S. Hitomi, R. Okuyama, R. Usui, Y. Yamada and S. Komaba, *Nature Materials*, 2012, **11**, 512-517.

209. N. Yabuuchi, M. Yano, H. Yoshida, S. Kuze and S. Komaba, *Journal of the Electrochemical Society*, 2013, **160**, A3131-A3137.
210. D. Kim, E. Lee, M. Slater, W. Q. Lu, S. Rood and C. S. Johnson, *Electrochemistry Communications*, 2012, **18**, 66-69.
211. X. F. Wang, M. Tamaru, M. Okubo and A. Yamada, *Journal of Physical Chemistry C*, 2013, **117**, 15545-15551.
212. P. Barpanda, G. Liu, C. D. Ling, M. Tamaru, M. Avdeev, S.-C. Chung, Y. Yamada and A. Yamada, *Chemistry of Materials*, 2013, **25**, 3480-3487.
213. P. Barpanda, J. Lu, T. Ye, M. Kajiyama, S.-C. Chung, N. Yabuuchi, S. Komaba and A. Yamada, *Rsc Advances*, 2013, **3**, 3857-3860.
214. K. H. Ha, S. H. Woo, D. Mok, N. S. Choi, Y. Park, S. M. Oh, Y. Kim, J. Kim, J. Lee, L. F. Nazar and K. T. Lee, *Advanced Energy Materials*, 2013, **3**, 770-776.
215. J. Y. Jang, H. Kim, Y. Lee, K. T. Lee, K. Kang and N.-S. Choi, *Electrochemistry Communications*, 2014, **44**, 74-77.
216. H. Kim, Y.-U. Park, K.-Y. Park, H.-D. Lim, J. Hong and K. Kang, *Nano Energy*, 2014, **4**, 97-104.
217. Y. U. Park, D. H. Seo, H. S. Kwon, B. Kim, J. Kim, H. Kim, I. Kim, H. I. Yoo and K. Kang, *Journal of the American Chemical Society*, 2013, **135**, 13870-13878.
218. H. Kim, I. Park, S. Lee, H. Kim, K.-Y. Park, Y.-U. Park, H. Kim, J. Kim, H.-D. Lim, W.-S. Yoon and K. Kang, *Chemistry of Materials*, 2013, **25**, 3614-3622.
219. H. Kim, I. Park, D. H. Seo, S. Lee, S. W. Kim, W. J. Kwon, Y. U. Park, C. S. Kim, S. Jeon and K. Kang, *Journal of the American Chemical Society*, 2012, **134**, 10369-10372.
220. K. Saravanan, C. W. Mason, A. Rudola, K. H. Wong and P. Balaya, *Advanced Energy Materials*, 2013, **3**, 444-450.
221. S. Lee, Y. Cho, H. K. Song, K. T. Lee and J. Cho, *Angewandte Chemie-International Edition*, 2012, **51**, 8748-8752.
222. J. Xu, D. H. Lee, R. J. Clement, X. Q. Yu, M. Leskes, A. J. Pell, G. Pintacuda, X. Q. Yang, C. P. Grey and Y. S. Meng, *Chemistry of Materials*, 2014, **26**, 1260-1269.
223. W. Ra, M. Nakayama, W. Cho, M. Wakihara and Y. Uchimoto, *Physical Chemistry Chemical Physics*, 2006, **8**, 882-889.

224. Y. Shiro, F. Sato, T. Suzuki, T. Iizuka, T. Matsushita and H. Oyanagi, *Journal of the American Chemical Society*, 1990, **112**, 2921-2924.
225. M. Venkateswarlu, C. H. Chen, J. S. Do, C. W. Lin, T. C. Chou and B. J. Hwang, *Journal of Power Sources*, 2005, **146**, 204-208.
226. W. Ra, M. Nakayama, H. Ikuta, Y. Uchimoto and M. Wakihara, *Applied Physics Letters*, 2004, **84**, 4364-4366.
227. S.-W. Kim, D.-H. Seo, X. Ma, G. Ceder and K. Kang, *Advanced Energy Materials*, 2012, **2**, 710-721.
228. A. Ponrouch, E. Marchante, M. Courty, J. M. Tarascon and M. R. Palacin, *Energy & Environmental Science*, 2012, **5**, 8572-8583.